AD-A151 871

DEVELOPMENT AND VALIDATION OF A NEW FALLOUT

TRANSPORT METHOD USING VARIABLE SPECTRA!. WINDS

DISSERTATION

Arthur T. Hopkins
Major USAF

AFIT/DS/ENP/84-2

DTIC
ELECTE
APR 0 1 1985
S   E
D

DEPARTMENT OF THE AIR FORCE
AIR UNIVERSITY
AIR FORCE INSTITUTE OF TECHNOLOGY

Wright-Patterson Air Force Base, Ohio

85   03   13   120

AFIT/DS/ENP/84-2

DEVELOPMENT AND VALIDATION OF A NEW FALLOUT

TRANSPORT METHOD USING VARIABLE SPECTRAL WINDS

DISSERTATION

Arthur T. Hopkins
Major USAF

AFIT/DS/ENP/84-2

DTIC
ELECTE
S
APR 0 1 1985
E
D

Approved for public release; distribution unlimited

DEVELOPMENT AND VALIDATION OF A NEW FALLOUT

TRANSPORT METHOD USING VARIABLE SPECTRAL WINDS

DISSERTATION

Presented to the Faculty of the School of Engineering

of the Air Force Institute of Technology

Air University

In Partial Fulfillment of the

Requirements for the Degree of

Doctor of Philosophy

Arthur T. Hopkins, B.S., M.S.

Major, USAF

September 1984

Approved for public release; distribution unlimited

DEVELOPMENT AND VALIDATION OF A NEW FALLOUT

TRANSPORT METHOD USING VARIABLE SPECTRAL WINDS

Arthur T. Hopkins, B.S., M.S.

Major, USAF

Approved:

Charles J. Bridgman, Chairman   Sept 11 '84

David L. Auton   10 Sept. 84

George John   Sept 11, 84

John F. Prince   11 Sept. 1984

Dennis W. Quinn   11 SEPT 1984

Accepted:

J.S. Przemieniecki·
Dean, School of Engineering

Preface

The purpose of this research was to develop and validate a fallout prediction method using variable winds for particle transport calculations. The new method uses National Meteorological Center (NMC) spectral coefficients to compute wind vectors along the space and time varying trajectories of falling particles. The method was validated by comparing computed and actual cloud trajectories from a Mount St. Helens volcanic eruption and a high explosive dust cloud. ----> $p. \, Xi$

The NMC supported this study by providing spectral coefficients for model development, sample wind vector data for model checkout and verification statistics for the accuracy assessment. I am grateful to LtCol John D. Warburton for his kind assistance and advice. In addition, I thank Maj James Kester and Lt Joyce White, ASD Staff Meteorologists, for obtaining the archived weather data used in the Mount St. Helens analysis.

I particularly thank Dr. Charles J. Bridgman, my advisor and research committee chairman, for his objective and constructive counsel throughout this dissertation study. I also thank the members of my research committee, Dr. George John, Dr. Dennis Quinn and Dr. David Auton, for their guidance and support.

This research was sponsored by the Defense Nuclear Agency (DNA). I gratefully acknowledge the support of DNA's technical library staff and the DIRECT COURSE project staff.

Not least, I thank Jeannie (my wife and word processor), Sarah and Patrick.

<div align="right">Arthur T. Hopkins</div>

Table of Contents

List of Figures

List of Tables

Abstract

A new method has been developed to incorporate variable winds into fallout transport calculations. The method uses spectral coefficients derived by the National Meteorological Center. Wind vector components are computed with the coefficients along the trajectories of falling particles. Spectral winds are used in the two-step method to compute dose rate on the ground, downwind of a nuclear cloud. First, the hotline is located by computing trajectories of particles from an initial, stabilized cloud, through spectral winds, to the ground. The connection of particle landing points is the hotline. Second, dose rate on and around the hotline is computed by analytically smearing the falling cloud's activity along the ground. The feasibility of using spectral winds for fallout particle transport was validated by computing Mount St. Helens ashfall locations and comparing calculations to fallout data. In addition, an ashfall equation was derived for computing volcanic ash mass/area on the ground. Ashfall data and the ashfall equation were used to back-calculate an aggregated particle size distribution for the Mount St. Helens eruption cloud. Further validation was performed by comparing computed and actual trajectories of a high explosive dust cloud (DIRECT COURSE). Using an error propagation formula, it was determined that uncertainties in spectral wind components produce less than four percent of the total dose rate variance. In summary, this research demonstrated the feasibility of using spectral coefficients for fallout transport calculations, developed a two-step smearing model to treat variable winds, and showed that uncertainties in spectral winds do not contribute significantly to the error in computed dose rate.

DEVELOPMENT AND VALIDATION OF A NEW FALLOUT
TRANSPORT METHOD USING VARIABLE SPECTRAL WINDS

I. Introduction

Background

An atmospheric nuclear burst creates a cloud of vaporized radio-
active particles composed of fission fragments, decay products, unfis-
sioned bomb fuel and neutron-induced debris. The radioactive particles
rise with the buoyant nuclear cloud, condensing on microscopic nuclei
or on the surfaces of other particles. As condensed particles grow and
the cloud cools, gravitational forces eventually exceed the forces in-
duced by updraft, and the radioactive particles fall from the cloud.
During their fall, particles are transported by ambient winds. As a
result, radioactive fallout can land far from the point of weapon deto-
nation. Fallout's widespread distribution coupled with its long-term
nature make fallout transport modeling an important part of nuclear
weapon effects studies.

Fallout transport studies have both military and civilian applica-
tions. Militarily, fallout may be an important consideration in studies
of force recovery and organization after a strategic nuclear attack or
during a protracted, limited nuclear war (69)(82). Fallout models are
also used to estimate population exposure from past atmospheric nuclear
weapons tests (8). In civilian applications, fallout models are applied
to study population survival and economic recovery prospects following a
nuclear attack (30)(42)(56)(60)(66)(76). Currently, fallout transport

1

models are even used to estimate potential climatological effects of global nuclear fallout and dust, the "nuclear winter" (105).

Fallout Models

Fallout studies use both numerical and analytic methods to predict particle motion in the atmosphere and dose rates on the ground. The standard numerical fallout code for military applications is DELFIC, the Defense Land Fallout Interpretative Code (79). DELFIC computes cloud rise, growth, stabilization and transport, with detailed simulation of radioactive particle formation. Particle fall is computed in a wind field that is (optionally) spatially constant, spatially constant with temporal updates or spatially interpolated within a finite grid of wind profiles. DELFIC is frequently used as a computational benchmark for simpler analytic models, such as the AFIT (Air Force Institute of Technology) and WSEG (Weapon Systems Evaluation Group) codes (17)(19)(78) (85)(86).

AFIT and WSEG simulate the fallout process by smearing (depositing) the falling cloud's radioactivity on the ground unidirectionally downwind. The analytic codes assume a constant wind vector to transport the cloud (49)(65). The constant wind assumption is a significant source of error, particularly when winds are not nearly constant in time and space.

Particle Transport in Spectral Winds

This report presents a new way to compute particle transport using variable winds. The new method uses spectral coefficients currently generated by the National Meteorological Center (NMC) and soon to be generated by the Air Force Global Weather Central (AFGWC)(103). Spectral coefficients are derived from global wind data collected twice daily,

nearly simultaneously. By fitting the wind data with a truncated series of spherical harmonics, NMC reduces the data to a set of complex spectral coefficients. The coefficients are used in the spherical harmonics expansions to compute wind speeds (spectral winds) anywhere in the atmosphere.

With spectral winds, fallout transport is modeled by computing wind speeds from coefficients at discrete positions and times along the trajectories of falling particles. Horizontal spatial variability is naturally simulated by the harmonic polynomials. There are coefficient sets for each of twelve different altitudes, so winds (or coefficients) must be vertically interpolated to obtain wind speeds between spectral heights. Each coefficient set fits the polynomials to global wind data at a fixed time, so winds (or coefficients) can be temporally interpolated to estimate wind speeds at times when data was not collected.

Using spectral winds to compute fallout particle trajectories will vastly improve the accuracy of fallout prediction codes. Spectral winds represent real atmospheric wind data over the entire globe. Particle trajectories can be computed with continuous, four dimensional variability.

Analytic Fallout Code with Variable Winds

Spectral winds can be used in any numerical or analytic fallout code. The spectral wind equations are ideally suited for calculations of wind-driven particle motion in a Lagrangian reference frame. A numerical fallout code with spectral wind transport would be an ideal fallout prediction sys.em, coupling a state-of-the-art physics model with global, variable winds. However, DELFIC, the standard numerical fallout code is so large and slow that it is impractical to use for most fallout studies,

3

especially when many hypothetical bursts are being considered. Analytic codes, such as AFIT and WSEG, are used for most fallout studies because they are economical, fast-running and benchmarked against DELFIC and actual fallout data (19)(69)(81)(84). In this study, spectral wind transport is incorporated into an analytic fallout code.

The AFIT and WSEG analytic fallout codes were designed for simplified cloud transport with a single wind vector. A new analytic method was developed to compute fallout dose rates with variable winds (53). The new method is a two step approach. First, the radioactive hotline is located by tracking the motion of particles from an initial, stabilized cloud, through spectral winds, to the ground. The hotline is the locus of peak activity downwind of the burst. Second, dose rate is calculated with a solution to the two-directional dose rate integral equation:

$$\dot{D} = k \ Y \ ff \int_0^\infty f(x,y,t) \ g(t) \ dt \qquad (1.1)$$

where

$\dot{D}$ = dose rate at (x,y) at one hour after burst
    note: $\dot{D}$ is called dose rate in this report to be consistent with most fallout references. Actually, $\dot{D}$ is the dose rate to air, or exposure rate, as defined by the International Commission on Radiation Units.
k = source normalization constant, typically 2350 (Roentgens/hour) (square miles/kiloton)
Y = weapon yield (kilotons)
ff = fission fraction
f(x,y,t) = spatial distribution function
g(t) = activity arrival rate function

With the two step method, cloud radioactivity is analytically smeared along the ground on and around a curved hotline defined by explicit particle fall calculations through variable, spectral winds.

Organization of Report

Chapter II explains how the NMC derives spectral coefficients, and how wind vector components are computed from the coefficients. Chapter III describes the hotline locator model that uses spectral winds to transport falling particles from the initial cloud to the ground. A variable wind fallout code is presented in Chapter IV, with an algorithm to compute dose rate at arbitrary field points. Chapter V shows results of two validation studies, using data from a Mount St. Helens ash cloud and from a cloud produced by a large high explosive (not nuclear) atmospheric burst. An error analysis is presented in Chapter VI, quantifying the effects of uncertainties in wind speed (and other independent variables) on dose rate at a point.

Appendix A shows a sample of spectral coefficients for the 1000 millibar height at 00UT (Universal Time) 16 Jan 82. Appendix B contains the derivation of the equation for computing spectral winds. Appendix C illustrates how different nuclear models position the stabilized cloud in the atmosphere. Polynomials for computing the Laurent series coefficients (used to determine particle sizes arriving downwind) are in Appendix D. Appendix E contains an integration of cloud activity in the crosswind direction. The algorithm for off-axis dose rate determination is in Appendix F. Appendix G explains how particle size distributions are fitted with trimodal log-normal distributions, using a constrained minimization search in the nine parameter hyperspace defined by the sum of three log-normal distribution functions.

II. Spectral Wind Calculations

In this report, spectral winds are the wind vector components obtained from NMC spectral coefficients. This chapter describes the source of the coefficients and the equations for computing wind vectors.

NMC Spectral Coefficients

Numerical models of atmospheric motion were developed by the NMC and others to study the general circulation of the atmosphere and to generate forecasts. Atmospheric motion is modeled by NMC with a set of non-linear partial differential equations that describe the temporal variation of space-dependent atmospheric variables (37)(71). The partial differential equations are converted to ordinary differential equations, then solved by finite difference techniques (15)(32)(34)(83). Space-dependent atmospheric variables in the partial differential equations are replaced by spherical harmonic expansions of the form (89)(93) (95):

$$D = \sum_{\ell=-J}^{J} \sum_{n=|\ell|}^{|\ell|+J} D_n^{\ell} \; P_n^{\ell}(\sin\phi) \; EXP(i\ell\lambda) \qquad (2.1)$$

where

D = space (and time) dependent atmospheric variable

D_n^{ℓ} = complex expansion (spectral) coefficient

P_n^{ℓ} = associated Legendre polynomial

ϕ = latitude
λ = longitude
ℓ = zonal (latitudinal) index
n = ordinal (longitudinal) index
J = truncation limit

6

Substituting a series like Eq (2.1) for each space-dependent variable transforms the partial differential equations into a set of ordinary differential equations, with time as the independent variable. The truncation limit, J, is selected by NMC to be high enough for accurate forecasts that are independent of the truncation limit (87).

As defined in the summations, allowable values of ℓ and n are bounded within a rhomboid on a plot of ℓ vs n. Rhomboidal truncation is used primarily because it gives the same number of meridional components for each zonal index (wave number) (35)(94).

Time integration of the differential equations requires initial values of the expansion coefficients, D_n^ℓ. The initial coefficients are computed by NMC using observed global atmospheric data and the normalization integral for spherical harmonics (95). The initial spectral coefficients fit the truncated spherical harmonics to observed global wind data that is collected twice daily. Coefficients can be used to compute the observed wind data and to interpolate the data on a spherical earth.

A set of spectral coefficients is derived for each wind component, u and v, at each of twelve heights in the atmosphere at a fixed time. Figure II-1 shows the spectral heights. Individual sets of coefficients are not empirically or analytically related in the NMC spectral models of atmospheric motion. However, the data used to derive the coefficients comes from continuous vertical soundings, so spectral winds will have an inherent inter-altitude correlation at a fixed time. The NMC has demonstrated that the spectral wind structure is vertically consistent (70). Therefore, particle trajectories, passing through spectral winds at

7
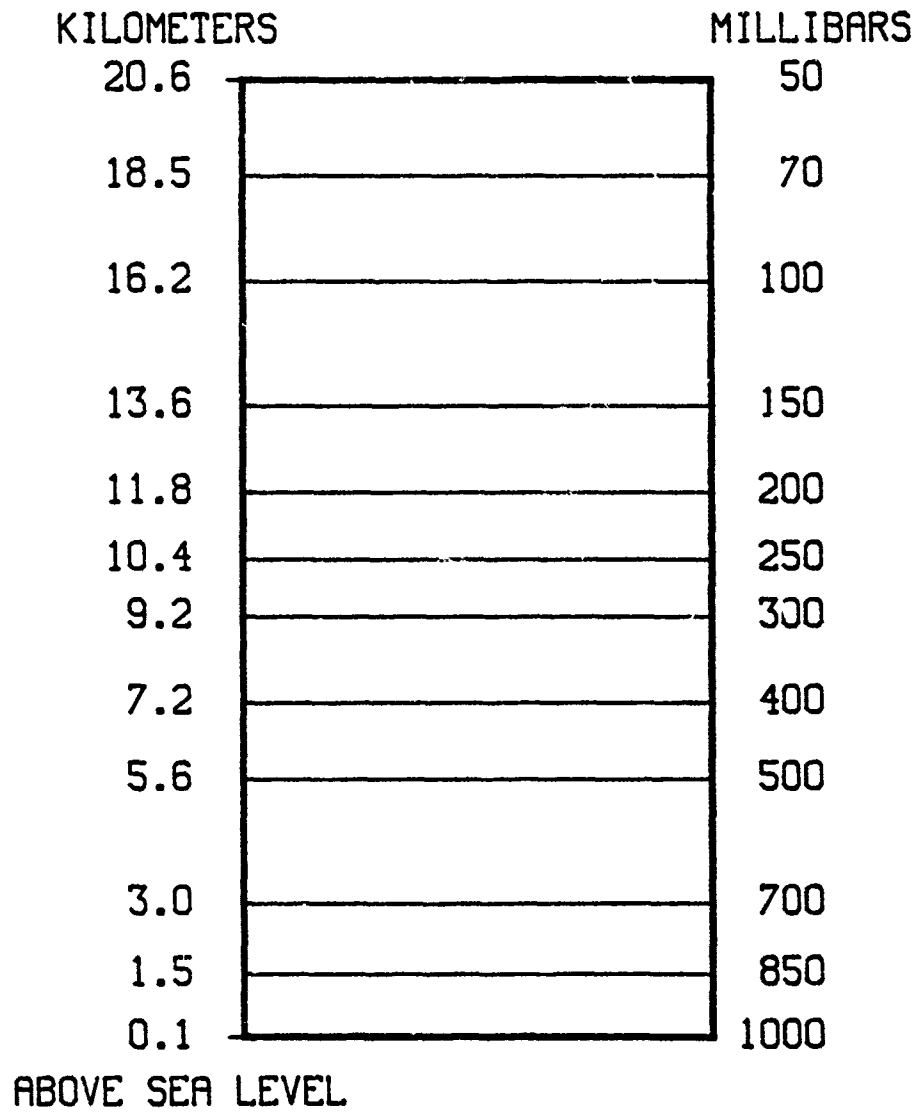
Figure II-1.   Spectral Heights and Pressure Levels

8

various altitudes, should be smooth and continuous.

Appendix A shows some spectral coefficients for the 1000 millibar height at 00UT (Universal Time) on 16 Jan 82. They are for the u-component of wind; 63 complex pairs are shown. A complete set of coefficients for all twelve atmospheric heights, at one time, consists of 23808 complex pairs. Spectral coefficients are routinely archived by NMC at the National Climatic Center, Asheville, North Carolina.

Wind Calculation

With the spectral coefficients for a specific date, time and pressure level, wind vector components can be computed anywhere in the atmosphere using the spherical harmonics expansion (95)(112):

$$(U,V) = (u,v)\cos\phi = \sum_{\ell=-J}^{J} \sum_{n=|\ell|}^{|\ell|+J+1} (U_n^\ell, V_n^\ell) \; P_n^\ell(\sin\phi) \; EXP(i\ell\lambda) \qquad (2.2)$$

where

(U,V) = pseudo-wind components, either U or V
(u,v) = spectral wind components, either u or v
    u = west to east
    v = south to north
(U_n^ℓ, V_n^ℓ) = spectral coefficients, either U_n^ℓ or V_n^ℓ

By rearranging the summation and using identities for spherical harmonics, the spectral equations become:

$$(U,V) = (u,v) \cos\phi$$

$$= Re \sum_{\ell=0}^{J} A \sum_{n=\ell}^{\ell+J+1} (U_n^\ell, V_n^\ell) \; P_n^\ell(\sin\phi) \; (\cos\ell\lambda + i \, \sin\ell\lambda) \qquad (2.3)$$

where

$$A = 1 \quad \text{if} \quad \ell = 0$$
$$A = 2 \quad \text{otherwise}$$

See Appendix B for the stepwise derivation of Eq (2.3) from Eq (2.2). Appendix B also shows the recursion relation for the associated Legendre polynomials, and the computational algorithm for spectral winds.

Figures II-2 through II-13 show fields of wind vectors computed with spectral coefficients at each of the twelve levels. Vectors were computed with Eq (2.3) on $2\frac{1}{2}$ degree intervals in latitude and longitude. High winds associated with the jet stream are easily seen in Figures II-7, 8 and 9 near tropopause heights. The coefficients can be used to compute winds at any global location where fallout or cloud transport predictions are needed.

Truncation

Current NMC models use $J = 30$, so there are 31 zonal indices (ℓ) and 32 ordinal indices (n) for each ℓ. Alternate truncations were examined in this study to determine how abbreviation of (ℓ,n) space affected wind speed calculations (4). Figure II-14 shows alternate rhomboidal truncations of $J = 27, 24, 21, 18$ and 15. Wind vectors were computed at 189 northern hemisphere points at the 1000 millibar level with each truncation, noting the average deviation of each component's magnitude from the corresponding $J = 30$ component's magnitude. This is shown in Figures II-15 and II-16. Deviations were largest when $J < 24$, and v component deviations were generally larger than u component deviations. Most significantly, winds less than 1 meter per second (mps) were much more affected by truncation than winds greater than 1 mps. A truncation to $J = 24$ produces

10
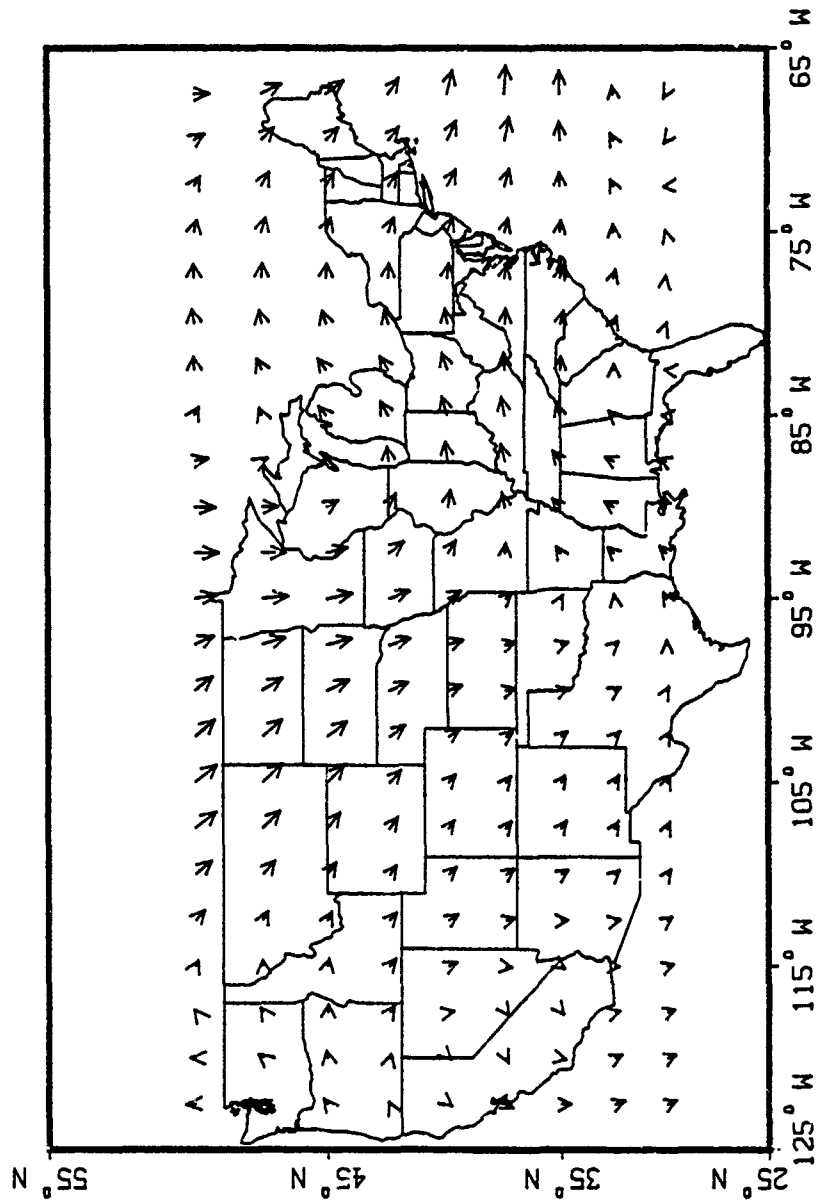
Figure II-2. Spectral Wind Vector Field, 1000 mb

11
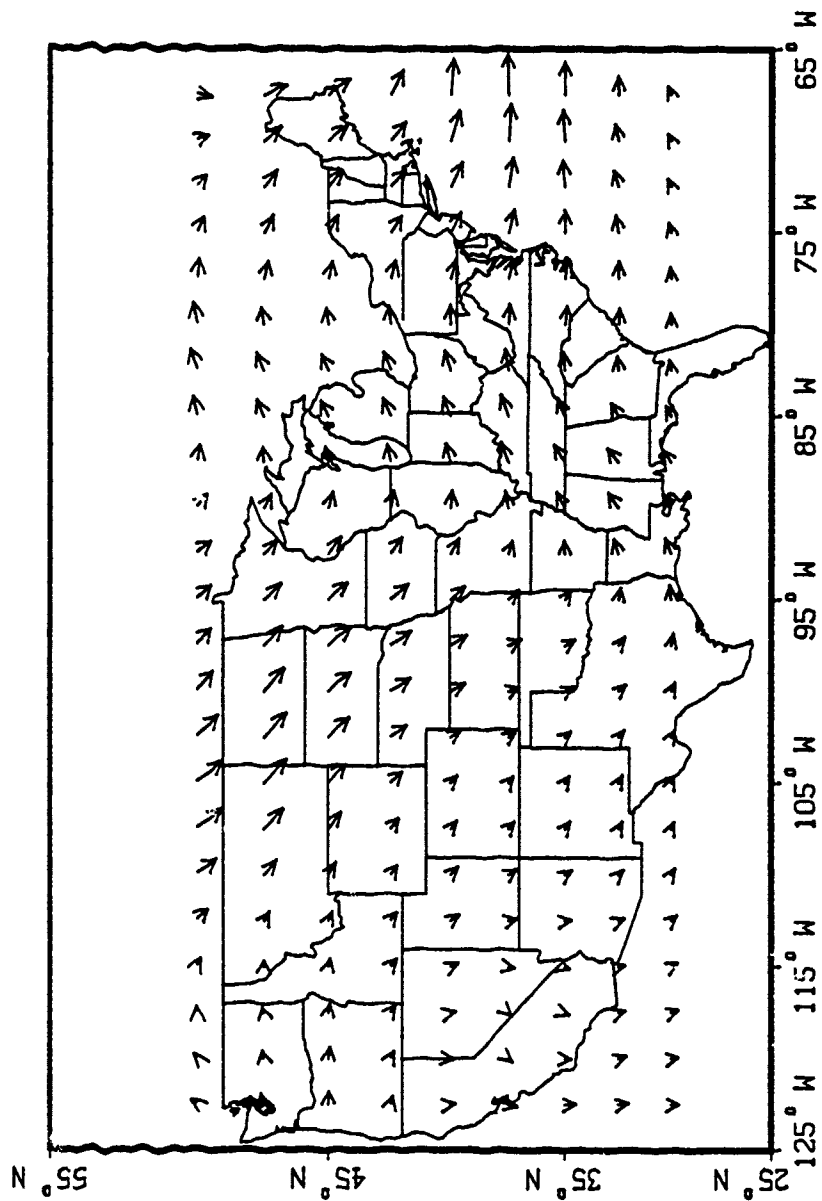
Figure II-3. Spectral Wind Vector Field, 850 mb

12
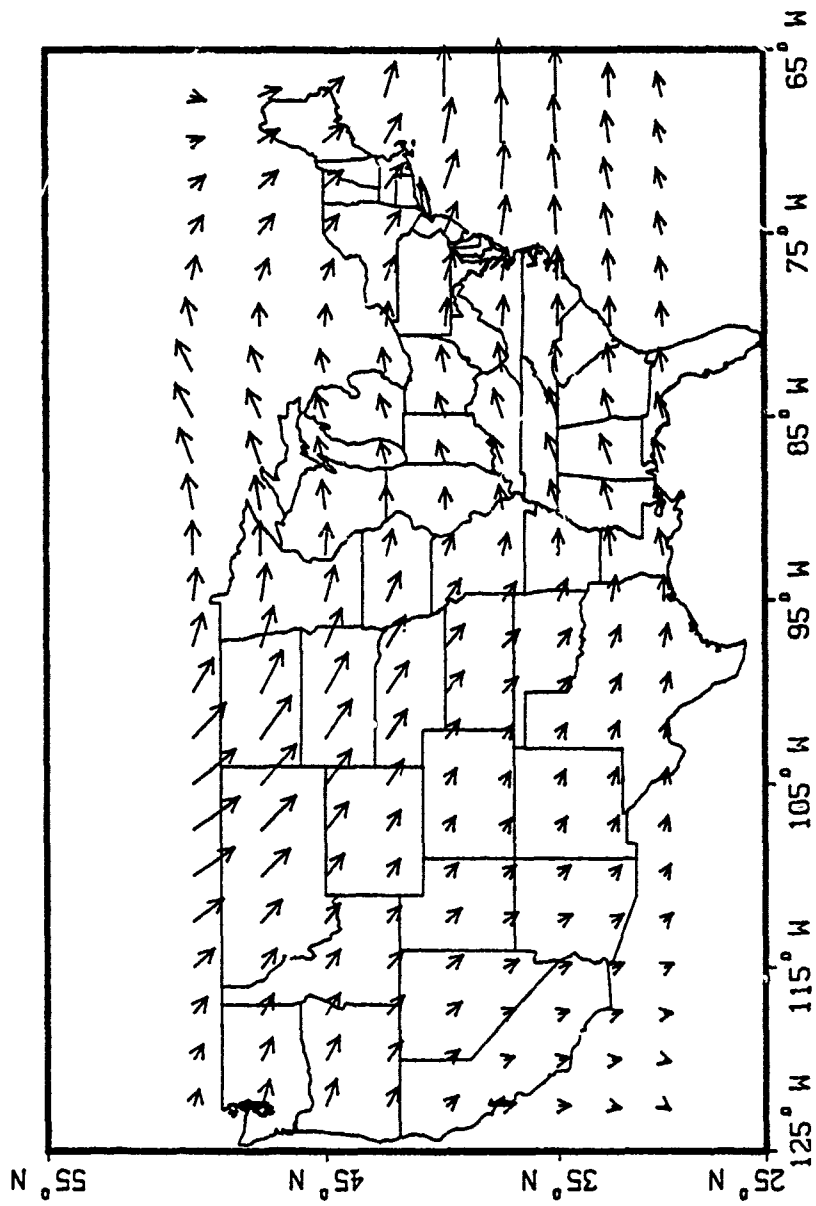
Figure II-4. Spectral Wind Vector Field, 700 mb

13
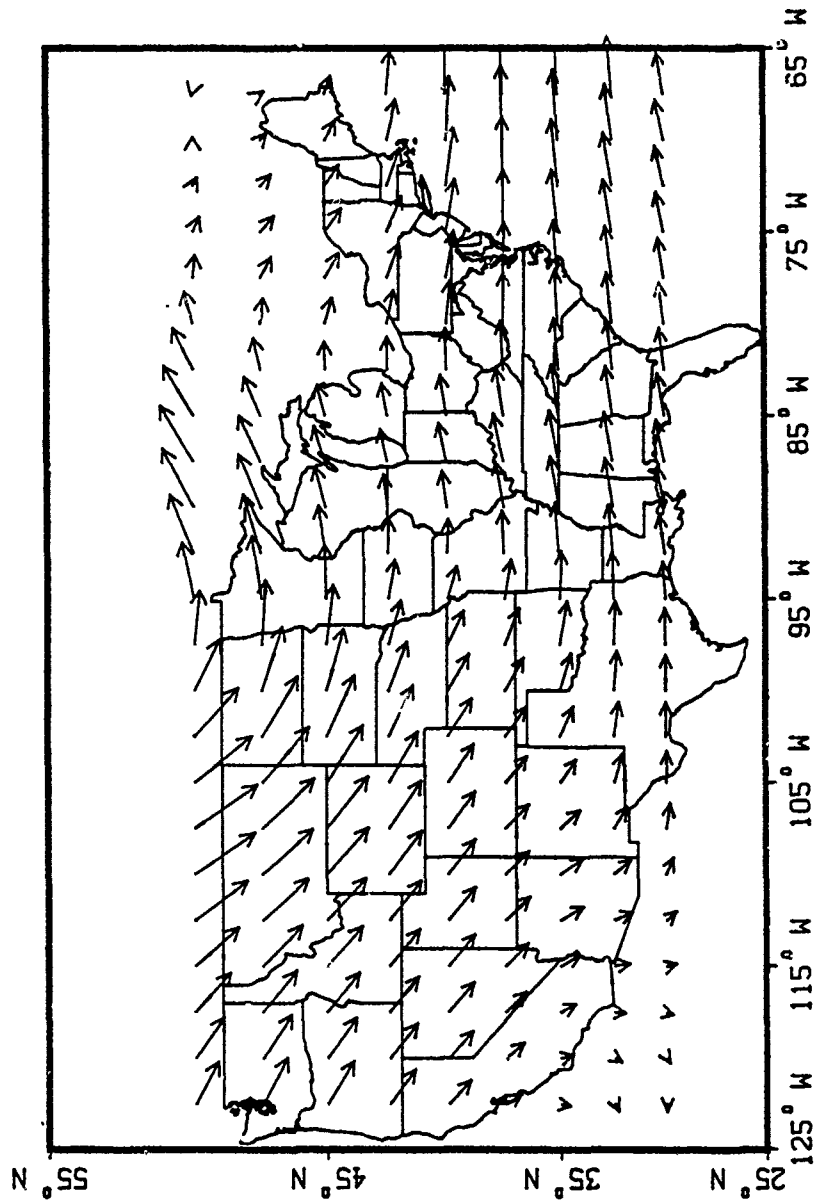
Figure II-5. Spectral Wind Vector Field, 500 mb

14
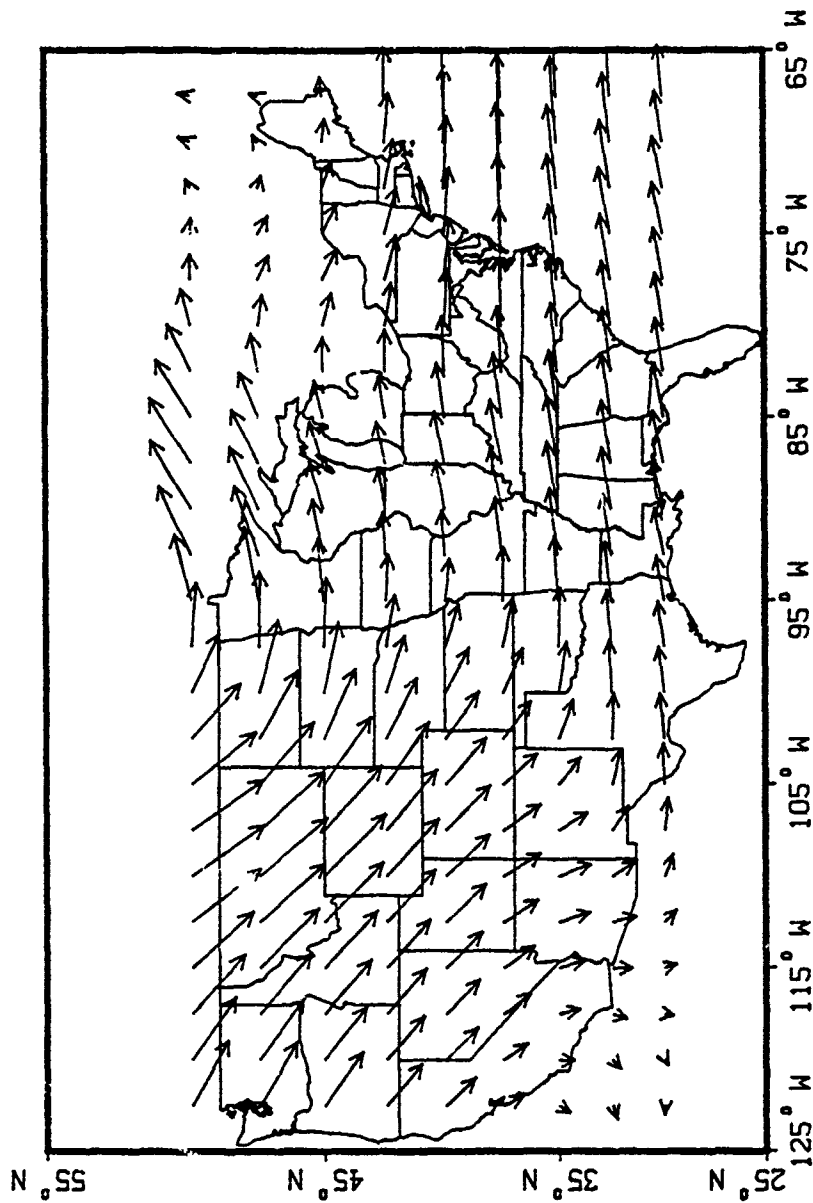
Figure II-6. Spectral Wind Vector Field, 400 mb

15
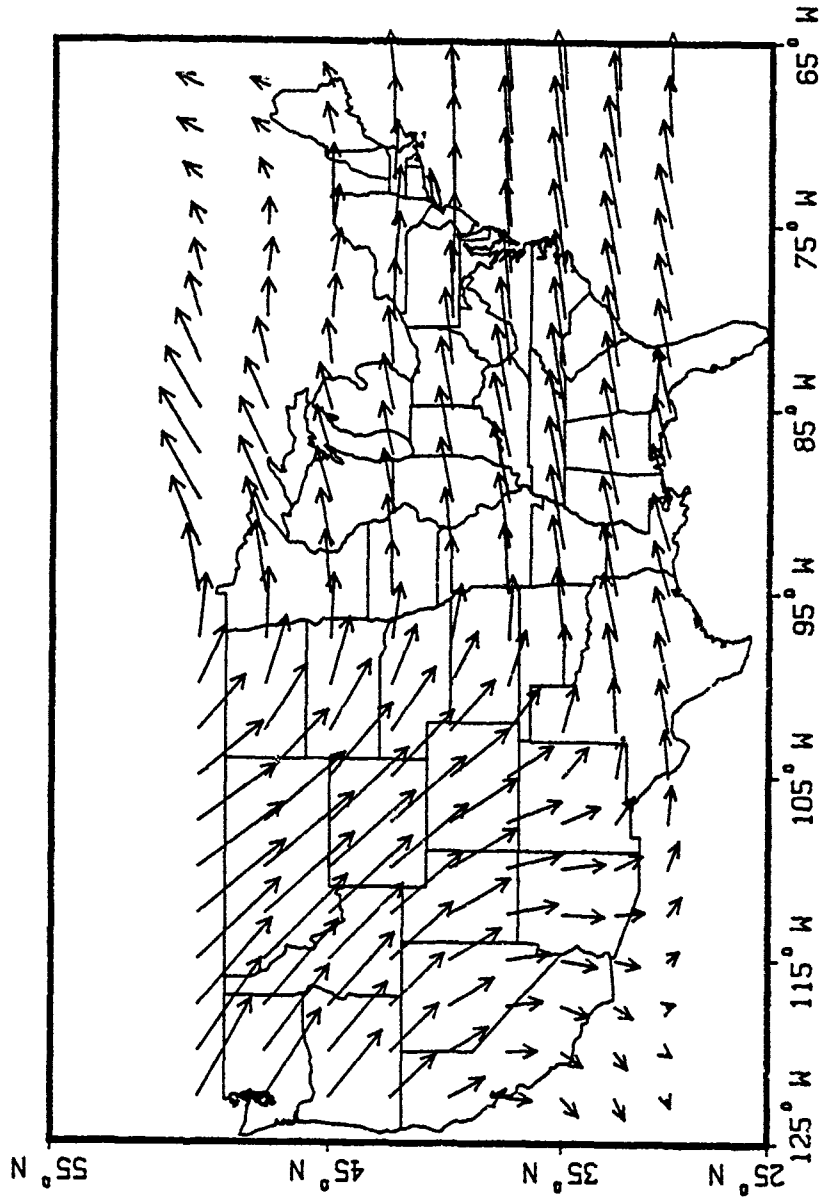
Figure II-7. Spectral Wind Vector Field, 300 mb

16
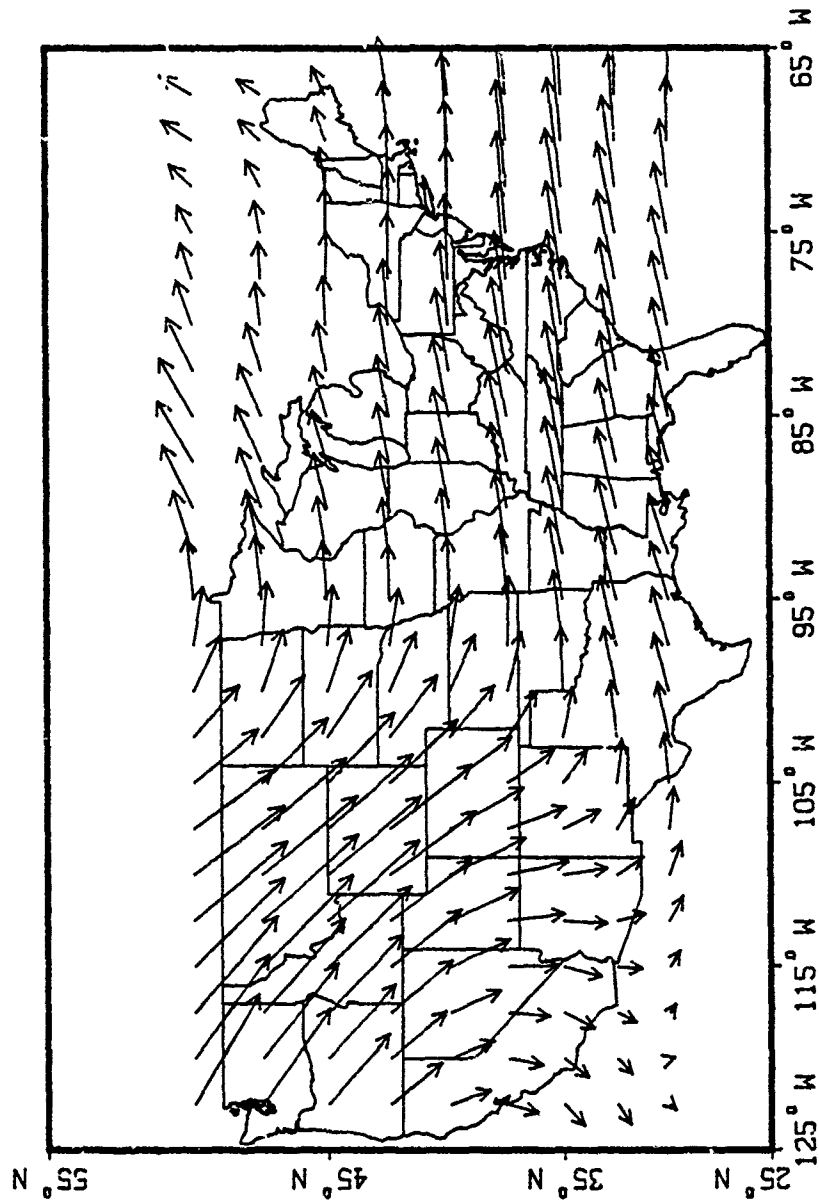
Figure II-8. Spectral Wind Vector Field, 250 mb

17
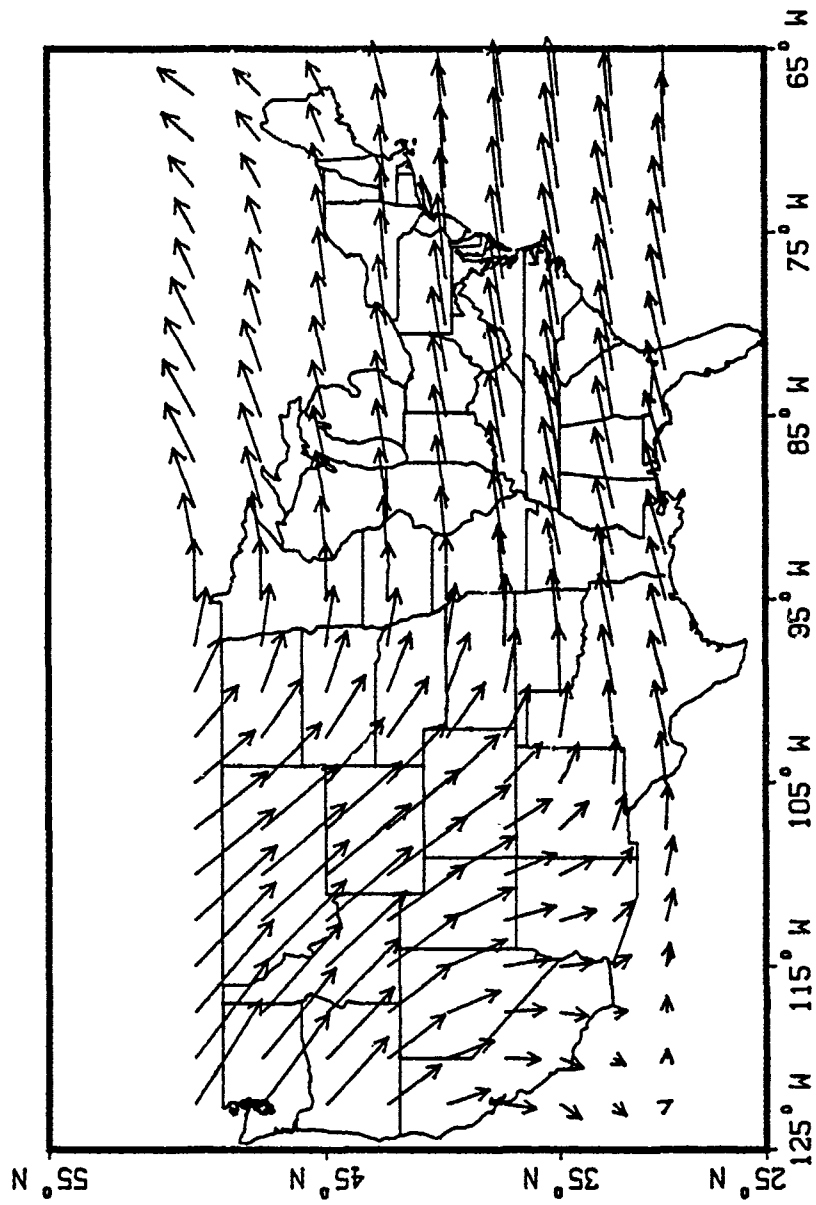
Figure II-9. Spectral Wind Vector Field, 200 mb

18
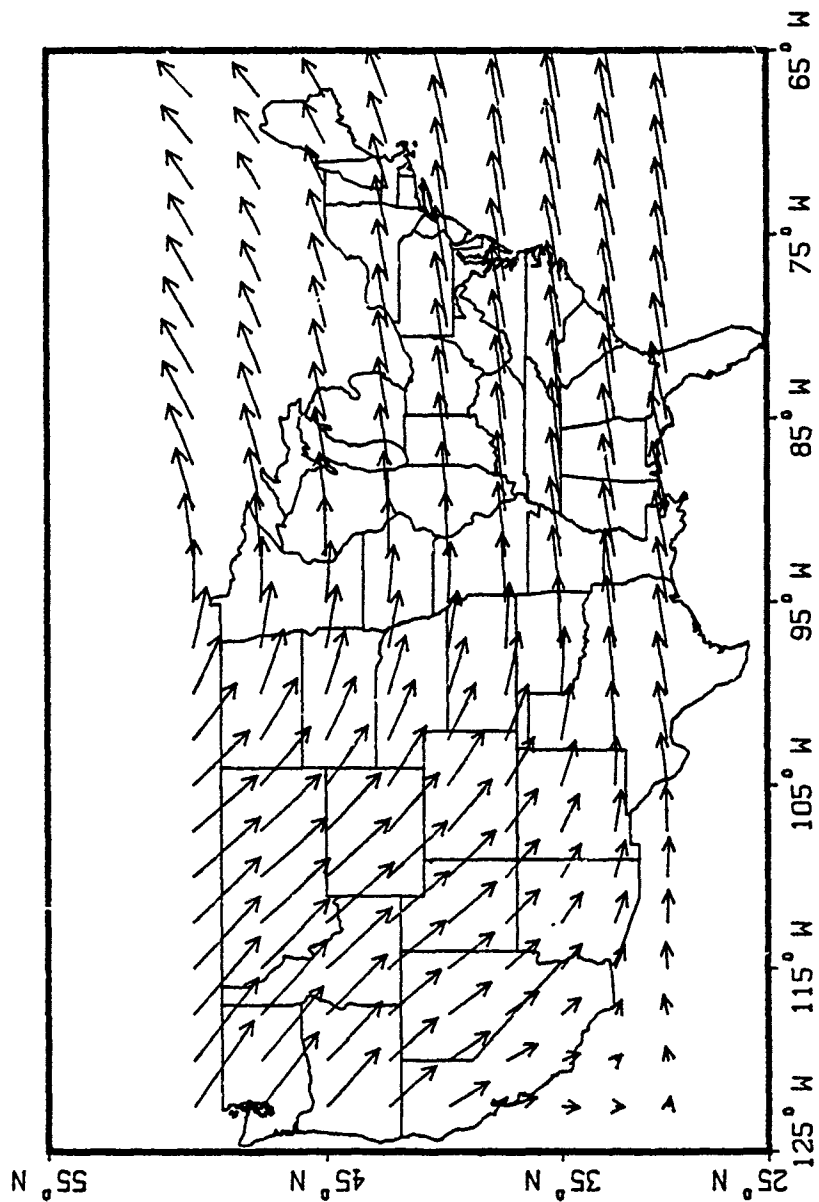
Figure II-10. Spectral Wind Vector Field, 150 mb

19
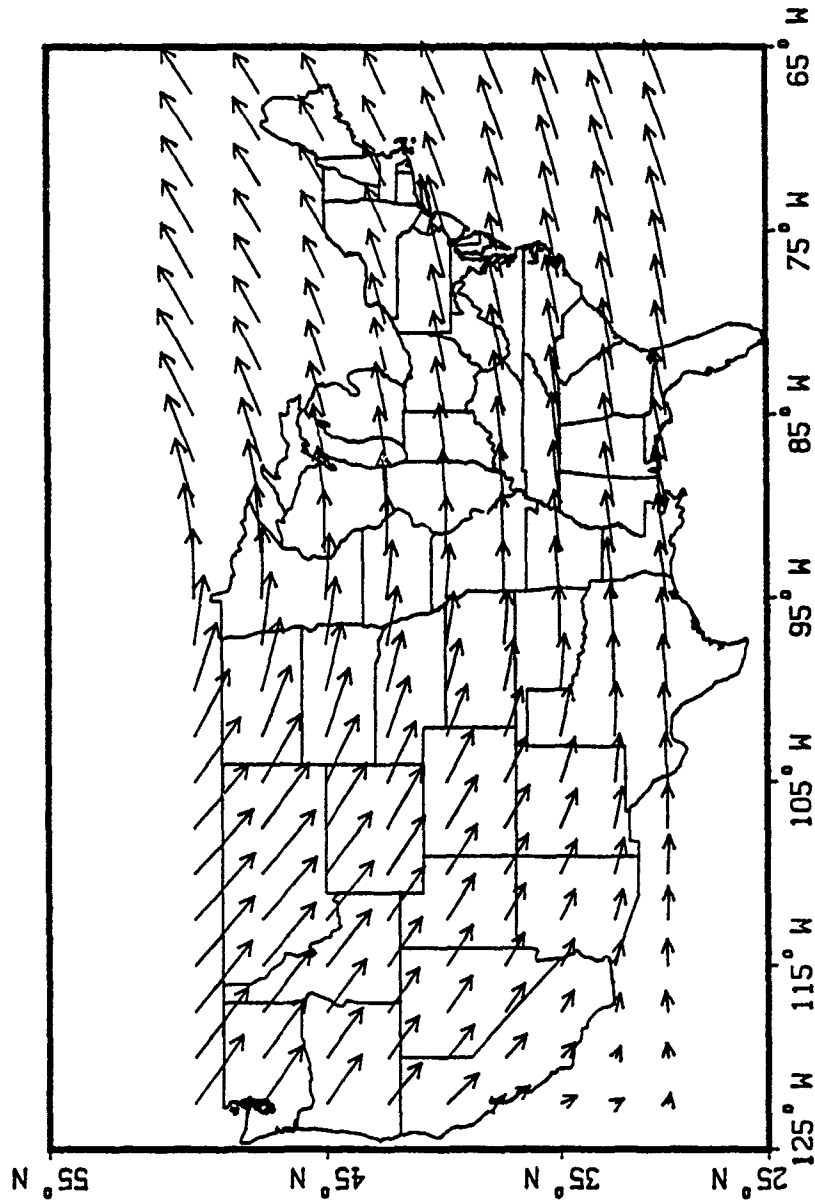
Figure II-11. Spectral Wind Vector Field, 100 mb
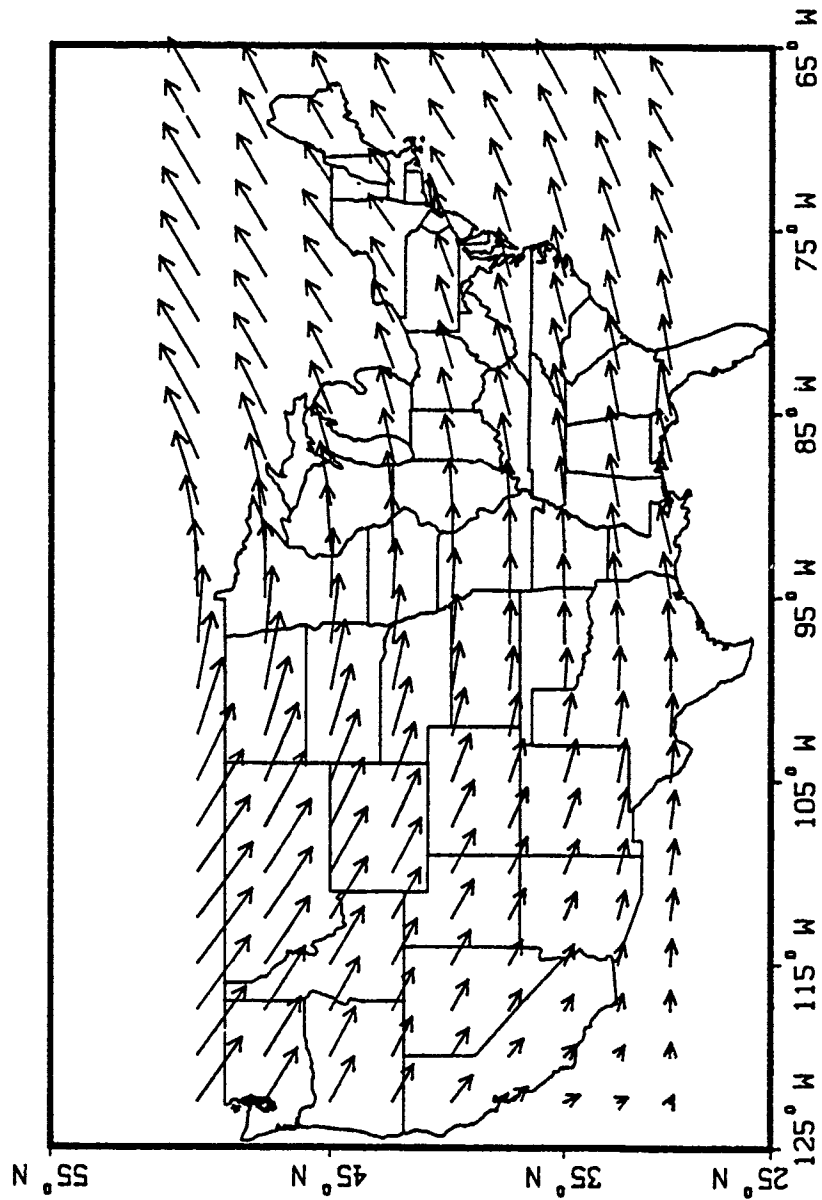
Figure II-12.   Spectral Wind Vector Field, 70 mb
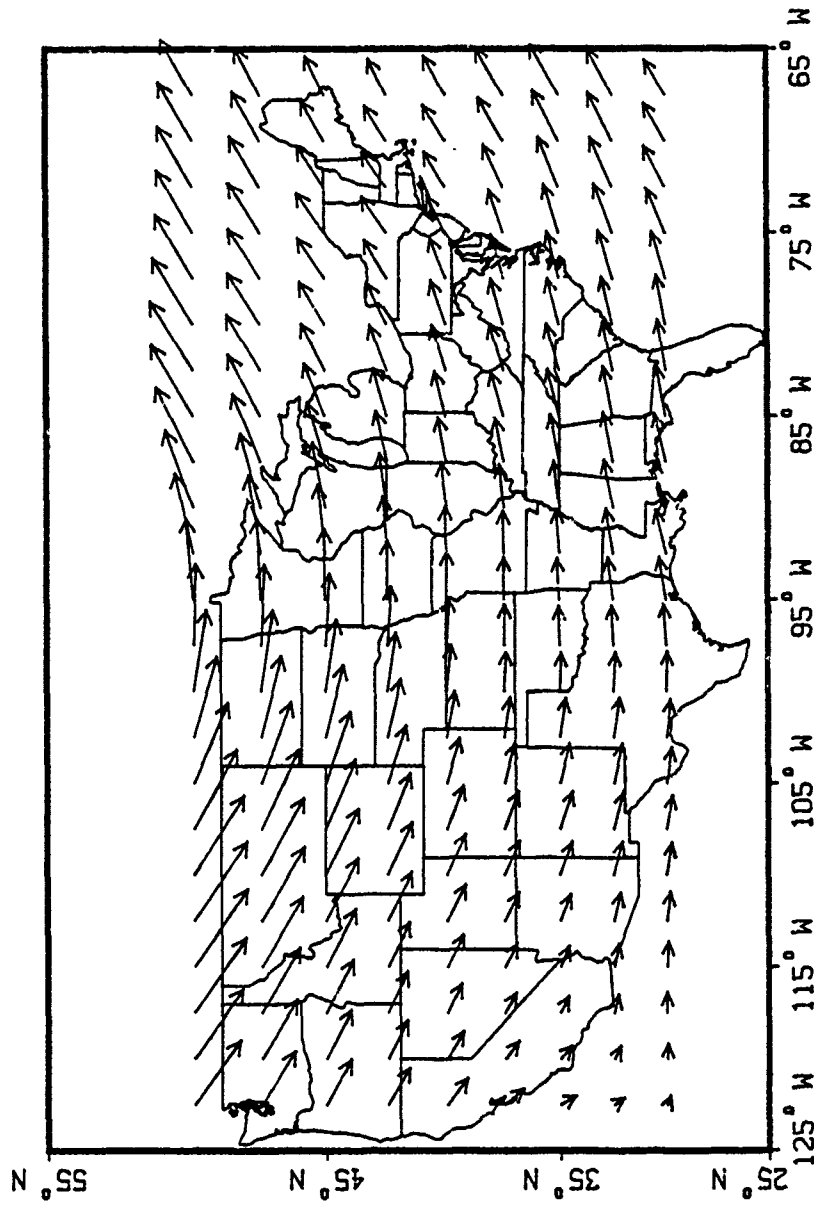
Figure II-13. Spectral Wind Vector Field, 50 mb

22
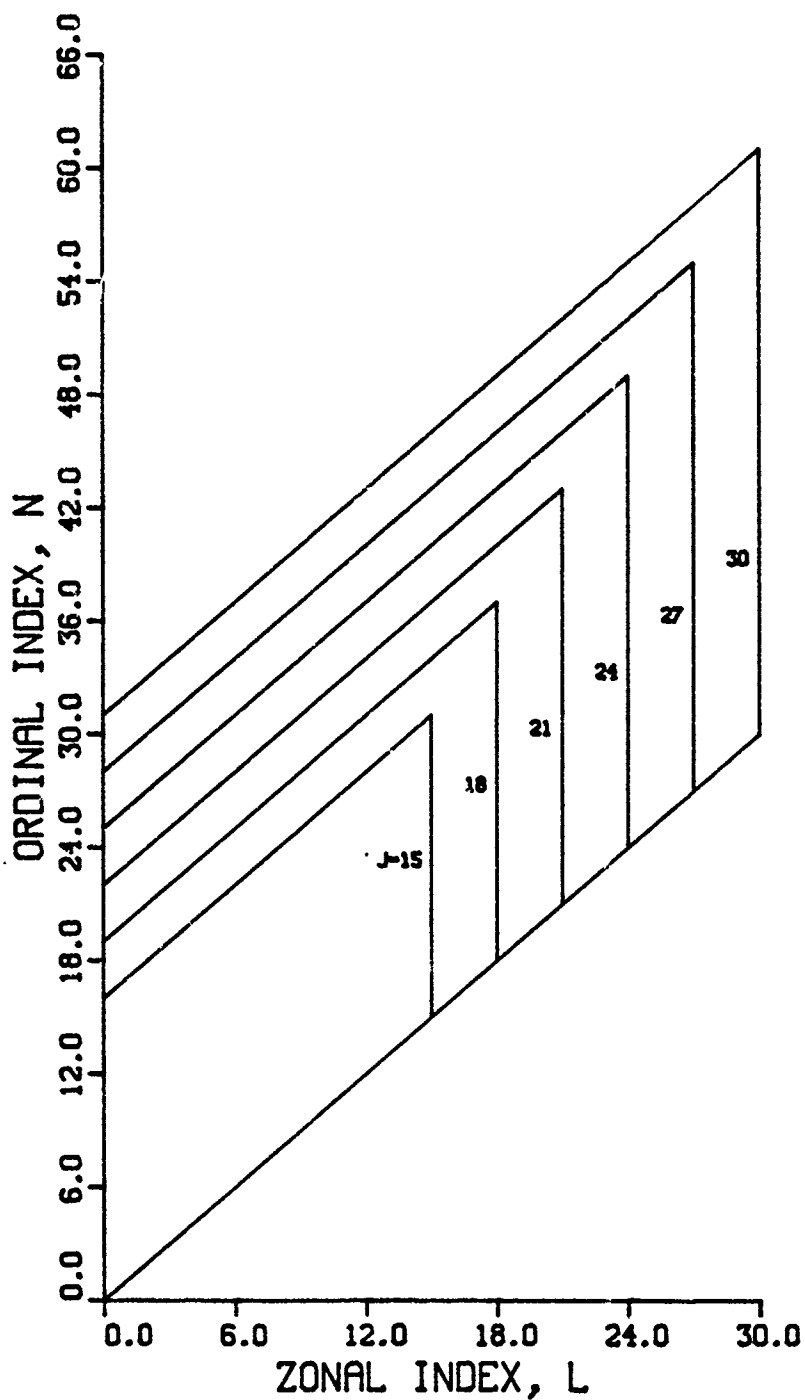
Figure II-14. Alternate Truncations of Summation Indices
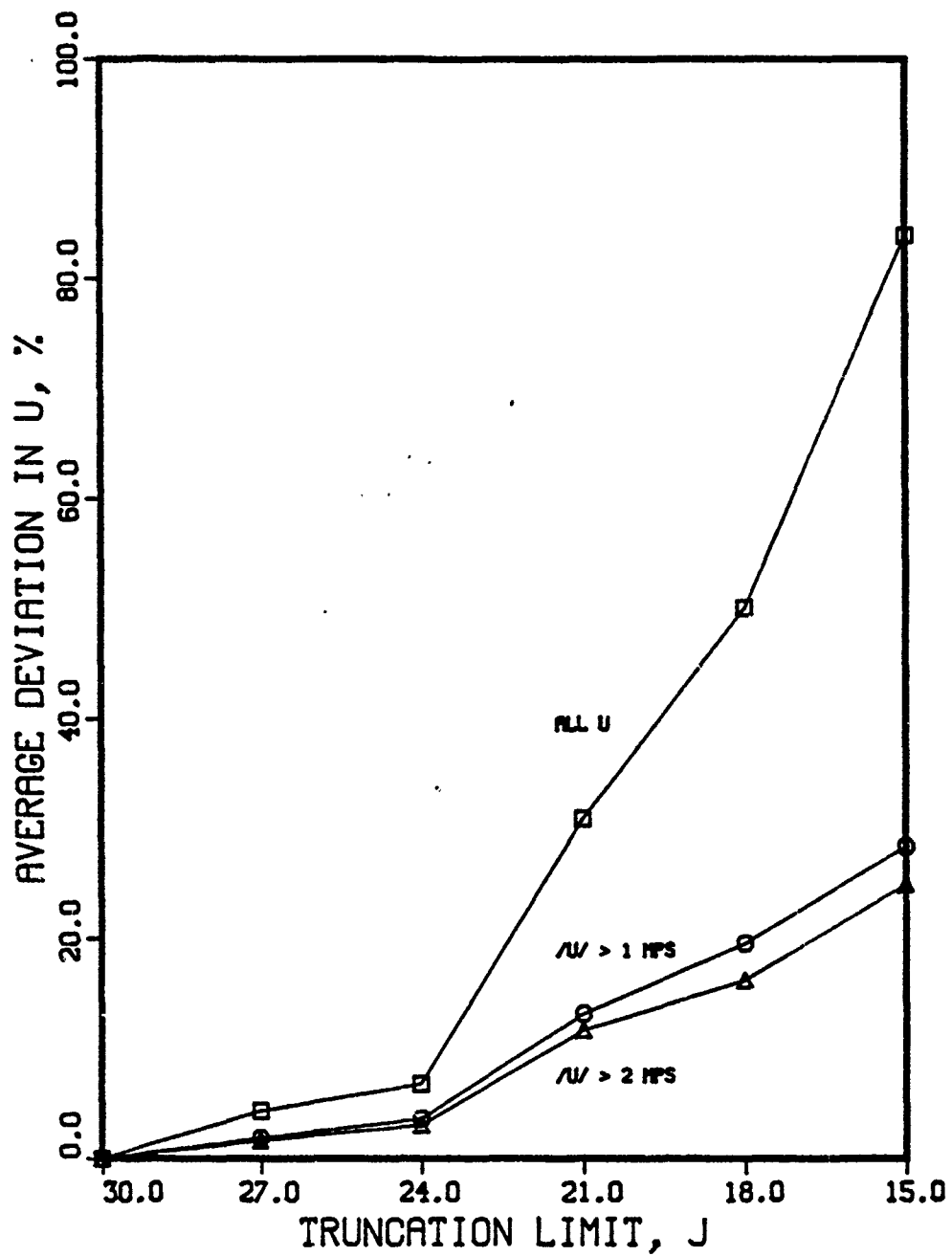
Figure II-15. Truncation Effect on U Wind Component
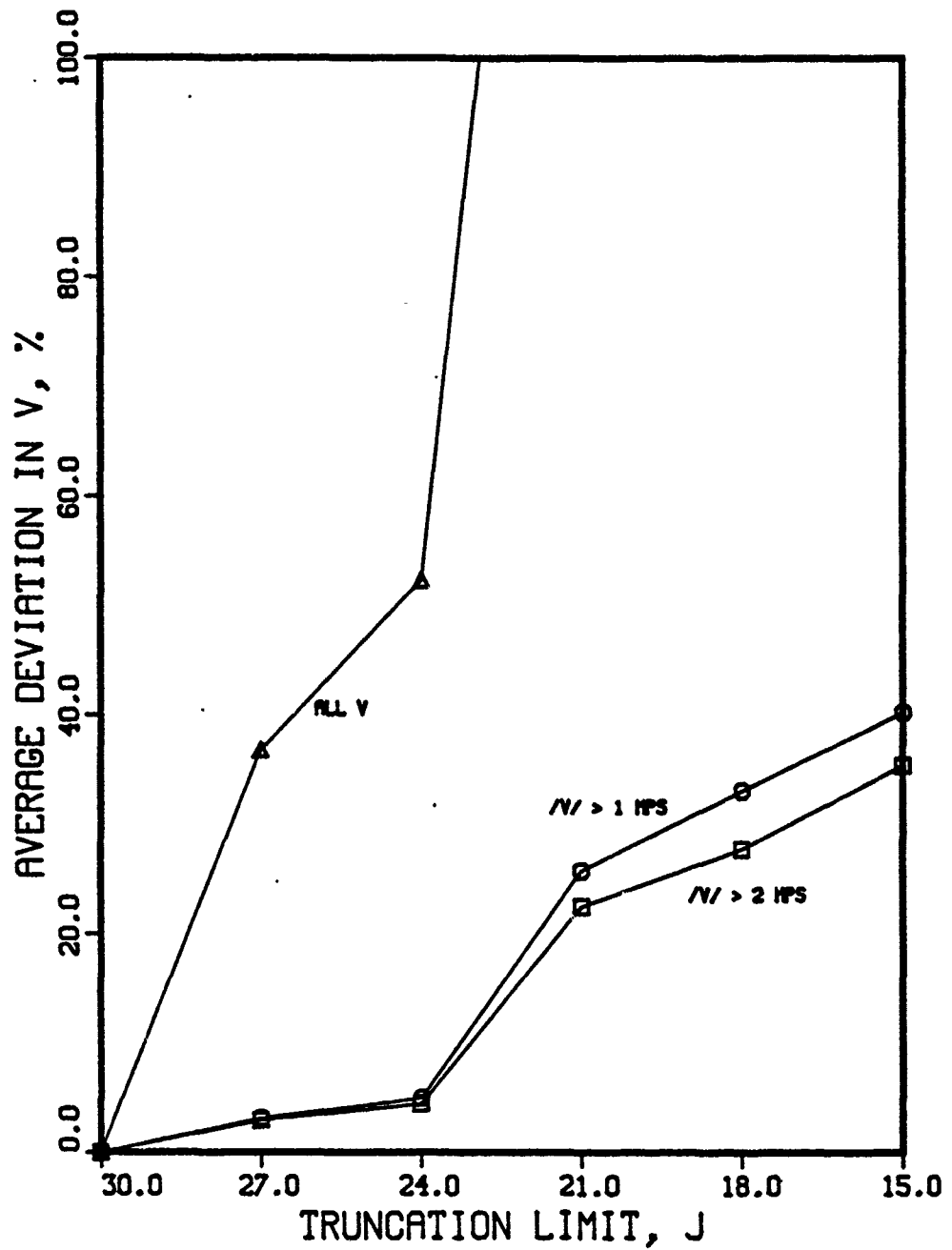
Figure II-16. Truncation Effect on V Wind Component

an average deviation of ±50% (all winds), but only ±5% considering only

winds greater than 1 mps. Abbreviating the summations would require

fewer calculations per component than setting J=30, but the error intro-

duced in low velocity winds may cause large errors in hotline placement.

Spectral wind calculations in this report use J=30.

Accuracy of Spectral Winds

The NMC routinely verifies that the spectral winds do represent

the radiosonde data used to derive the coefficients (70)(108)(109)(110)

(111). A measure of accuracy is the root-mean-squared (rms) vector error:

$$\Delta w = \frac{1}{N-1} \sum_{i=1}^{N} [(u - u_r)^2 + (v - v_r)^2]^{\frac{1}{2}} \tag{2.4}$$

where

Δw = rms vector error
(u,v) = spectral wind components
(u_r,v_r) = radiosonde wind components

The rms vector error is determined by NMC monthly using spectral winds

and radiosonde data. Table II-1 shows the maximum, minimum and average

rms vector errors, for four levels, based on 25 consecutive months' data.

RMS vector errors are derived from data taken by 110 North American

weather observation stations.

The vector errors do not vary significantly with height, but wind

speed generally increases with height. Therefore, the relative error,

ratio of vector error to wind vector magnitude, should decrease with

increasing height. This expectation is validated in Chapter V, with a

comparison between the spectral wind trajectory and the actual trajectory

of a 3 kilometer high cloud.

TABLE II-I

RMS Vector Errors

(Meters per Second)

Level	Altitude	RMS Vector Error		
millibars	kilometers MSL	Avg	Min	Max
850	1.5	4.8	4.0	5.8
500	5.6	4.9	3.8	5.9
250	10.4	6.8	6.0	7.9
100	16.2	3.7	2.9	4.8

III. Hotline Locator Model

A two step method is used to model variable wind effects with a smearing fallout code. First, the hotline is located; then, activity is smeared downwind, along the hotline. This chapter describes how hotline coordinates are computed, using spectral winds. Essentially, a particle array is tracked from the initial stabilized cloud, through spectral winds, to the ground. Wind-driven horizontal displacements of each falling particle are computed and summed through a discretely layered atmosphere. The hotline is the connection of particle landing points. Different sized particles fall from different initial heights with different speeds through different winds, so hotlines may be curved.

Following is a description of the initial cloud, atmosphere discretization and fall-speed calculation used to locate the hotline. Wind shear is also computed along particle trajectories for use in smearing code estimates of cloud spreading. Sample hotlines are shown for hypothetical clouds that start above land-based missile sites in the United States.

Initial Cloud

Initially, the stabilized cloud contains all radioactive particles. The cloud model is a gravity-sorted distribution of particle size vs height, obtained from correlations of DELFIC cloud height data (11). Figure III-1 shows how particle size varies with height in initial clouds produced by five different nuclear weapon yields. Particle size and height in the cloud are linearly related; slopes and intercepts
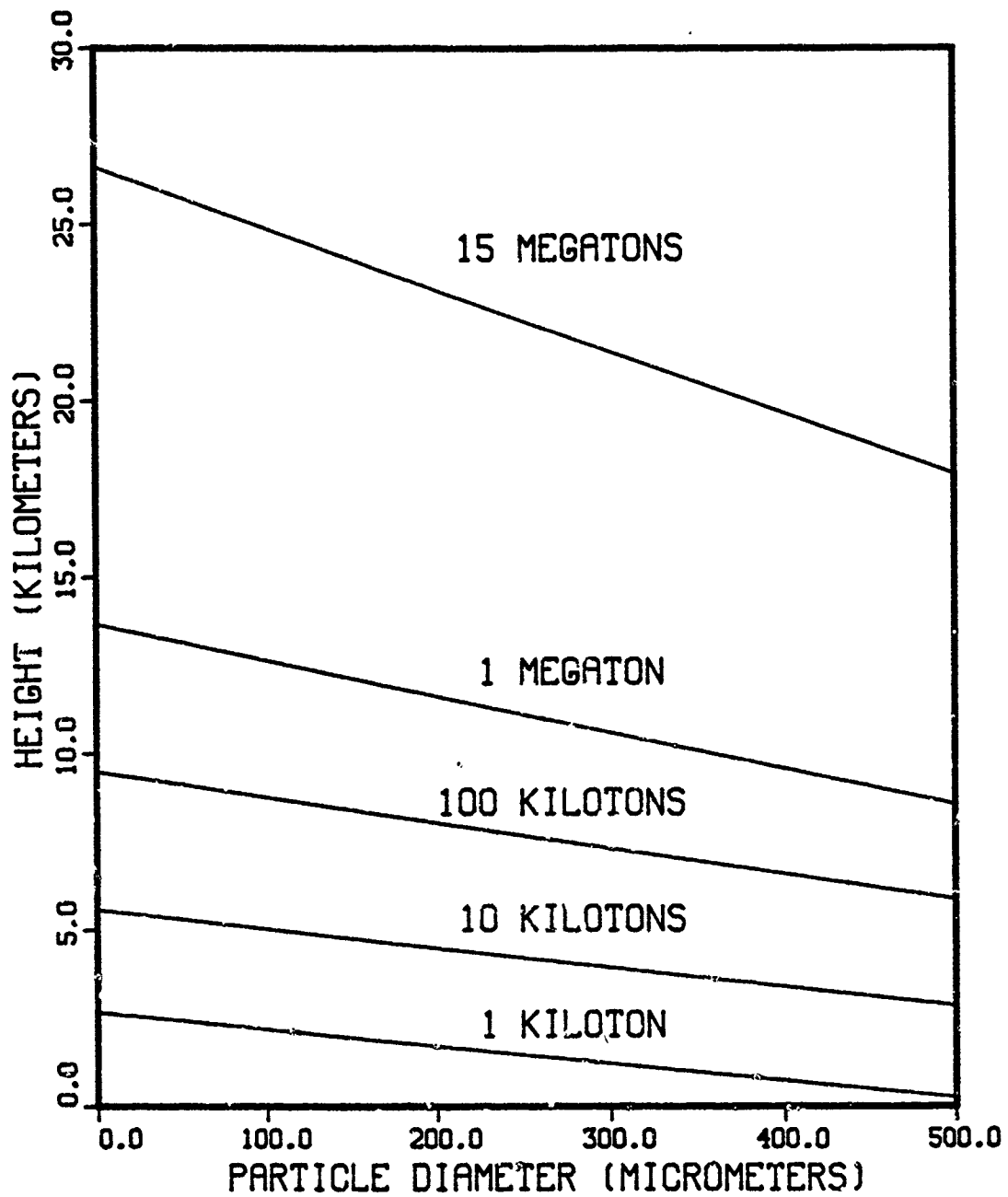
Figure III-1. Average Heights of Particles in DELFIC's Stabilized Clouds

are yield-dependent polynomials. Equations for particle height, slope and intercept are in Appendix C.

Assuming that particle starting heights represent altitudes of peaks in constant-size activity distributions, the ground trace of particles describes the fallout hotline. This assumption was validated in (53) by comparing hotlines from initial cloud correlations with DELFIC results.

In this report, initial clouds are the gravity-sorted clouds shown in Figure III-1. In fact, there are many independent estimates of initial cloud heights, based on numerical and empirical data. The distributed size-height correlations are used because they replicate DELFIC's initial clouds, and they generally agree with observed data. Other initial clouds can and have been used for fallout calculations with analytic codes. Appendix C presents some initial cloud models and shows cloud height sensitivity to weapon yield.

Atmosphere Discretization

The atmosphere is divided into layers of equal thickness beneath the height of the highest (smallest) particle in the initial cloud. Particle trajectory calculations showed that hotline location varied with assumed number and thickness of atmosphere layers in the hotline locator model. However, sensitivity studies with 3, 6, 12, 24, 36, and 48 layer models indicate that hotline coordinates change very little with more than 24 layers.

Hotline coordinates were computed with the six different layer models using the same particle sizes in each model. Coordinates varied less as atmosphere discretization became finer. The deviation in

distance from the burst point was used to quantify the variation in hotline coordinates with number of model layers. See the inset on Figure III-2. Average deviation is the average of deviations of twelve hotline points. Figure III-2 shows how the average deviation decreased with increasing number of model layers. Hotline coordinates were nearly stationary with 24 or more model layers; the average deviation due to increasing the number of model layers above 24 was less than 4%.

Atmosphere properties are computed at each level with state equations for a U.S. Standard Atmosphere (75)(107). The equations are summarized in (53). Particle fall speeds are computed at each level and averaged between levels to obtain a fall speed and residence time in each layer of atmosphere. The product of wind speed and residence time gives displacement within a layer; displacements are summed in all layers between the particle's initial height and the earth surface.

Wind speed at any latitude, longitude and height is computed with spectral coefficients and Eq (2.3). This hotline locator model linearly interpolates (in height) spectral winds to obtain wind vector components in a layer of atmosphere. The interpolated winds transport falling particles to new horizontal coordinates at a lower level in the discrete atmosphere. Figure III-3 shows the relations among the discrete atmosphere, a megaton initial cloud and the spectral wind heights.

Particle Fall Rate

The terminal velocity of each particle must be calculated at each level to obtain the particle's residence time in each discrete layer of atmosphere. Terminal velocities are calculated with the Davies-McDonald method (27)(67)(68). Davies empirically related

31
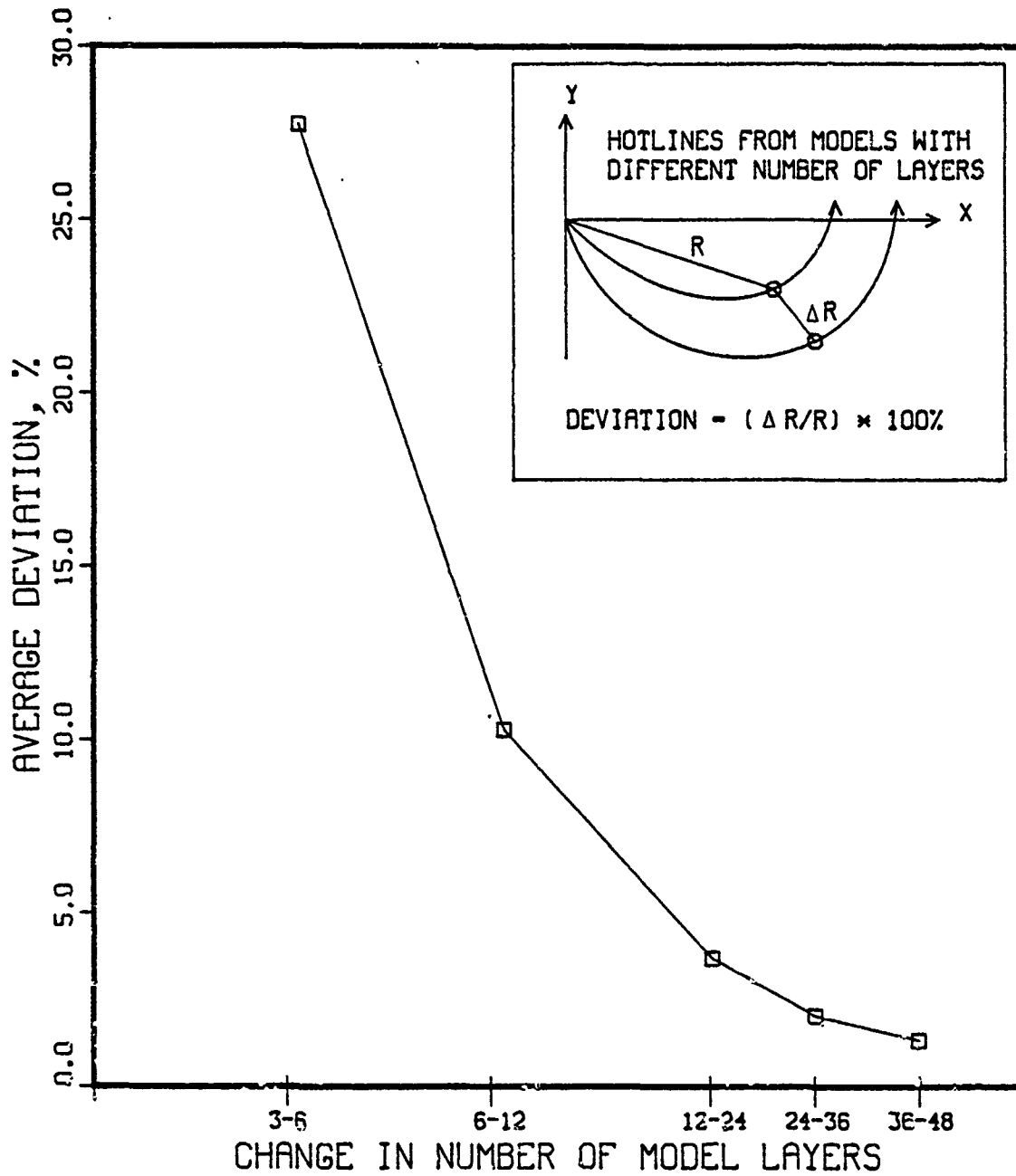
Figure III-2.   Average Deviation of Hotline Coordinates vs
Change in Number of Model Layers

25

LAYER 24

20

15

LEVEL NUMBER

10

5

1

LAYER 1

ATMOSPHERE
LEVELS AND
LAYERS

40
200
400
600
800
1000

CLOUD
PARTICLE
DIA. (μm)

150
200
250
300
400
500
700
850
1000

SPECTRAL
HEIGHTS
(MILLIBARS)

HEIGHT (KILOMETERS)

10
5
1
0
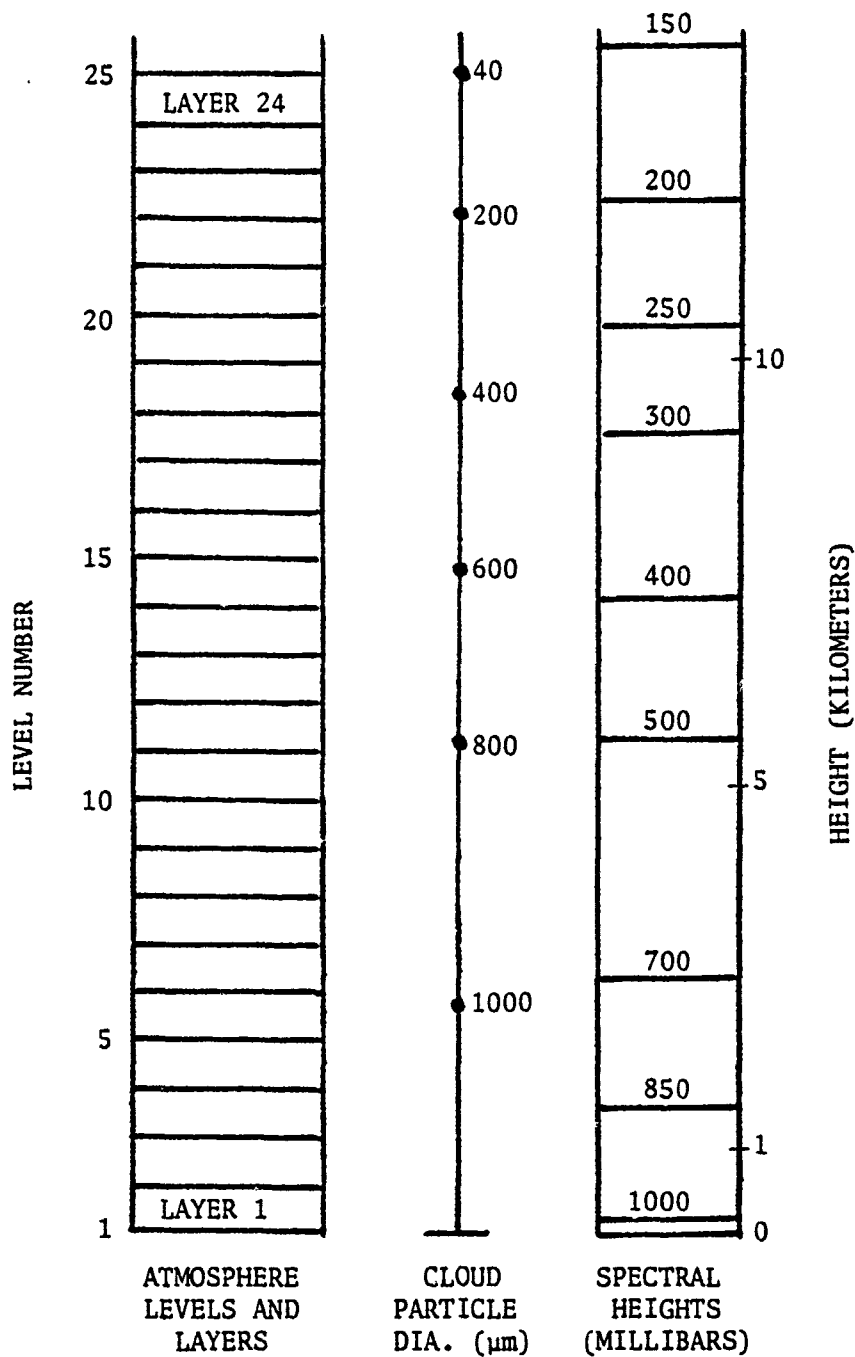
Figure III-3. Atmosphere Discretization, Initial Cloud and Spectral
Heights in Hotline Locator Model

the Reynolds number, Re, of a moving sphere to $C_D Re^2$; C_D is the particle's drag coefficient. McDonald described an algorithm to compute the quantity $C_D Re^2$ from particle size, particle density, atmospheric density and kinematic viscosity. Using $C_D Re^2$ to obtain Re, terminal velocity is computed as follows:

$$V_z = Re \; \nu/d \qquad (3.1)$$

where

   V_z = terminal velocity
   Re = Reynolds number
   ν = atmospheric kinematic viscosity
   d = particle diameter

The equations assume that particles are spheres of constant density falling through the discretely layered atmosphere. Figure III-4 shows the total fall time of ten different sized particles from heights up to 18 kilometers above sea level in a U.S. Standard Atmosphere.

Wind Shear

Vertical wind shear is a measure of the wind field's dispersive effect on the falling cloud. Components of the shear vector are defined as follows (43)(48):

$$s_x = \Delta u/\Delta z \qquad (3.2)$$

$$s_y = \Delta v/\Delta z \qquad (3.3)$$

where

   s_x = vertical shear (westerly)
   s_y = vertical shear (southerly)
   Δz = finite thickness of atmosphere
   $(\Delta u, \Delta v)$ = wind component variations over Δz
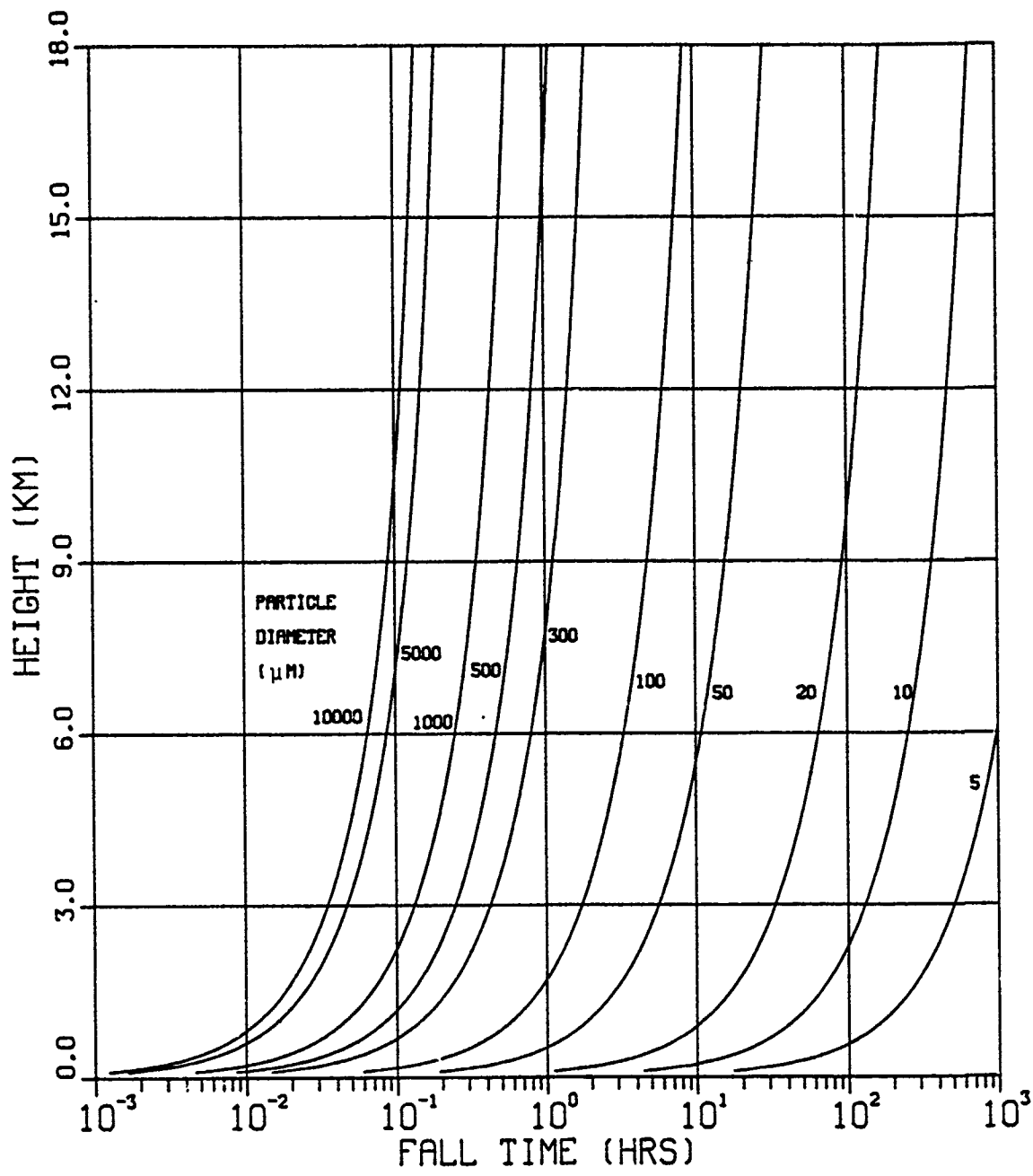
Figure III-4. Particle Fall Times from Heights up to 18 Kilometers

35

Wind shear is a characteristic frequency with which atmospheric turbu-

lence acts on the cloud (6)(7). For nuclear clouds, the turbulence scale

is assumed to be a fraction of the initial cloud thickness. Fallout

codes usually assume a constant shear value for the life of the cloud

(86). The constant shear is typically either a guess or a number cal-

culated from the vertical profile that was used to compute the constant,

'effective' wind.

However, spectral winds permit separate shear calculations for

each point on the hotline. Shear then represents the net dispersive

effect of cloud-scale turbulence on individual particle size groups

in separate trajectories. For each hotline point (or particle size),

shear is computed as follows:

$$(S_x, S_y) = \left[\sum_i (s_x, s_y)_i^2 \frac{t_i}{TFALL} \right]^{\frac{1}{2}}$$

(3.4)

where

(S_x, S_y) = net (rms) shear in trajectory
t_i = residence time of particle in layer i
TFALL = total fall time of particle from initial cloud to ground

Net shear (S_x, S_y) is the rms value of shears determined over discrete

layers of atmosphere, weighted by the residence time of each particle

in each layer of atmosphere.

Sample Hotlines

Figure III-5 shows hotlines computed with a twenty-four layer hot-

line locator model that tracks twenty particles. The model uses spectral

coefficients to compute the winds that transport falling particles in a

U.S. Standard Atmosphere. Initial earth coordinates of the stabilized

36
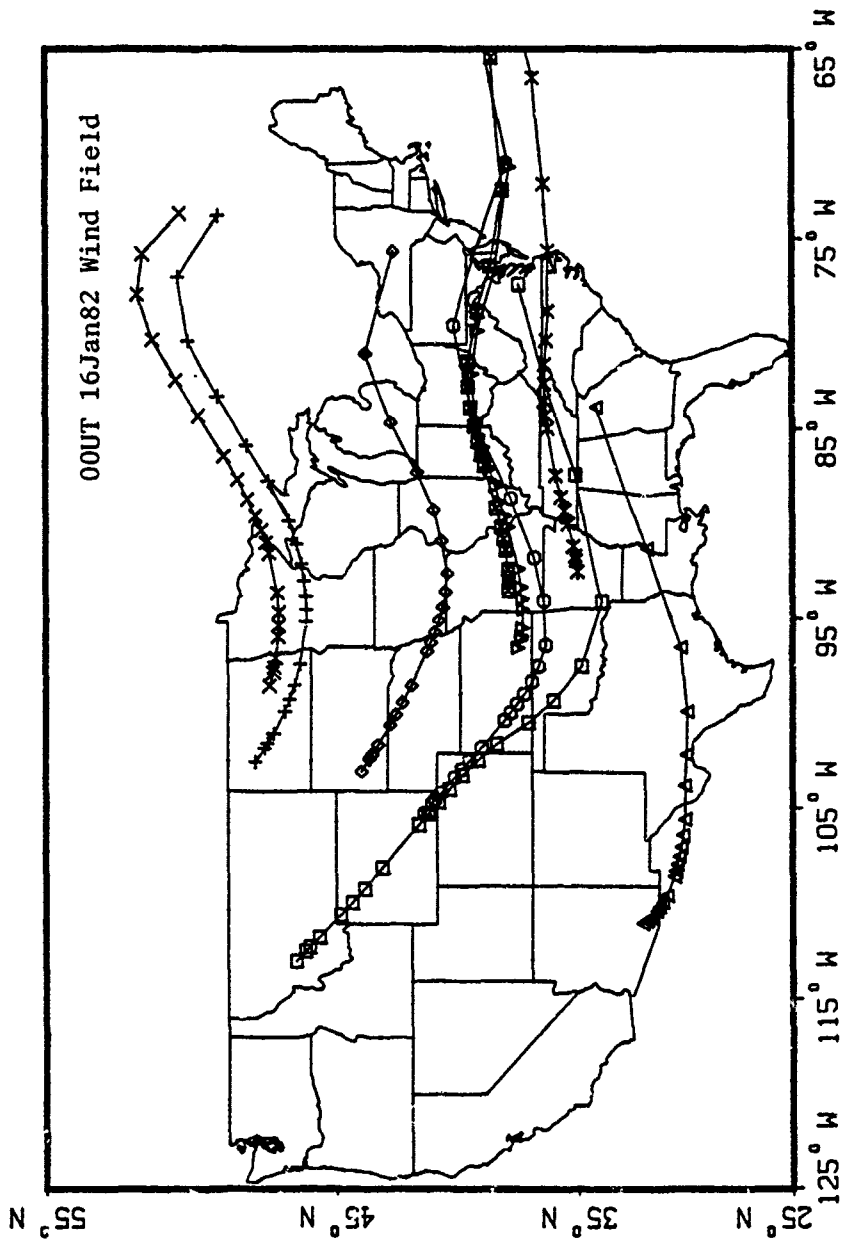
Figure III-5. Curved Hotlines with Variable Winds in Hotline Locator Model

cloud are specified as colatitude and longitude east of Greenwich in radians. The hotlines are continuous and realistically curved. Points on the hotline are landing spots of different particle sizes; large particles fall closer to the burst point.

Summary

A hotline locator model was developed to compute hotline coordinates. The model uses spectral wind coefficients to compute wind vectors and shear along the trajectories of falling particles. Sensitivity studies show that computed hotline points converge to stationary locations as the number of atmospheric layers increase. Twenty-four discrete layers beneath the highest particle in the initial cloud give adequate convergence. Wind shear is computed from each particle's unique trajectory winds. Sample hotlines are continuous and realistically curved.

Key model assumptions are as follows:

(1) U.S. Standard Atmosphere
(2) Linear vertical interpolation of winds between spectral heights
(3) No updrafts or downdrafts
(4) Constant density (2.6 grams per cubic centimeter) spheres

These assumptions were made to generate the illustrative hotlines shown here. Actually, any appropriate atmosphere, interpolation scheme, vertical velocity and particle density can be used to compute hotline location.

IV. Variable Wind Smearing Model

This chapter describes the second step necessary to determine fall-out dose rate with variable winds. A fallout smearing model is presented that determines ground coordinates of dose rate contours around curved hotlines. Curved hotline coordinates were computed separately in the first step with the hotline locator model (Chapter III), using spectral winds for particle transport.

Existing smearing codes use a constant wind vector to transport a falling cloud of radioactive particles unidirectionally downwind. The one dimensional dose rate equation for smearing codes cannot be used with variable winds because a constant wind was assumed to obtain the analytic solution for dose rate (19). With variable winds, cloud activity is smeared along a curved hotline, using a new analytic solution to the dose rate integral.

Following sections describe the dose rate equation, its activity arrival rate term and its spatial distribution term. A method is developed to compute dose rate at any specified ground location. Sample contours of constant dose rate about curved hotlines are shown.

Dose Rate Equation

Dose rate is computed with an analytic solution to the dose rate integral, Eq (1.1). Following is the dose rate equation:

$$\dot{D} = \frac{k \ Y \ ff \ g(ta)}{\sqrt{2\pi}} \ (\sigma_x^2 \ V_y^2 + \sigma_y^2 \ V_x^2)^{-\frac{1}{2}} \ EXP \left(-\frac{1}{2} \ \frac{(x \ V_y - y \ V_x)^2}{\sigma_x^2 \ V_y^2 + \sigma_y^2 \ V_x^2} \right) \quad (4.1)$$

where

k = source normalization constant
Y = kilotons of weapon yield
ff = fraction of weapon yield from fission
g(ta) = arrival rate of activity on ground (hour^{-1})
(X,Y) = hotline coordinates (miles from burst point)
(x,y) = ground coordinates where dose rate is calculated
   (miles from burst point)
(V_x, V_y) = net wind components from burst point to hotline
   point (X,Y) (miles/hour)
(σ_x, σ_y) = deviations of cloud activity distributions (miles)

note: x direction is positive eastward
   y direction is positive northward

Eq (4.1) was obtained by assuming that cloud activity is distributed normally in two directions, and that the arrival rate function, g(t), can be approximated with a two-term Taylor expansion about arrival time, ta (19)(53). Furthermore, analytic integration of Eq (1.1) required that dose rate be computed at points distant from the burst point.

A constant, unidirectional wind is simulated when $V_y = 0$ and $V_x =$ constant at all hotline points. The dose rate equation then reduces to the unidirectional, constant wind form in (19); setting $V_y = 0$, the dose rate equation becomes:

$$\dot{D} = \frac{k \ Y \ ff \ g(ta)}{\sqrt{2\pi} \ \sigma_y \ V_x} \ EXP \left[-\tfrac{1}{2} \ \frac{y^2}{\sigma_y^2} \right] \tag{4.2}$$

Activity Arrival Rate

Cloud activity is smeared along the ground as the falling cloud translates with the winds. The activity arrival rate function, g(t), is the functional rate of arrival of activity on the ground (19).

$$g(t) = -A(r) \ \frac{dr}{dt} \tag{4.3}$$

40

Assuming that a log-normal distribution describes the particle number-size frequency in the cloud, the activity-size distribution function can be expressed as the sum of two distributions (2)(19).

$$A(r) = A_3 + A_2 \tag{4.4}$$

$$A_3 = \frac{fv}{\sqrt{2\pi}\ \beta_3\ r}\ EXP\left[-\tfrac{1}{2}\left(\frac{\ln r - \alpha_3}{\beta_3}\right)^2\right] \tag{4.5}$$

$$A_2 = \frac{1 - fv}{\sqrt{2\pi}\ \beta_2\ r}\ EXP\left[-\tfrac{1}{2}\left(\frac{\ln r - \alpha_2}{\beta_2}\right)^2\right] \tag{4.6}$$

where

fv = fraction of cloud activity that is volume-distributed in particles
$1-fv$ = fraction of cloud activity that is surface-distributed on particles
r = particle radius
β = slope of log-normal distribution
$\alpha_n = \alpha_o + n\ \beta^2$ = logarithm of median radius in n^{th} moment distribution
$\alpha_o = \ln r_o$ = logarithm of median radius in particle number-size frequency distribution
$\frac{dr}{dt}$ = time derivative of particle radius arriving on ground

A(r) thus represents the fractionation or apportionment of cloud activity onto the surfaces (A_2) and throughout the volumes (A_3) of the particles. Figure IV-1 shows A_3, A_2 and A(r) for typical values of $fv = 0.68$, $\beta = 1.386$ and $r_o = 0.204$ (17)(19)(78). Figure IV-2 shows the same activity distributions weighted by particle radius.

The time derivative of particle size arriving at each hotline point, dr/dt, is computed with a Laurent series developed to compute the particle size arriving from the initial cloud at specified times (24).
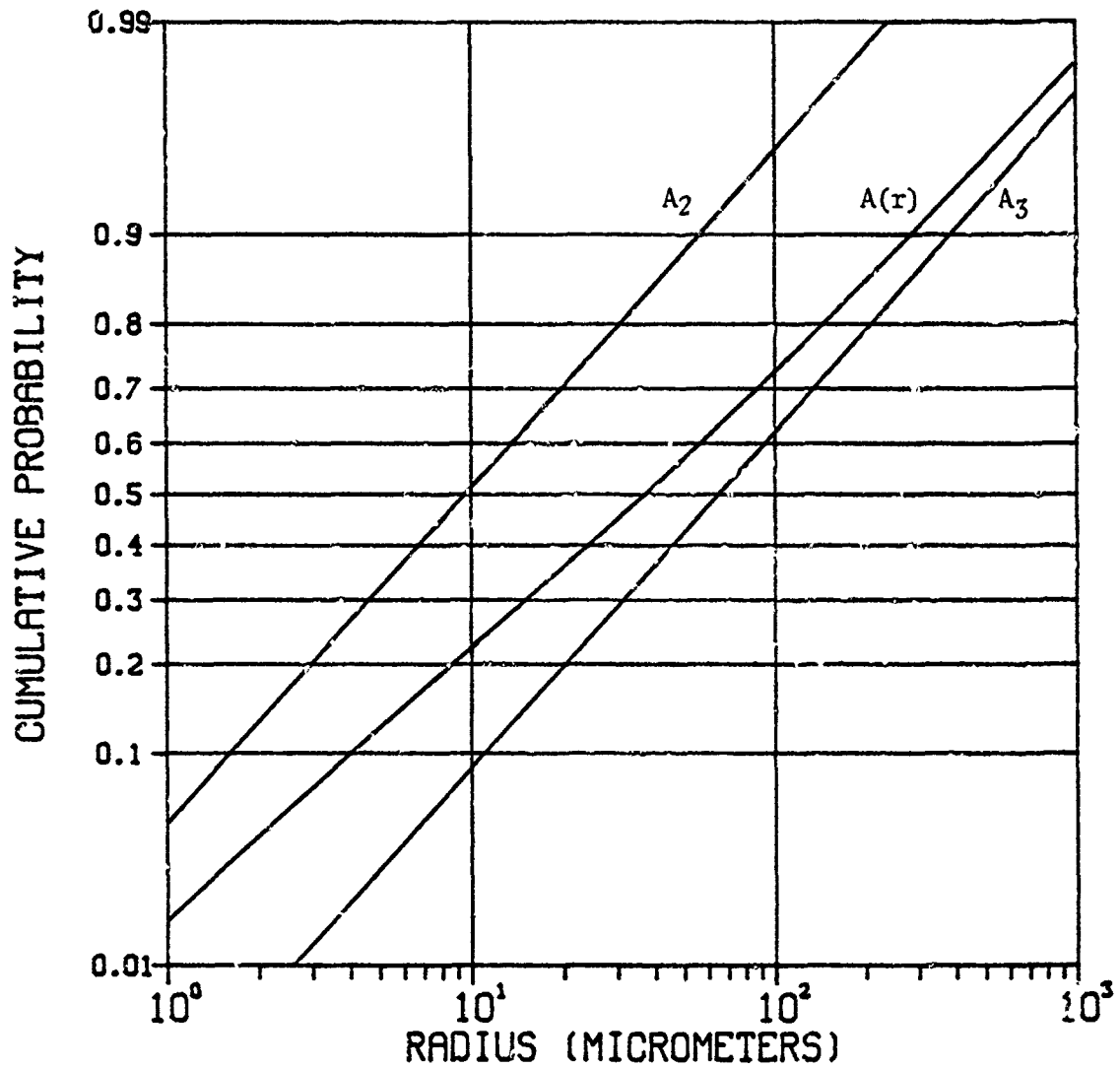
Figure IV·1. Particle Activity-Size Distributions for Nuclear Cloud

42
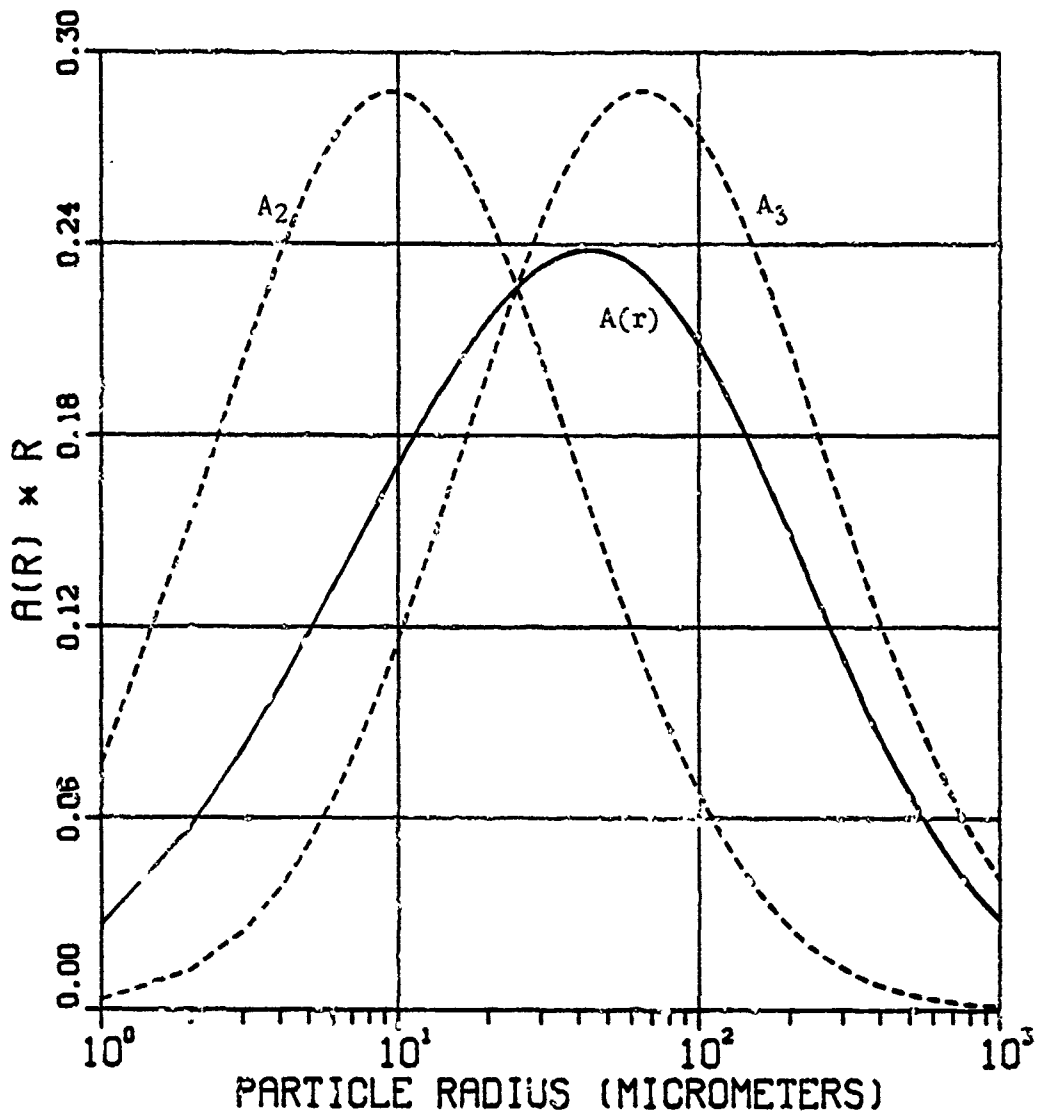
Figure IV-2. Particle Activity-Size Distributions
Weighted with Particle Size

43

$$\frac{dr}{dt} = \sum_{i=1}^{5} C_i (i-6) t^{i-7} - \frac{1}{2} C_7 t^{-\frac{3}{2}} \qquad (4.7)$$

where

C_i = Laurent series constants (height dependent)
t = arrival time of particle size r from a specified height

Each Laurent series constant (C_1 through C_7) was correlated with height, so each constant can be computed with a sixth degree polynomial. The polynomials eliminate the need for tabular searches for C_i values. Appendix D contains the polynomial constants needed to calculate the Laurent series constants.

Since particles in the initial cloud are gravity-sorted, different particle sizes fall from different initial heights. A different set of Laurent series constants for each particle size can be computed with the polynomials. Thus, the distributed initial cloud is modeled with a stack of pancake clouds, one for each particle size. The pancake clouds are simple, accurate approximations of vertical activity distributions that are symmetric about the pancake cloud height (12). The pancake cloud computations of dr/dt with Laurent series are appropriate only for fallout particles with mass densities of 2.6 grams per cubic centimeter.

For other particle mass densities, dr/dt can be computed with the discrete particle arrival times generated by the hotline locator. Numerical differentiation using r and t, can produce any dr/dt along the hotline (74). Figure IV-3 shows dr/dt computed three ways for a megaton initial cloud: (1) Laurent series for pancake cloud, (2) Laurent series for a stack of pancake clouds at DELFIC distributed heights, and (3) numerical derivatives (central differences). Numerical values of
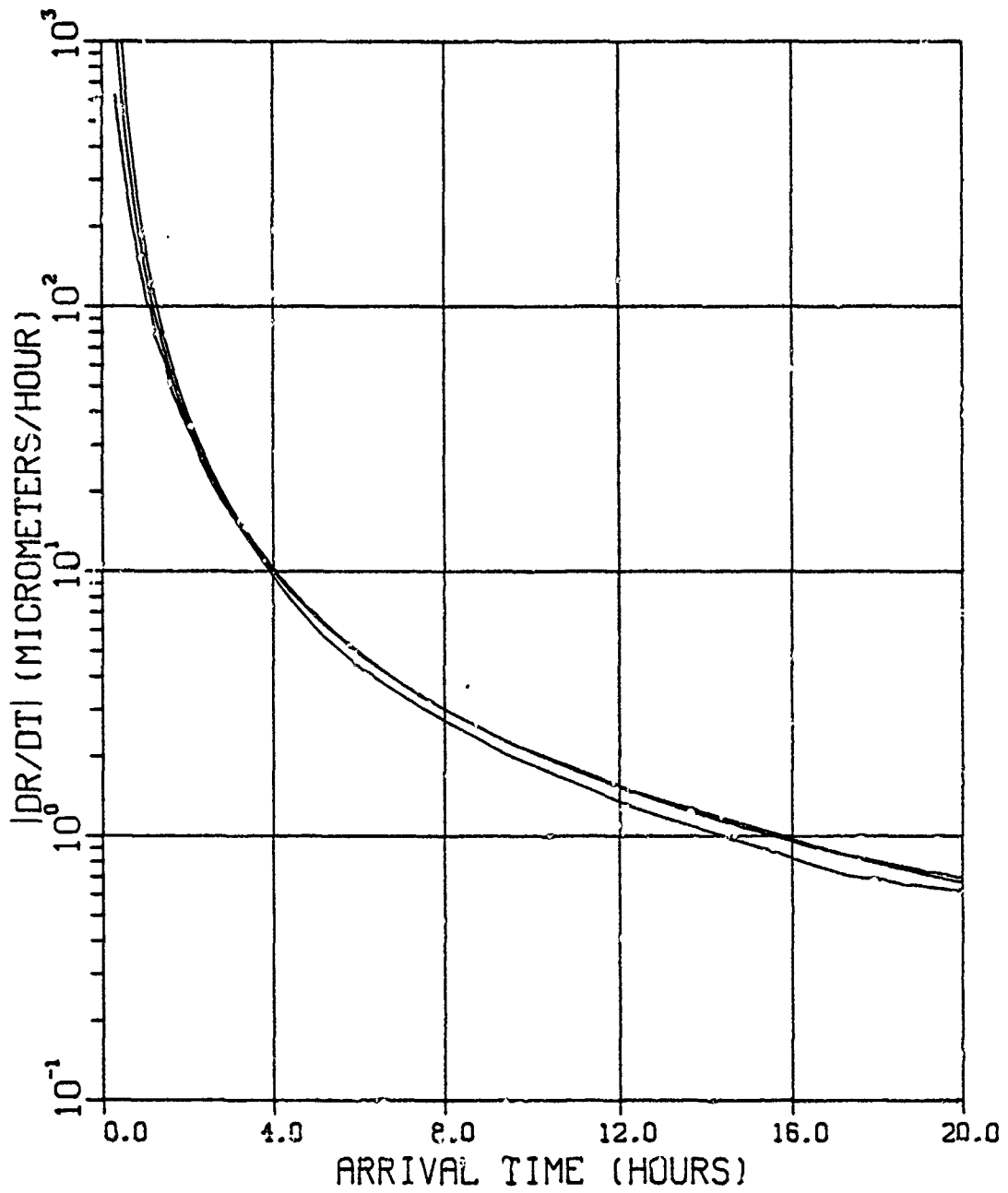
Figure IV-3. Time-Derivative of Particle Size
Arriving from Initial Cloud

45

dr/dt were computed with radii and arrival times from a hotline location calculation. Distributed clouds give essentially the same dr/dt as a simple pancake initial cloud, except at early times (< 1 hour) when large particles are arriving from low altitudes.

Spatial Distribution

The spatial distribution function describes the lateral distribution of activity in the cloud.

$$F_{xy} = \frac{1}{\sqrt{2\pi}\ \sigma_V} \text{ EXP } \left[-\frac{1}{2} \left(\frac{x\ V_y - y\ V_x}{\sigma_V} \right)^2 \right] \tag{4.8}$$

$$\sigma_V^2 = \sigma_x^2\ V_y^2 + \sigma_y^2\ V_x^2 \tag{4.9}$$

Figure IV-4 illustrates F_{xy} over a plane, with constant net wind components, V_x and V_y.

This two directional normal distribution defines the spread of activity along a line perpendicular to the net wind vector (8). Figure IV-5 shows the geometry of the net wind and crosswind lines.

The ground position (x,y) is on the net crosswind line. Activity is smeared simultaneously onto the net crosswind lines as the cloud moves downwind along the hotline. The spatial distribution function, F_{xy}, contains a normalized Gaussian spread in the net crosswind direction. Dispersing clouds in the atmosphere are typically modeled with normal lateral distributions. Data from aircraft sampling supports this Gaussian model (29). Appendix F contains an integration of F_{xy} along a net crosswind line, illustrating normalization in the crosswind direction.

46
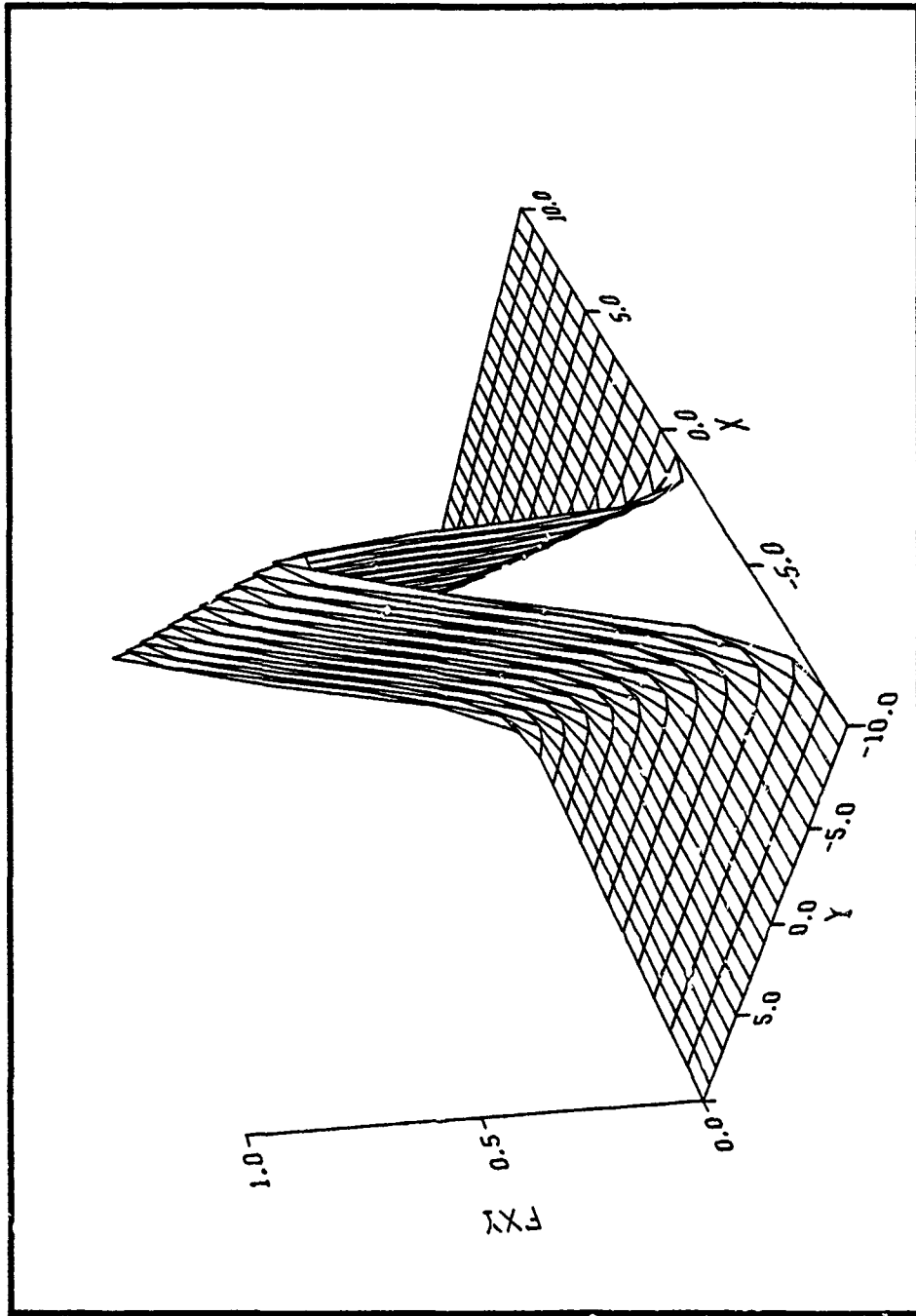
Figure IV-4. Three Dimensional Plot of Spatial Distribution Function
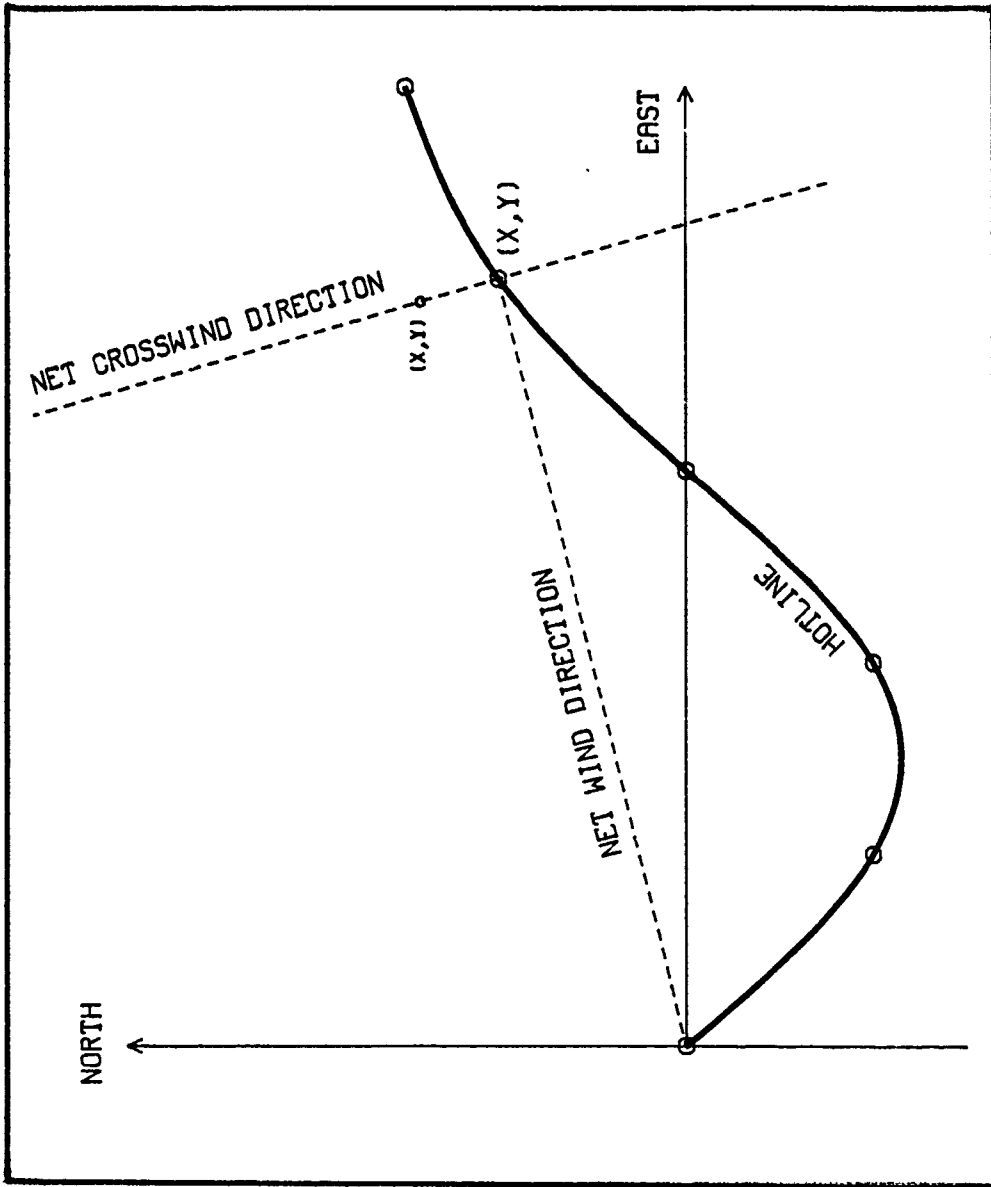
Figure IV-5. Net Wind and Hotline Geometry

The deviation, σ_v , suggests an ellipse-shaped ground intercept of the cloud with eccentricity determined by net wind components and directional deviations. In fact, dispersion theory and observations of nuclear clouds suggest an ellipse-shaped spatial distribution. Aircraft sample data from nuclear clouds produced by Chinese atmospheric nuclear tests showed that debris clouds were ellipse-shaped in horizontal directions at aircraft altitudes (104).

Lateral Deviations

Standard deviations of the fallout cloud activity are specified in the x and y directions; x is positive eastward and y is positive northward. The deviations are functions of initial cloud size, toroidal growth and wind shear effects. The initial cloud size is determined by weapon yield. Toroidal growth continues until the cloud's internal flow stops. Late time cloud growth is driven by wind shear. Following are equations for crosswind deviation, σ_y , given by Pugh (86) for a constant wind, V_x:

$$\sigma_y^2 = \sigma_0^2 \left(1 + 8 \frac{Ts}{Tc} \right) + \left(t \, S_y \, \sigma_h \right)^2 \qquad (4.10)$$

where

σ_0 = initial cloud parameter

$$\ln \sigma_0 = 0.7 + \frac{\ln Y}{3} - 3.25 / \left[4.0 + \left(\ln Y + 5.4 \right)^2 \right] \qquad (4.11)$$

Y = yield (megatons)
Ts = elapsed time for toroidal growth = t   if   t $\leq$ 3 hours
Tc = effective e-folding time for activity arrival on the ground; based on exponential g(t) in Pugh (86)

$$= 12 \left(\frac{HC}{60} \right) - 2.5 \left(\frac{HC}{60} \right)^2 \qquad \text{(hours)}$$

49

$$HC = 44.0 + 6.1 \ln Y - 0.205 (\ln Y + 2.42) |\ln Y + 2.42| \qquad \text{(kilofeet)}$$

$\sigma_h = 0.18 \ HC$

t = cloud arrival time

S_y = wind shear in y direction $\qquad$ (hours^{-1})

The first term in Eq (4.10) models toroidal growth, which is assumed to stop at 3 hours after the burst. The second term represents growth due to wind shear. Figure IV-6 shows how σ_o, Tc and HC vary with weapon yield.

With variable winds, downwind is not likely to be in the x direction at all times. The spatial distribution function, F_{xy}, requires σ_y and σ_x to determine the crosswind spread of activity. Therefore, σ_x is computed with an equation analogous to σ_y.

$$\sigma_x^2 = \sigma_o^2 \left(1 + 8 \frac{Ts}{Tc} \right) + (t \ S_x \ \sigma_h)^2 \qquad (4.13)$$

The x and y direction shears are computed from spectral winds using the hotline locator model. Shear is determined along each particle's unique trajectory through variable winds.

In general (after 3 hours), σ_x and σ_y are proportional to t. This linear dependence is stronger than diffusion theory predicts. Many models of cloud dispersion in the atmosphere assume Fickian diffusion (20)(96), and the analytic solution to the diffusion equation gives a Gaussian form with σ defined as follows:

$$\sigma = (2 \ K \ t)^{\frac{1}{2}} \qquad (4.14)$$

where

σ = standard deviation of cloud distribution

K = coefficient of eddy diffusivity
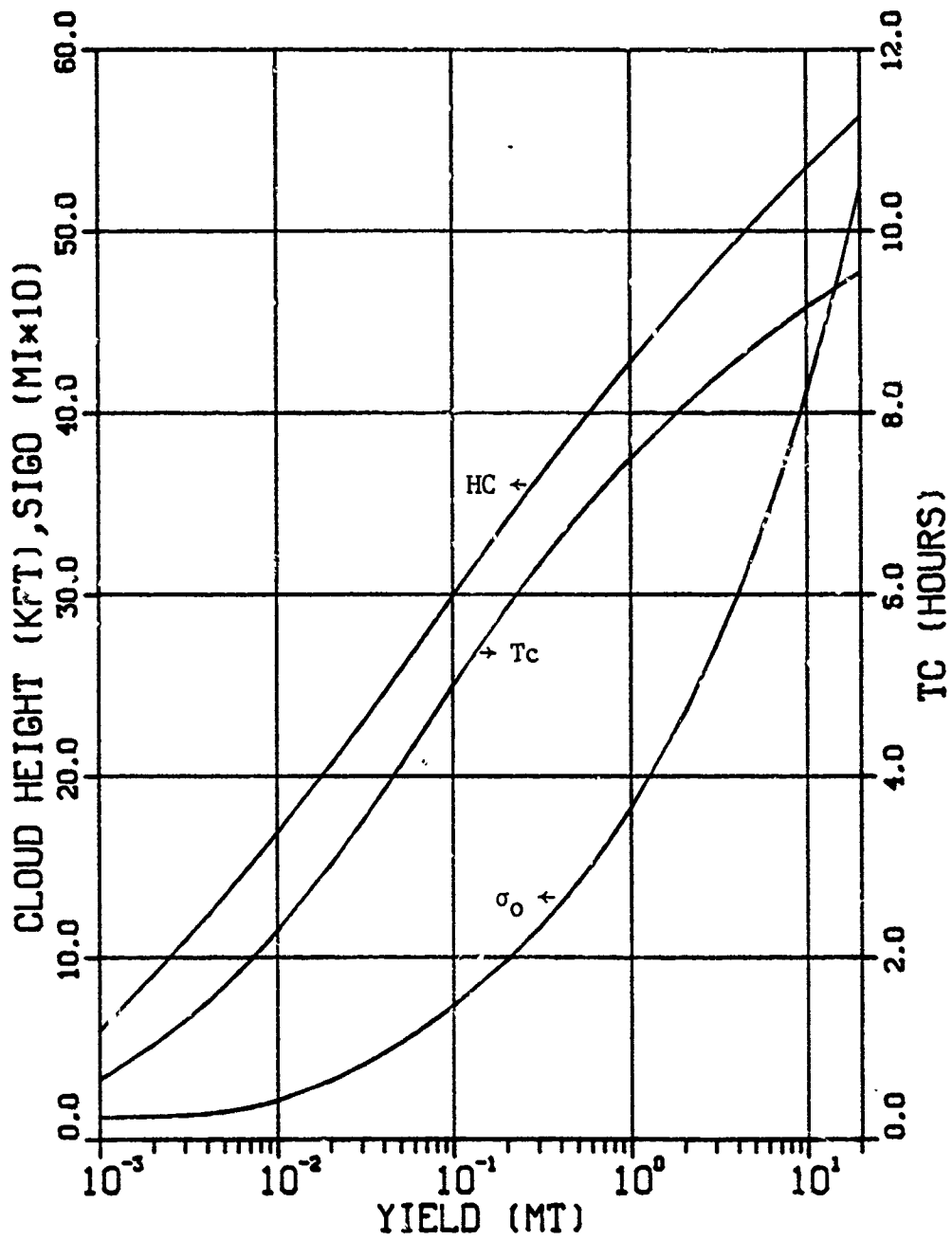
Figure IV-6. WSEG Yield-Dependent Parameters

51

Eddy diffusivity coefficients have been estimated for nuclear clouds (6) (64). With falling particles, the cloud dispersion process is affected by vertical wind shear, so the diffusivity, K, must be an effective value accounting for shear, fall and diffusion (63)(102)(117).

Sample contours in this report were computed with Pugh's specification for σ_y, because his formula was based on nuclear cloud data and because it contains explicit weapon yield dependence.

Dose Rate Calculations

The variable wind smearing model determines fallout dose rate at a point. Coordinates of a desired dose rate are found by marching away from hotline points (X,Y), along net crosswind lines, until computed dose rate at (x,y) is the desired level. Figure IV-7 shows the geometry for finding a dose rate contour; the line connecting each point (x,y) is the contour. Figure IV-8 shows 0.3 Roentgen/hour dose rate contours computed with the curved hotlines shown in Chapter III.

To compute dose rate at any arbitrary ground point (x,y), it is necessary to find the hotline point (X,Y) that is connected to (x,y) on a crosswind line. Using the fact that the burst point (0,0), hotline point (X,Y) and ground point (x,y) form a right angle, a method was developed to find (X,Y) for any (x,y). Appendix F presents the technique for finding the hotline point (X,Y) associated with any ground point (x,y). Figure IV-9 shows a three-dimensional dose rate surface computed with this technique at 1000 arbitrary points downwind of a megaton yield nuclear burst.
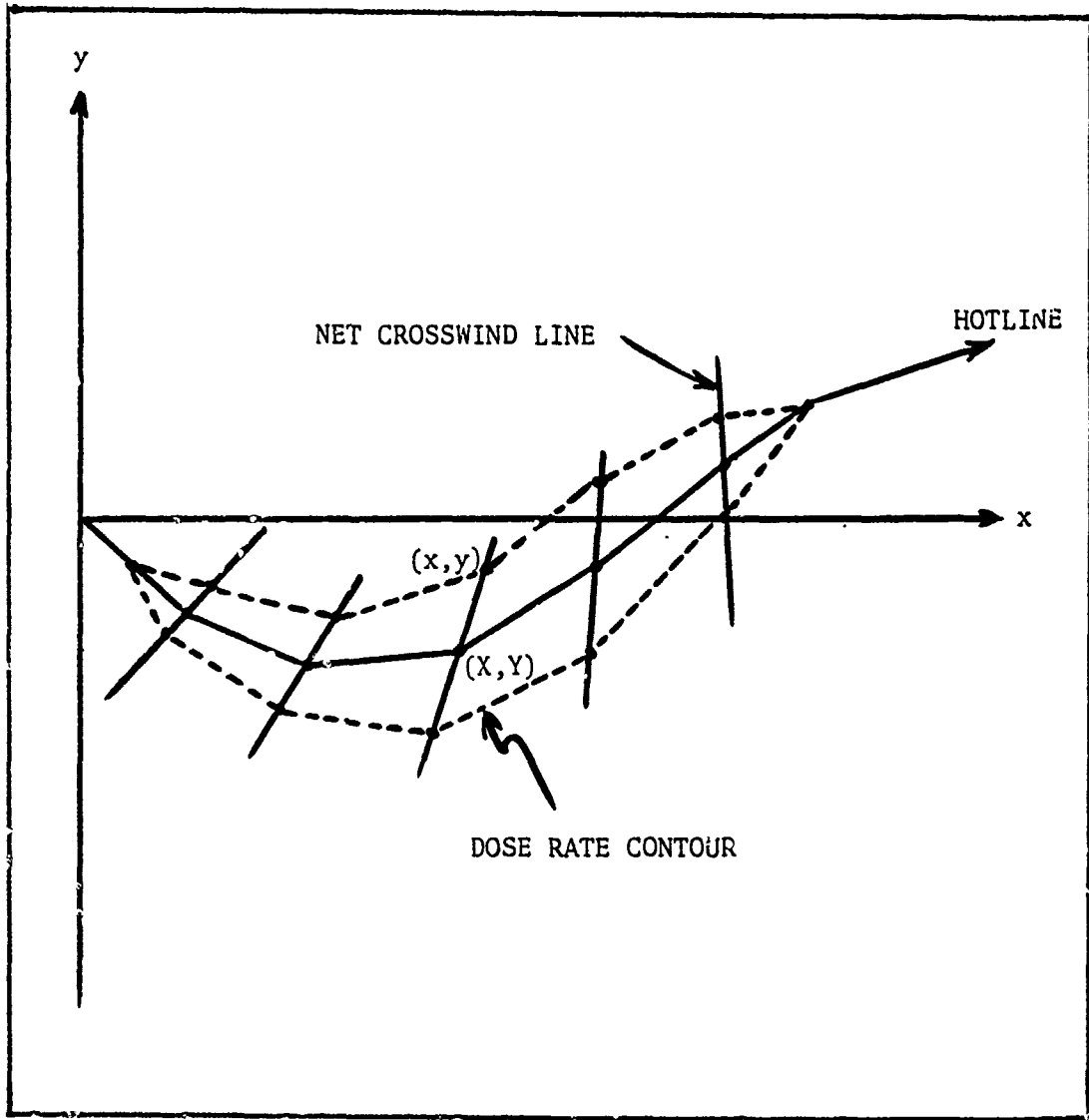
Figure IV-7. Dose Rate Contour Geometry
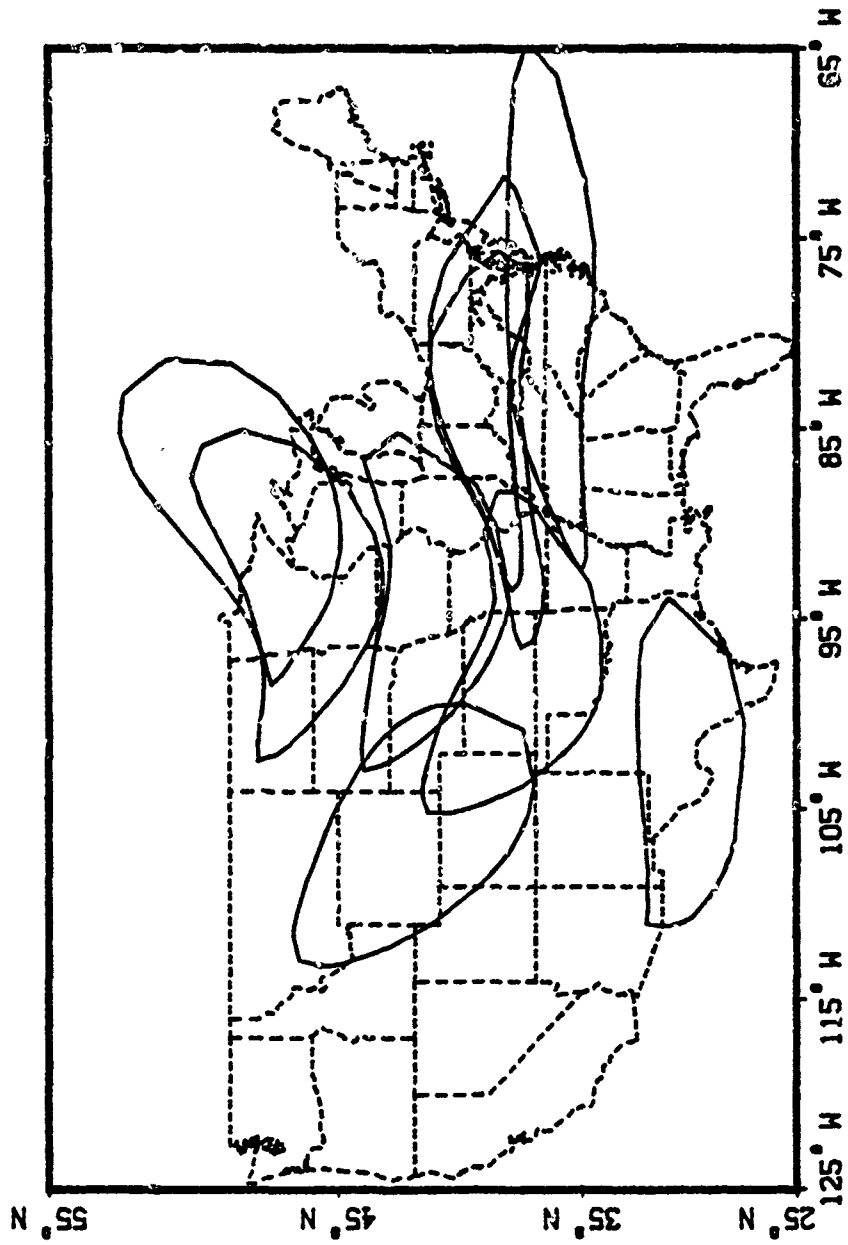
Figure IV-8. Dose Rate Contours

54
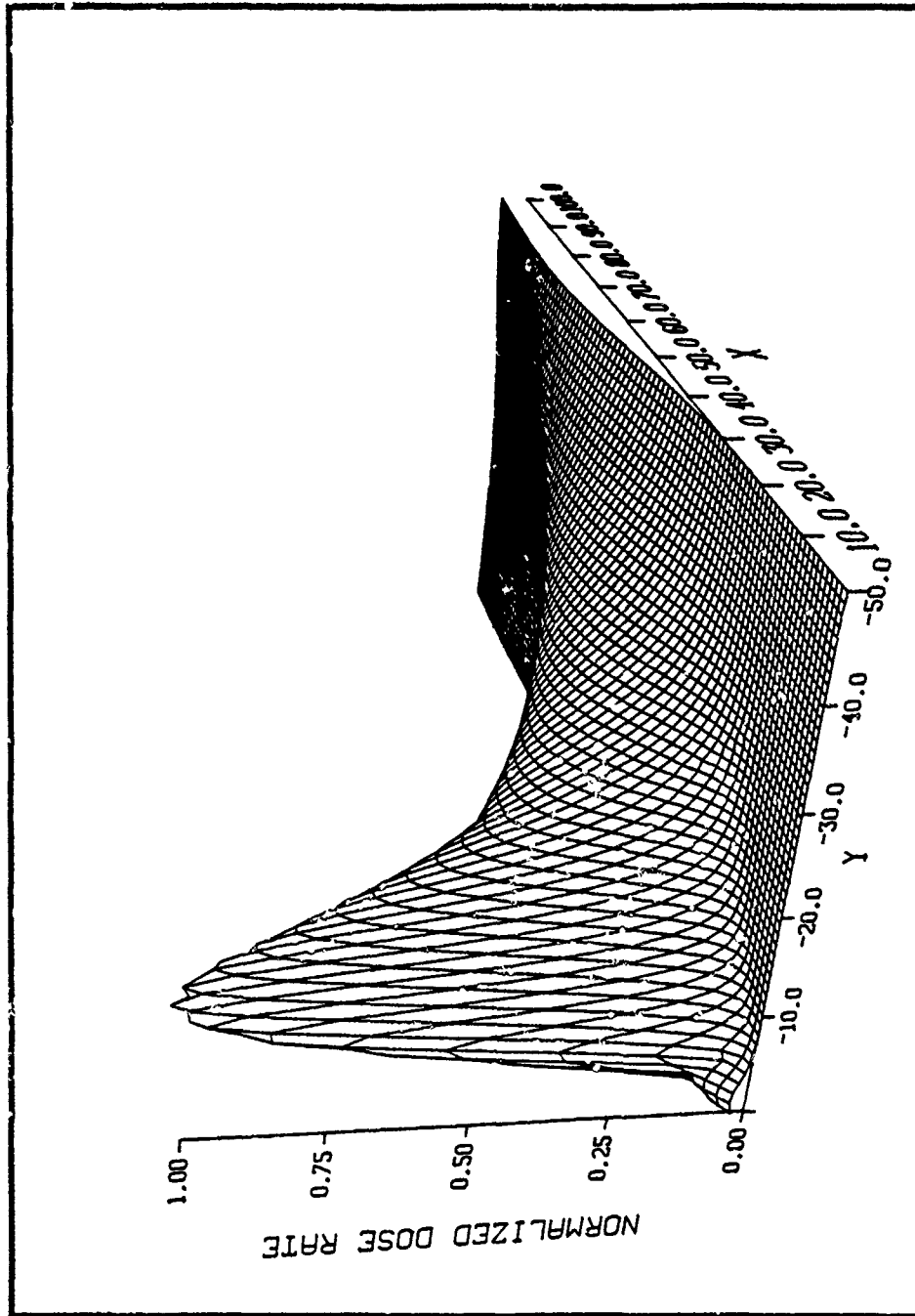
Figure IV-9. Three Dimensional Dose Rate Surface

Summary

A method has been developed to compute fallout dose rate contours around curved hotlines produced by variable winds. The method uses an analytic solution to the dose rate integral Eq (1.1), and hotline coordinates determined with spectral winds (Chapter III). Activity is smeared simultaneously along net crosswind lines as the cloud moves downwind. Dose rate at any arbitrary ground location can be determined, using the technique derived in Appendix F.

V. Validation

Ideally, the new fallout prediction method should be validated by computing fallout dose rate contours for atmospheric nuclear tests, and comparing calculations to actual data and to other model predictions (46)(47)(81). This method requires NMC spectral coefficients to compute the wind vectors that transport falling particles. However, the NMC did not generate and archive the coefficients before 1980. Since the United States conducted atmospheric nuclear testing before 1964, spectral coefficients were not available to validate the fallout transport method with nuclear cloud data.

The NMC Spectral Model was operational when the Mount St. Helens volcano erupted in 1980. Using global wind data for 18, 19, 20 May 80, (116) the NMC generated and provided spectral coefficients to support validation of the new transport method with ash cloud data.

Ash cloud data for the 18 May 80 eruption is extensive; radar observations, fallout collectors, sampling aircraft and satellites provided correlative information for fallout studies. This chapter describes the Mount St. Helens cloud, the transport and deposition data, and calculations of the ashfall hotline location and isomass contours using spectral winds. The excellent agreement between observed and calculated hotline locations and ashfall arrival times confirms that spectral winds can accurately determine trajectories of particles falling from a high yield (megaton-range) cloud.

Further validation is presented for a low yield (kiloton range) cloud. The Defense Nuclear Agency (DNA) detonated 600 tons of high explosives in

New Mexico on 26 October 83. The test explosion, codenamed DIRECT COURSE, created a cloud that rose approximately 3 kilometers above ground, and moved to the northwest. Using spectral coefficients, again supplied by the NMC, the cloud trajectory was computed and compared to observations. Excellent agreement between calculated and observed trajectories confirms that spectral winds can accurately simulate the motion of low yield clouds in the atmosphere.

Following are the Mount St. Helens and DIRECT COURSE cloud analyses. Both cloud studies show that spectral wind transport is a feasible, accurate method for improving fallout modeling with variable winds. The Mount St. Helens analysis was extended to show how the smearing model can be adapted to compute volcanic ashfall and to back-calculate the cloud particle size distribution from ashfall data.

Mount St. Helens Ash Cloud Analysis

Cloud Rise, Transport and Deposition. The eruption of 18 May 80 produced the largest ash cloud of the six major eruptions in 1980 (61). Initiated by a Richter 5.1 earthquake at 0832 Pacific Daylight Time (PDT), Mount St. Helens erupted into a Plinian column of volcanic gases and particles that rose to more than 22 kilometers above ground in approximately 10 minutes (44). Subsequently, the top part of the ash column expanded into a mushroom-shaped cloud that elongated and moved downwind as ash particles fell. The volcano erupted continuously for more than 9 hours.

The ash cloud stabilized at different heights during the nine hour eruption time. Table V-1 shows the approximate altitudes of visible cloud top, bottom and center near stabilization time (90). Time-varying

TABLE V-1

Stabilized Cloud Heights at 0845 PDT   (90)

Top	17.1 kilometers
Center	12.1
Bottom	7.1

TABLE V-2

Radar-Detected Cloud Top Heights   (44)

Time (PDT)	Height
0915 - 0938	12.0 kilometers
0938 - 1100	12.5
1100 - 1158	14.0
1158 - 1255	13.0
1255 - 1330	12.9
1330 - 1500	13.0
1500 - 1605	13.5
1605 - 1705	15.5

radar observations of cloud top heights are shown in Table V-2. While a visible cloud dimension cannot be related quantitatively to a cloud dimension, the radar-detected cloud top is close to the visible cloud center height. The time-weighted average of radar cloud top heights is 13.3 kilometers above ground level (AGL), ranging from 12.0 to 15.5 kilometers during the eruption.

Satellite data shows that the ash cloud front travelled 500 kilometers in less than 5 hours. Figure V-1 (used here with permission) shows the time-varying position of the satellite-detected cloud's leading edge; the satellite-detected cloud was transported by a high-velocity wind layer centered at approximately 12 kilometers above sea level, ASL. The volcano's mouth was approximately 2.9 kilometers ASL. Figure V-2 shows the initial arrival times of fallout on the ground, along the downwind line of maximum ashfall (the hotline); hotline position was estimated from isomass contours in (90). Cloud transport and deposition are summarized in Figure V-3 (again, used with permission). Ground ashfall generally occurred to the north of the satellite-detected cloud, because wind direction generally veered with increasing height.

Figure V-4 shows the elapsed time of eruption, and times for which the NMC provided spectral coefficients. Most of the 9 hour eruption time was within 6 hours of 00UT 19 May 80, so cloud transport and fallout trajectories were most accurately replicated with persistent winds for that time. Time-varying winds were produced by interpolating spectral winds for different times.

Spectral Winds. The NMC provided 5 sets of spectral coefficients, representing winds from 00UT 18 May 80 through 00UT 20 May 80, at 12 hour

60
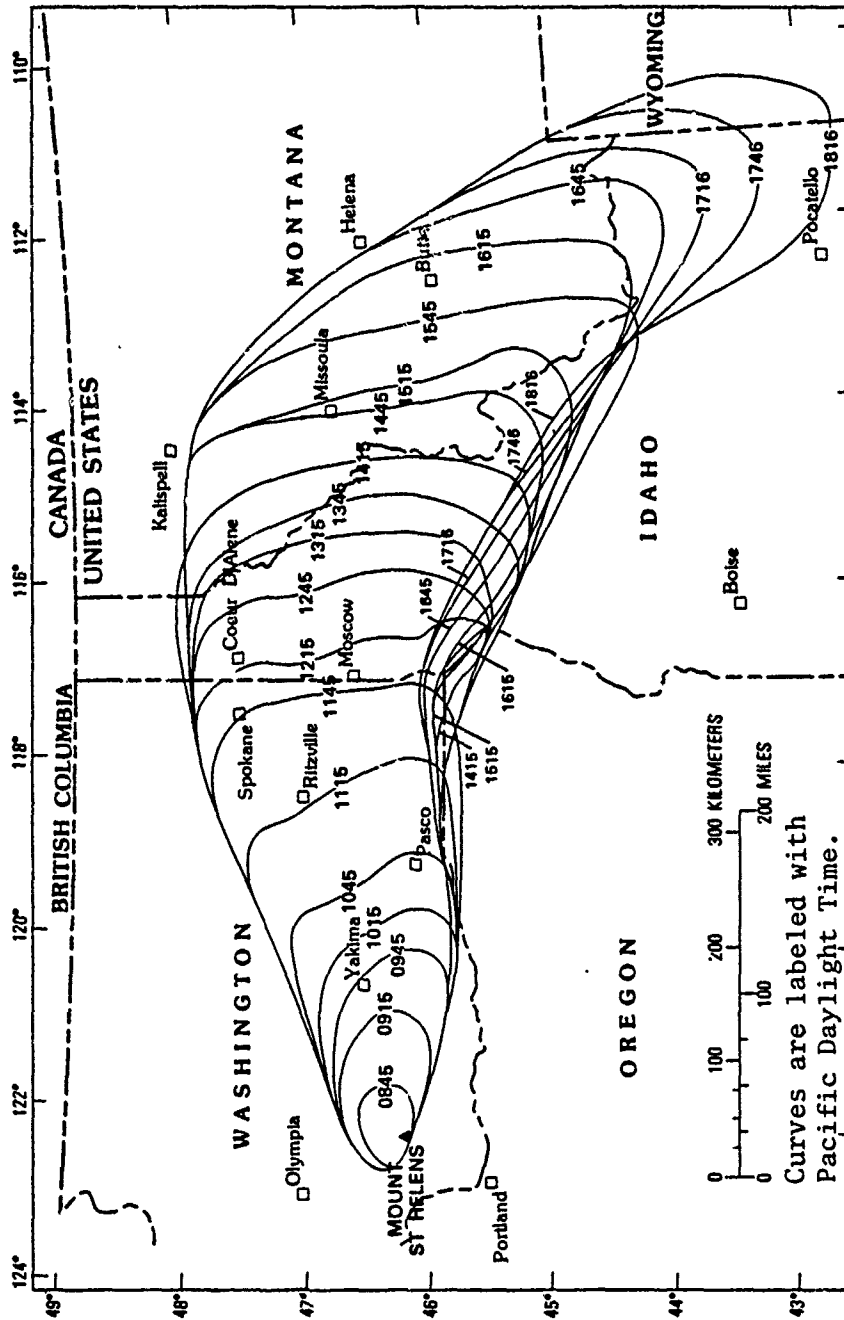
Figure V-1. Satellite-Detected Cloud Outlines (90:579)
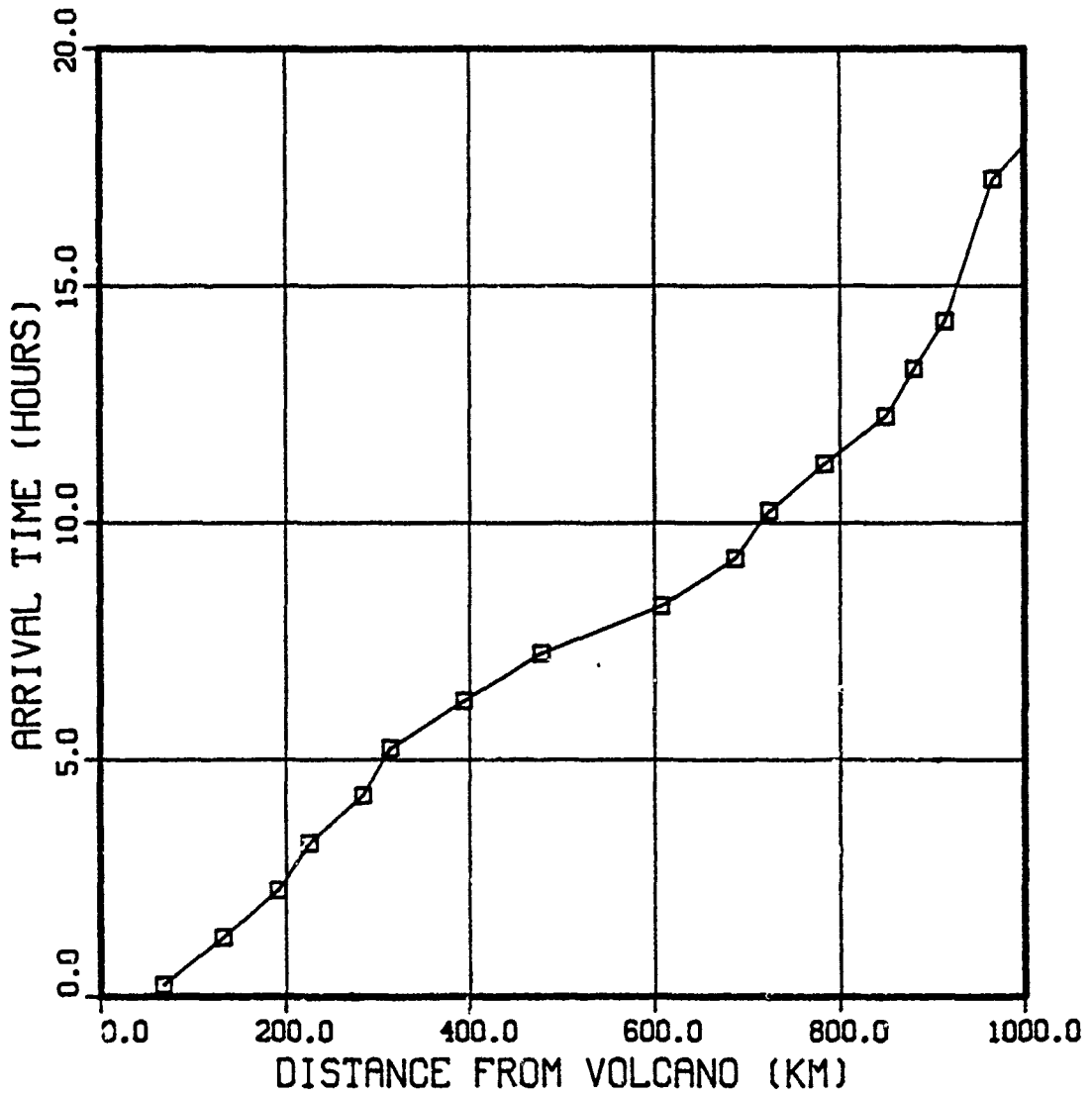
Figure V-2. Arrival Time vs Downwind Distance
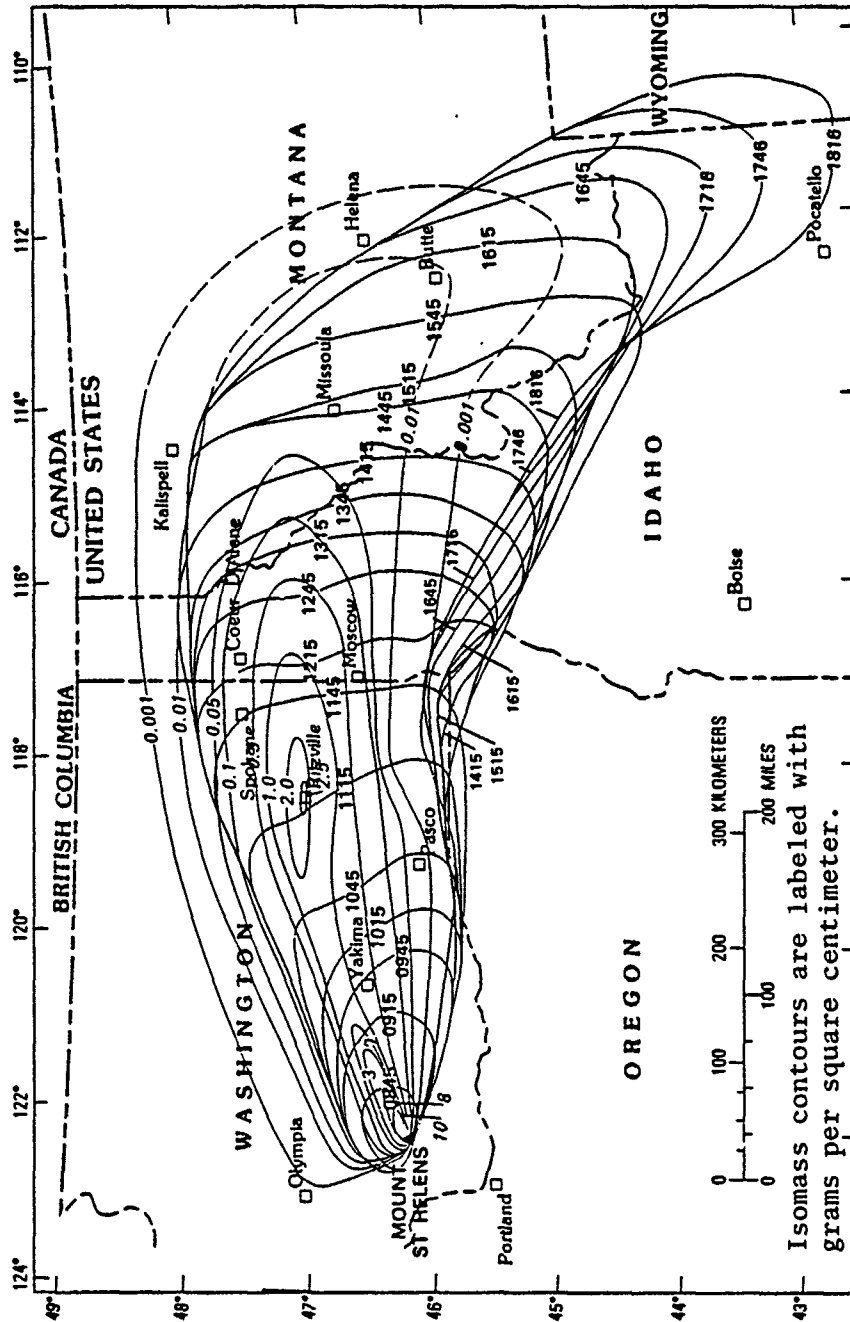
Figure V-3. Isomass Contours and Satellite Cloud Outlines (90:588)
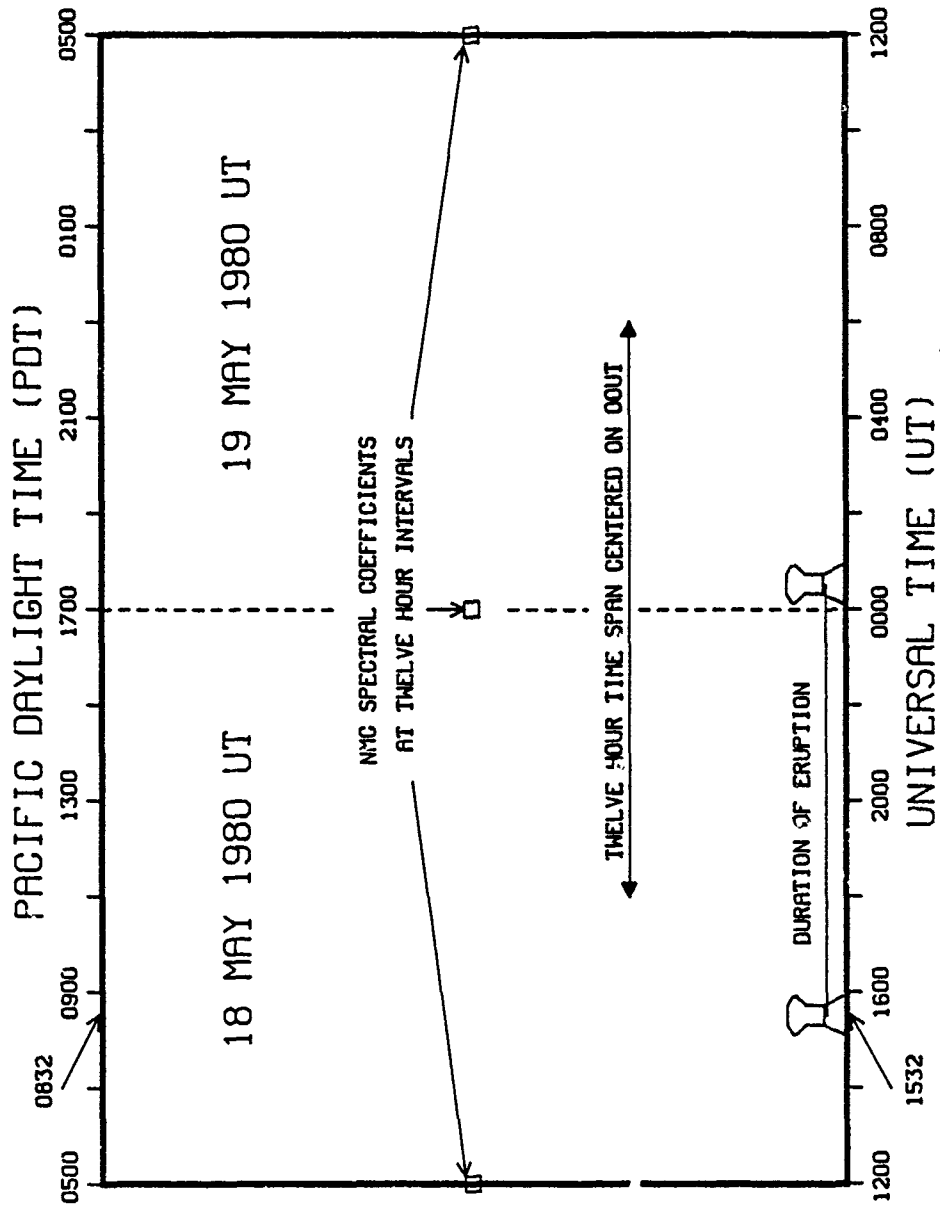
Figure V-4. Time Line of Eruption and Wind Coefficients

64

intervals. The coefficients were written on magnetic tape, formatted in 80 column card images (113). One set contains 992 complex pairs for each of two wind vector components at each of 12 levels. There are 23808 complex pairs in each set of coefficients.

Figures V-5 through V-7 show wind vectors computed with the 00UT 19 May 80 coefficients on a $2\frac{1}{2}$ degree latitude/longitude grid over continental United States. The three levels were chosen to illustrate low, middle and high altitude winds in the atmosphere. High altitude tropospheric winds are typically faster than low altitude winds and the flow is generally westerly. Wind vector length is the distance travelled by a parcel of air in 3 hours. The effect of the jet stream is most evident in the 250 millibar wind field, Figure V-6.

Hotline and Isobaric Trajectories. Spectral coefficients were used to compute the ashfall hotline location and isobaric trajectories at ten heights above the volcano. An isobaric trajectory is the path travelled by an air parcel at a fixed height or pressure level. In 1980, isobaric trajectory predictions were used by the United States Geological Survey to forecast ashfall hazards before the volcanic eruption (73)(99).

The hotline locator starts with an initial, stabilized cloud and computes the trajectories of spherical particles falling through variable spectral winds to the ground. The connection of particle landing points on the ground is the hotline. The initial cloud model has a gravity-sorted distribution of particle size vs height, described in Chapter III. The size-height equation was derived from nuclear cloud calculations, so it is weapon yield dependent. In this application, yield is just a parameter for cloud height selection. A range of yields

65
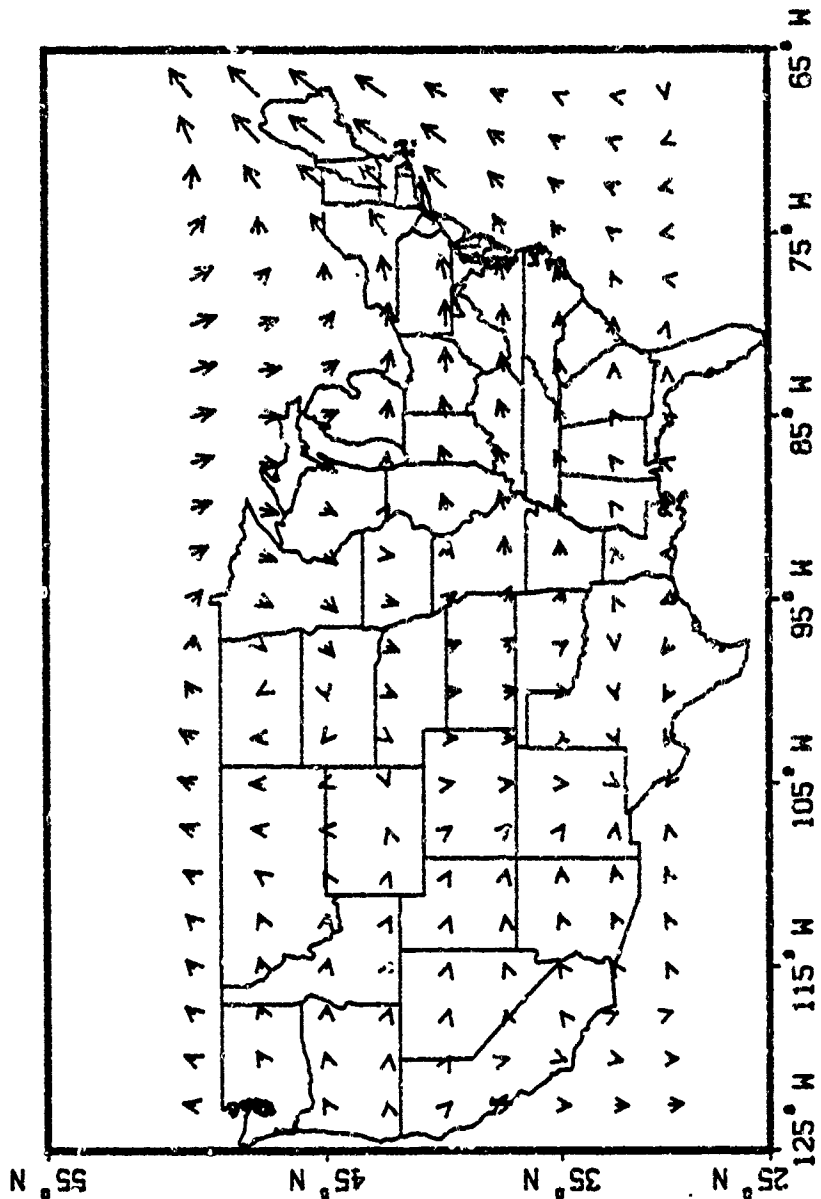
Figure V-5. 00UT 19 May 80 Wind Field (850 mb)

66
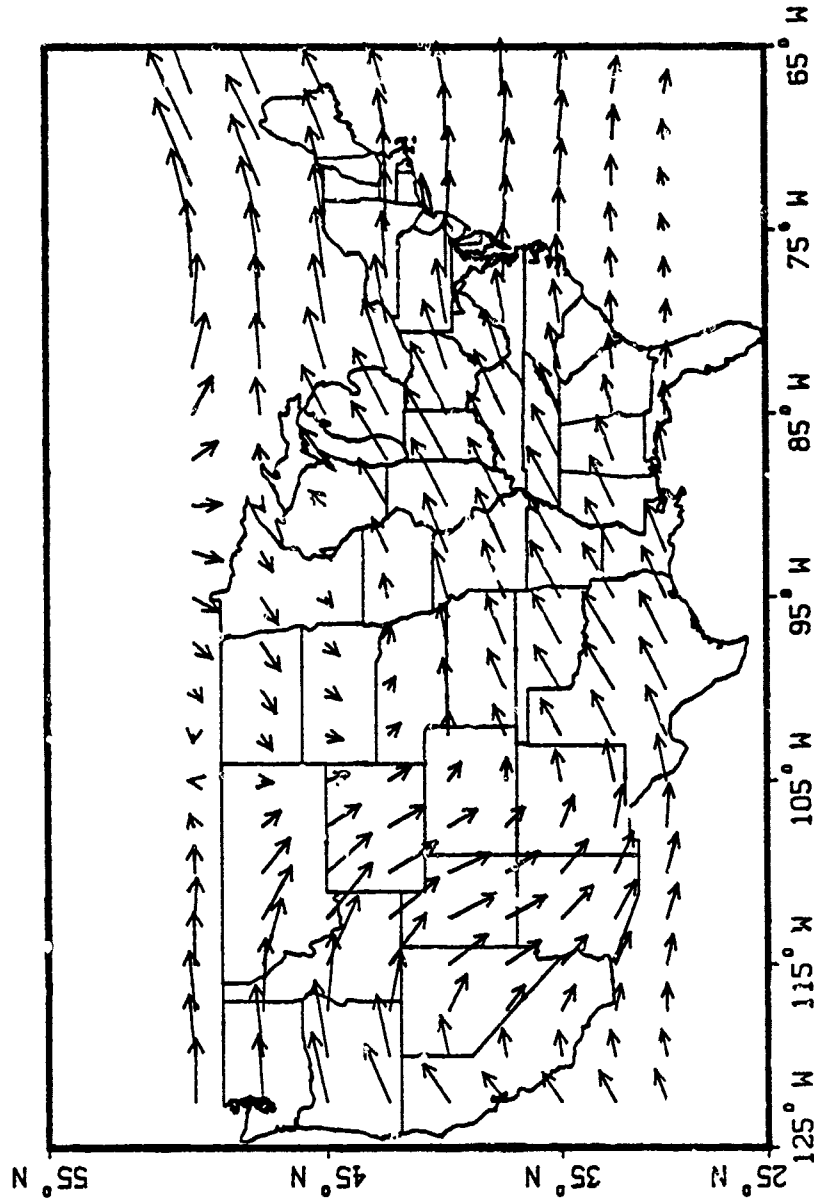
Figure V-6. 00UT 19 May 80 Wind Field (250 mb)

67
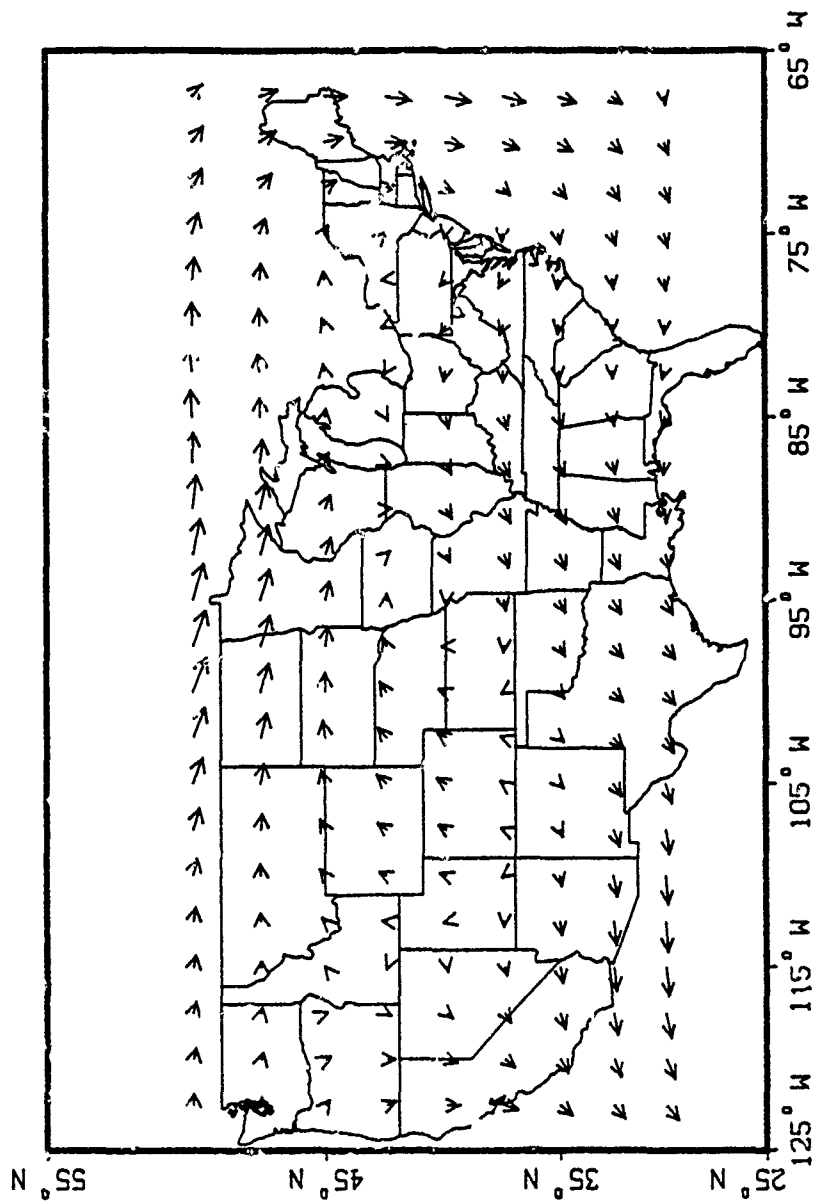
Figure V-7. 00UT 19 May 80 Wind Field (50 mb)

68

was examined to find a yield that positioned the initial cloud within the altitude bounds detected visually and with radar, matching the observed hotline location. Figure V-8 shows how the computed hotline location varied with different choices of the yield parameter in the 00UT 19 May 80 winds. The hotline from a 0.5 megaton initial cloud closely matched the actual hotline, although all three of the predicted hotlines in Figure V-8 have generally correct position and curvature. The 0.5 megaton yield is not an estimate of eruption energy; yield is a parameter used to position the initial cloud. Total eruption energy has been estimated to be much higher, approximately 24 megatons (61:563).

Furthermore, computed arrival times of volcanic ash particles agreed with the observed ashfall onset times (38). Figure V-9 shows observed and calculated arrival times on the hotline out to 1000 kilometers from the volcano. Arrival time is an excellent indicator of the suitability of spectral winds for fallout calculations, because arrival time incorporates all wind vectors computed along each particle's trajectory. Also, arrival times are computed during hotline location (Chapter III), and used to define the net wind vectors in the variable wind smearing model (Chapter IV). The root-mean-square (rms) difference between observed and computed net wind speeds is 2.1 meters per second. Figure V-9 also shows the arrival times computed with the same initial cloud, using a constant vertical wind profile for transport calculations. The constant vertical wind profile is a combination of linear regression fits to wind measurements at Salem, Oregon, at 3 different times (21). The constant wind profile generally overpredicts arrival times; the rms difference between observed and computed net wind speeds is 4.3 meters
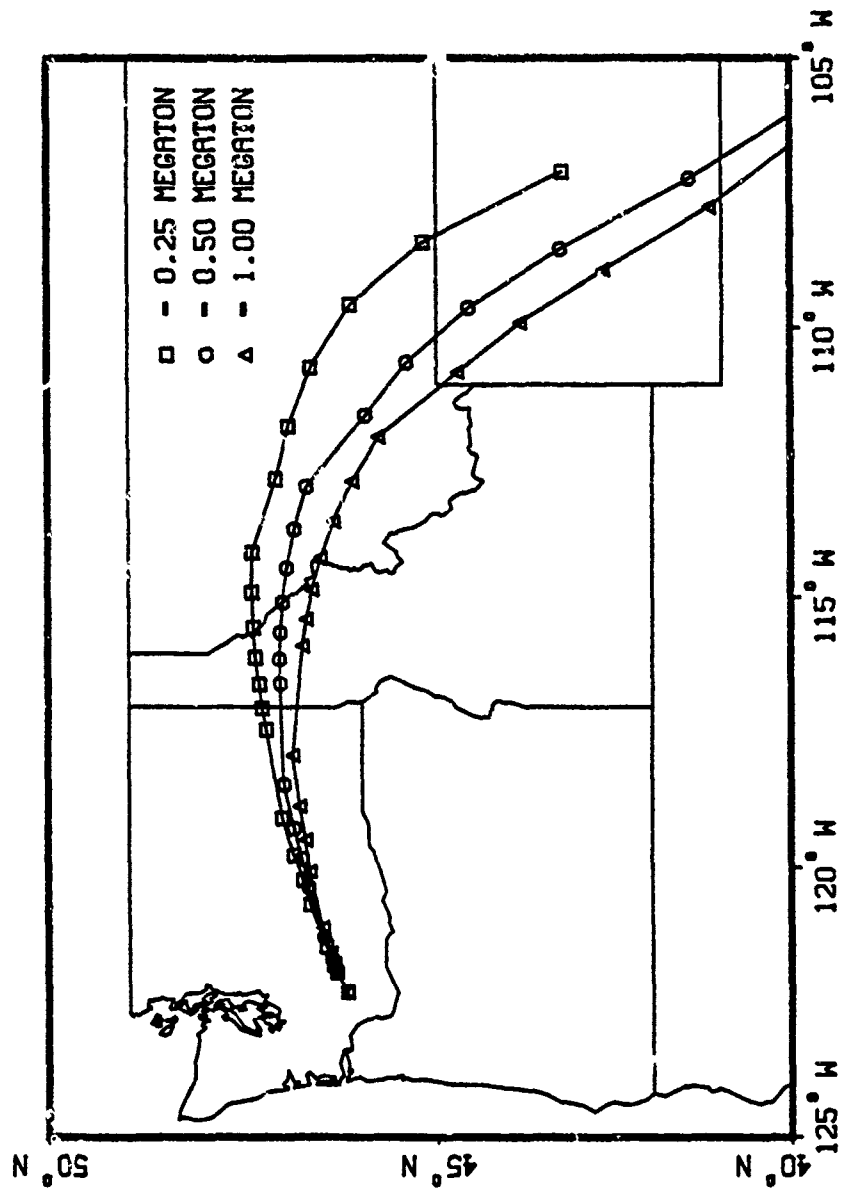
Figure V-8. Hotlines: Yield Variations
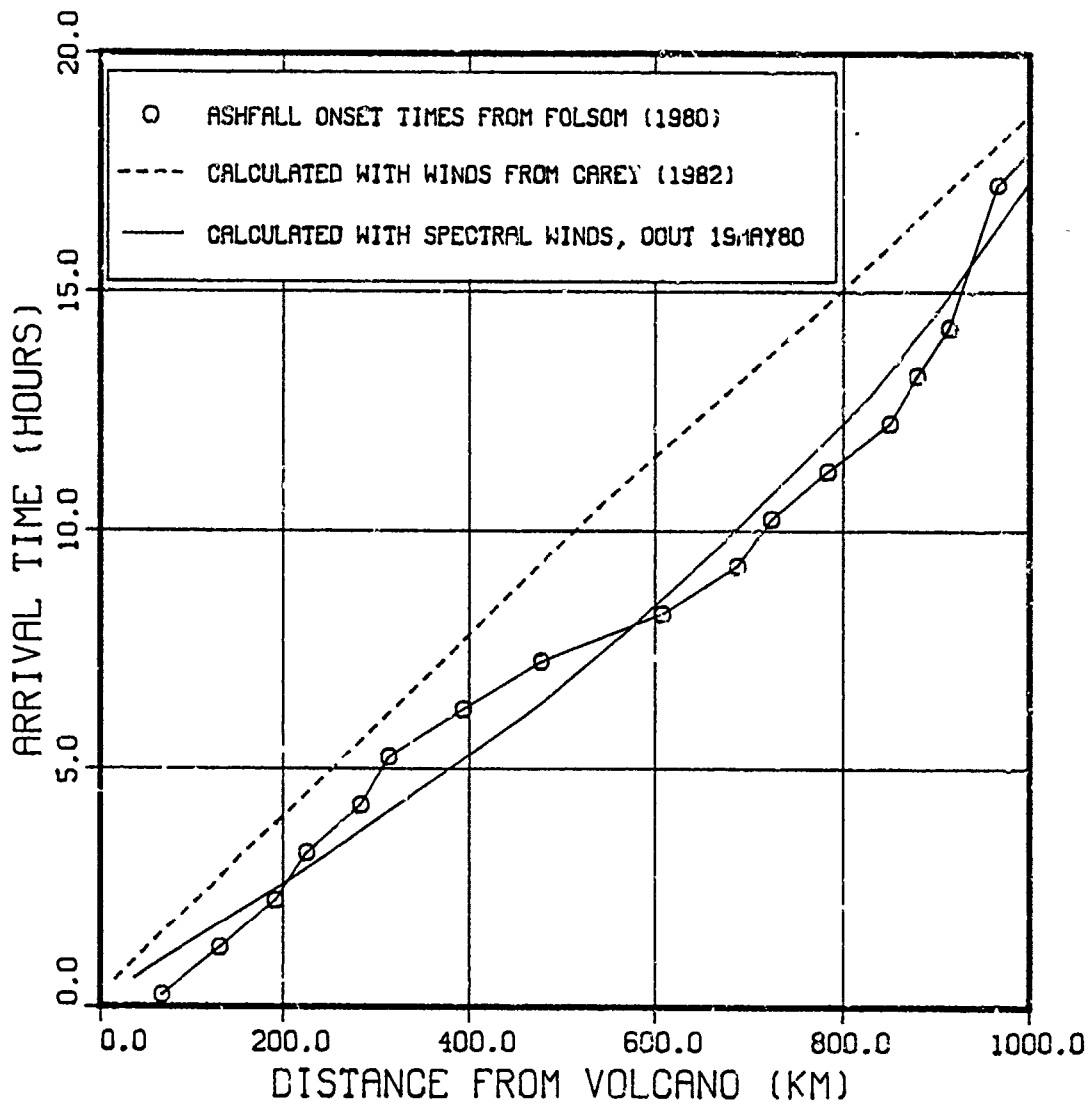
Figure V-9. Arrival Time Data and Calculations

71

per second. The spectral wind field produced net wind vectors that were twice as accurate as the net wind vectors computed with a constant vertical profile.

With spectral winds for different times, the predicted hotlines diverged significantly. Figure V-10 shows hotlines predicted with spectral coefficients for four different times. All preceeding calculations were done with one set of spectral coefficients; winds were spatially, not temporally, interpolated. The same three dimensional wind field persisted during cloud transport. As expected, the 00UT 19 May 80 winds most accurately replicated the observed hotline.

Temporal variations were modeled by interpolating spectral coefficients or wind vectors for adjacent times as particles fell from the initial cloud. Knowing when a particle starts to fall, the temporally adjacent coefficient sets can be identified and interpolated to compute winds at any time during particle fall. Figure V-11 shows hotlines computed with temporally varying spectral winds, using three different starting times: 0845, 1145 and 1445 PDT. The three curves on Figure V-11 show how temporal changes in trajectory winds affected hotline placement. Within 300 kilometers of the volcano, temporal wind variations during the eruption did not significantly affect ashfall location. However, at longer ranges and longer travel times, the effects of temporal wind changes are apparent. Ash that erupted in the first six hours curved southward sooner than ash that erupted later, causing the ashfall to be smeared over wider areas at long distances. Temporally varying winds could be used to predict ash trajectories if the time-varying eruption rate data could be estimated from radar measurements (44)(45).

72
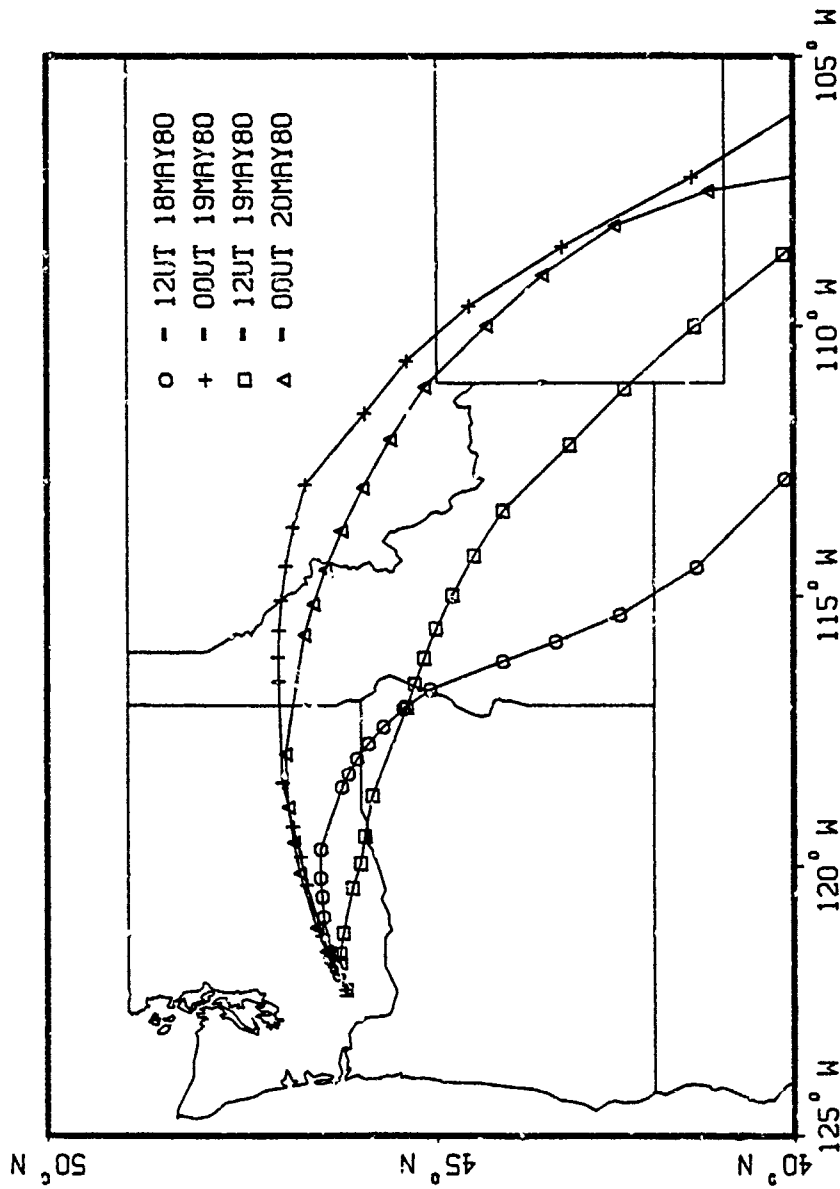
Figure V-10. Hotlines: Four Different Times

73
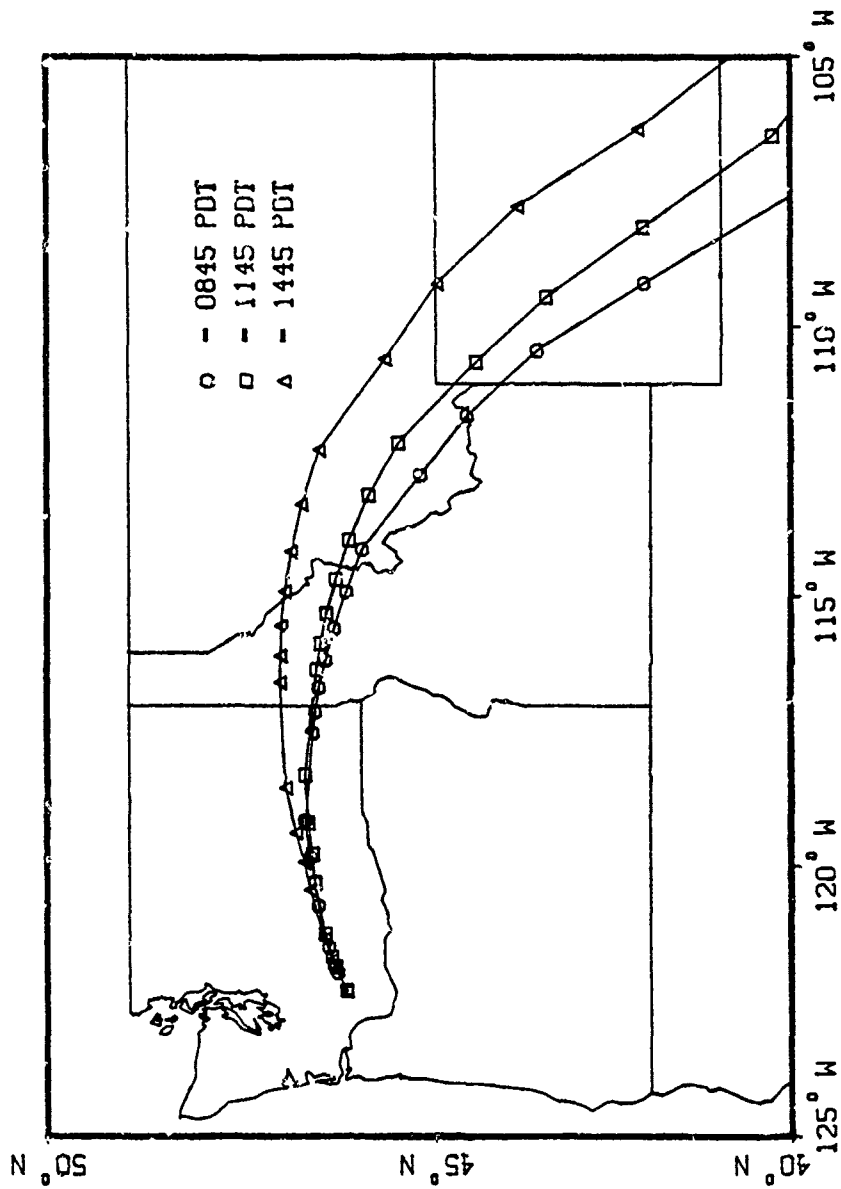
Figure V-11. Hotlines: Three Different Starting Times in Variable Winds

Small volcanic ash particles, $\lesssim 1$ micrometer in diameter remained suspended in the atmosphere for a long time. Aircraft measurements showed that Mount St. Helens ash actually circled the earth in about 16 days (21). Long range transport was computed with temporally varying spectral winds in constant-altitude trajectories. In this report, constant-altitude trajectories are also isobaric, because the U.S. Standard Atmosphere was used for all atmosphere state parameter calculations. Isobaric trajectories simulate the transport of particles with negligible fall speeds. Figures V-12 and V-13 show isobaric trajectories near the volcano and over a continental scale, computed with temporally interpolated spectral winds, starting at 0845 on 18 May 80. Two general paths are evident: (1) the upper tropospheric winds moved particles southeastward over Wyoming and Kansas before turning to the northeast; (2) the low level winds carried ash northeastward into Canada. The National Oceanic and Atmospheric Administration (NOAA) predicted isobaric ash trajectories using measured and forecasted wind data (26)(101). The NOAA predictions are shown in Figure V-14. The same two general paths are also evident in the NOAA predictions.

Ash Fallout Model. The dose rate equation, Eq (4.1), was modified to compute mass of volcanic ash per unit area on the ground. Three changes were necessary to derive an ashfall equation.

First, the source normalization constant, k, weapon yield, Y, and fission fraction, ff, were replaced by the mass lofted into the volcanic cloud. Mass of downwind ash was approximately 5×10^{14} grams (44)(90). Estimates of total mass assumed rock mass densities of 2.0 to 2.8 grams per cubic centimeter, representative of the solid, unfractured rock on

75
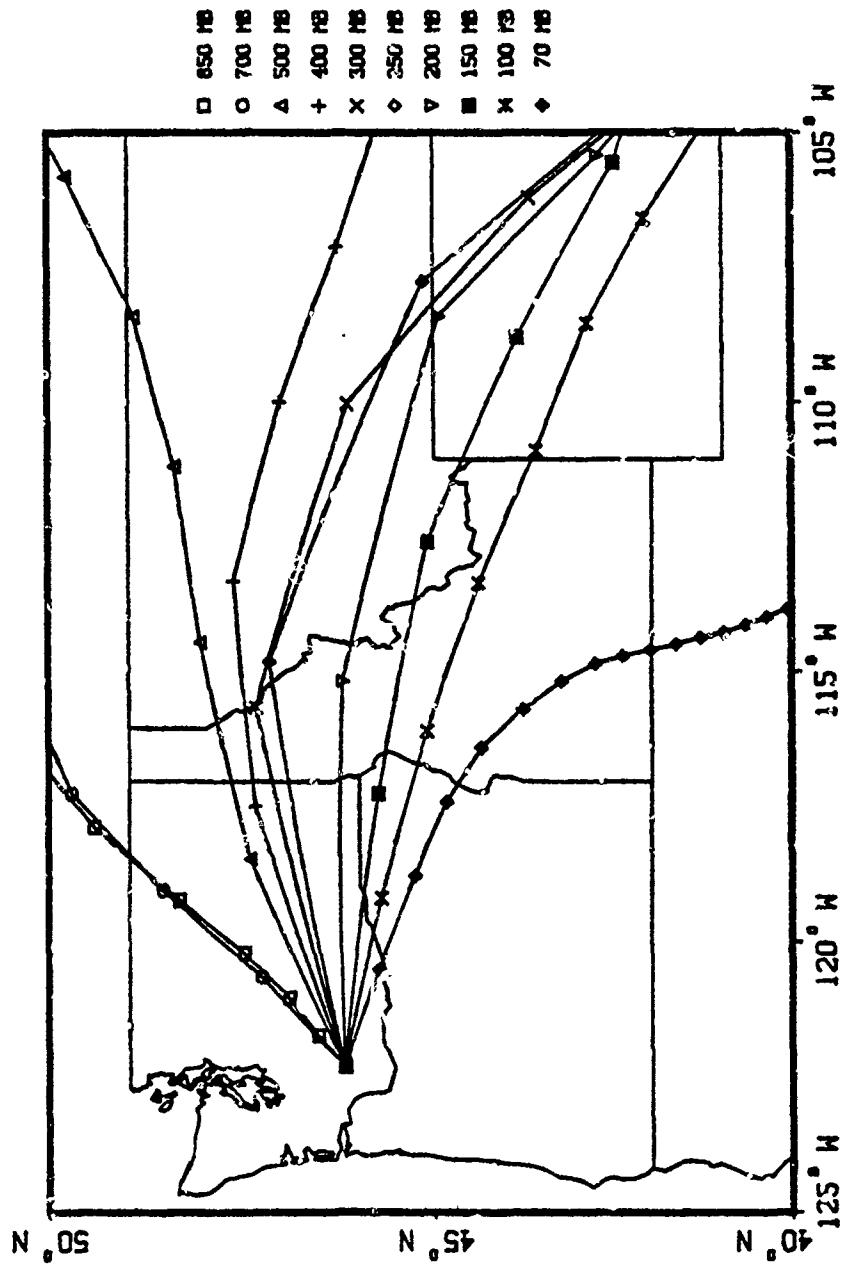
Figure V-12. Isobaric Trajectories with Temporally Varying Winds
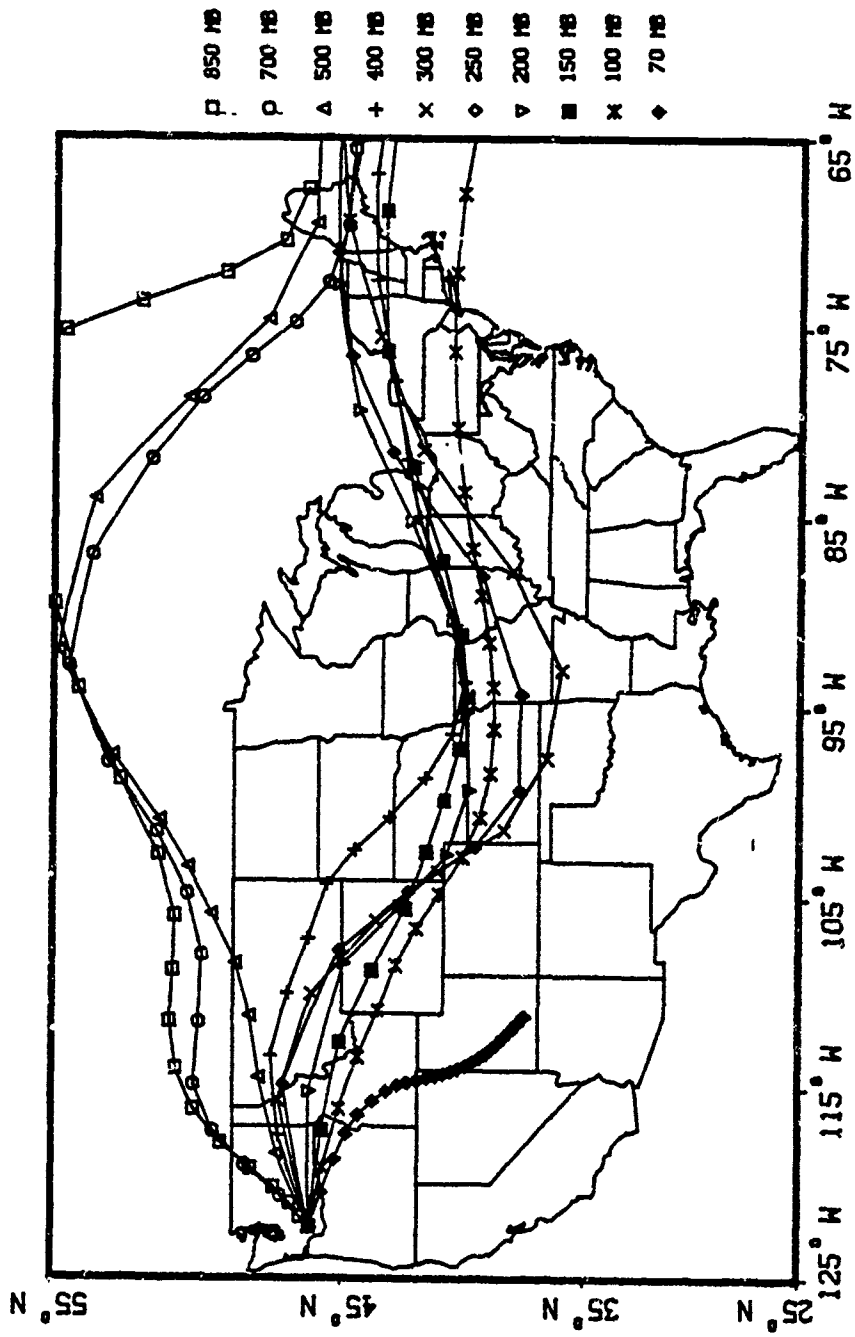
Figure V-13. Isobaric Trajectories with Temporally Varying Winds

77
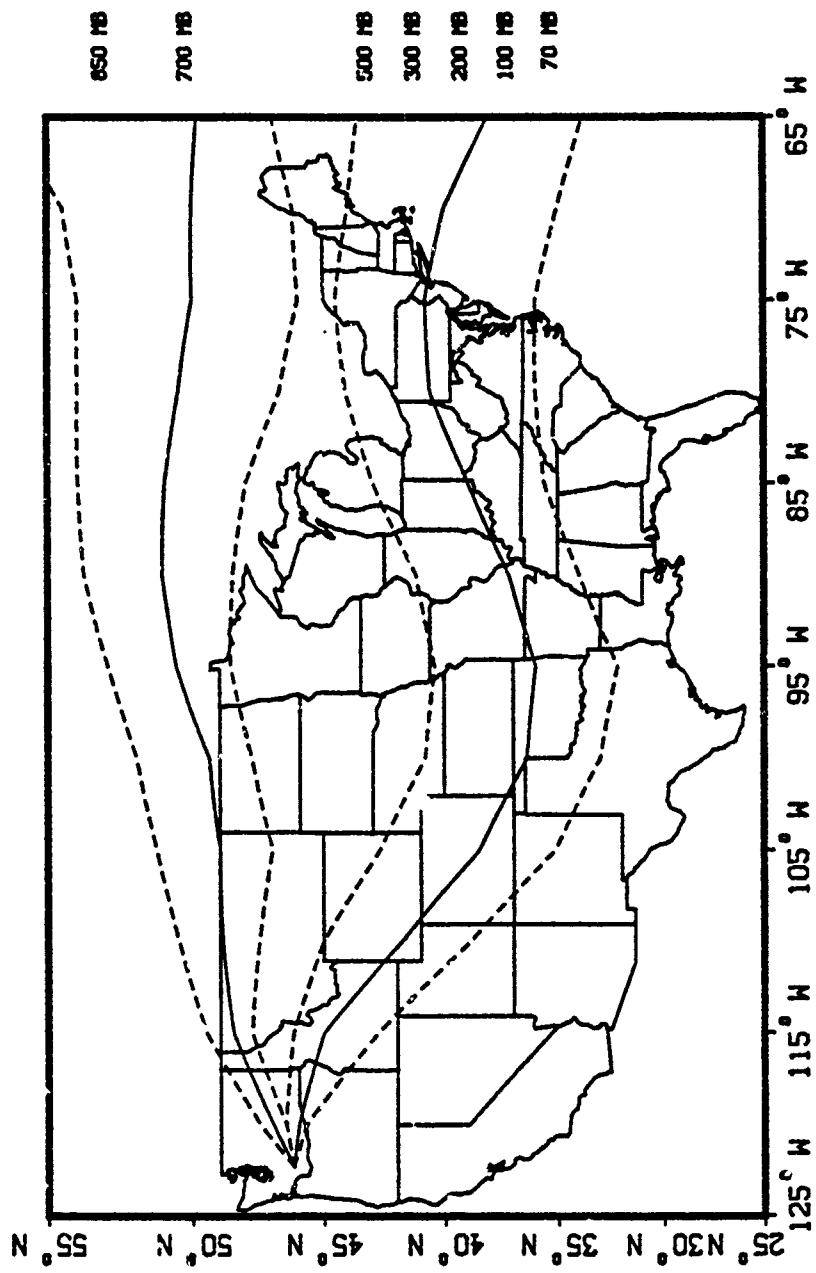
Figure V-14. NOAA Isobaric Trajectories

650 MB
700 MB
500 MB
300 MB
200 MB
100 MB
70 MB

the mountain (39). However, measurements of ash particles' mass density showed many particles with density less than 2.0 grams per cubic centimeter (21). Cloud particles can have various mass densities, due to different rock types and because the particles can contain air pockets and fissures produced during solidification, collision with other particles and breakage during eruption (118). In this report, 2.0 grams per cubic centimeter was used as a representative value. In fact, hotline location was not particularly sensitive to density variation; see Figure V-15.

Second, the fractionated activity-size frequency distribution, $A(r)$, was replaced by a particle mass-size distribution function for the ash cloud. A cloud distribution was measured by Carey and Sigurdsson (21) using fallout samples; a cumulative form of their histogram is shown in Figure V-16, with the DELFIC default mass-size spectrum for reference. The measured distribution suggests that the Mount St. Helens ash cloud size distribution was multimodal. A multimodal size distribution is consistent with qualitative and quantitative analyses of ash fallout (16). Observed ash was a mixture of two distinctly different rock types: old rocks from previous eruptions and new magma (21)(39)(91). The measured particle mass-size frequency histogram was fit with an analytic function using the nine parameter function minimization technique described in Appendix G. Following is a trimodal log-normal function that fits the histogram:

$$M(r) = \sum_{i=1}^{3} \frac{f_i}{\sqrt{2\pi}\ \beta_i\ r}\ \text{EXP}\left(-\tfrac{1}{2}\left(\frac{\ln r - \alpha_i}{\beta_i}\right)^2\right) \qquad (5.1)$$

79
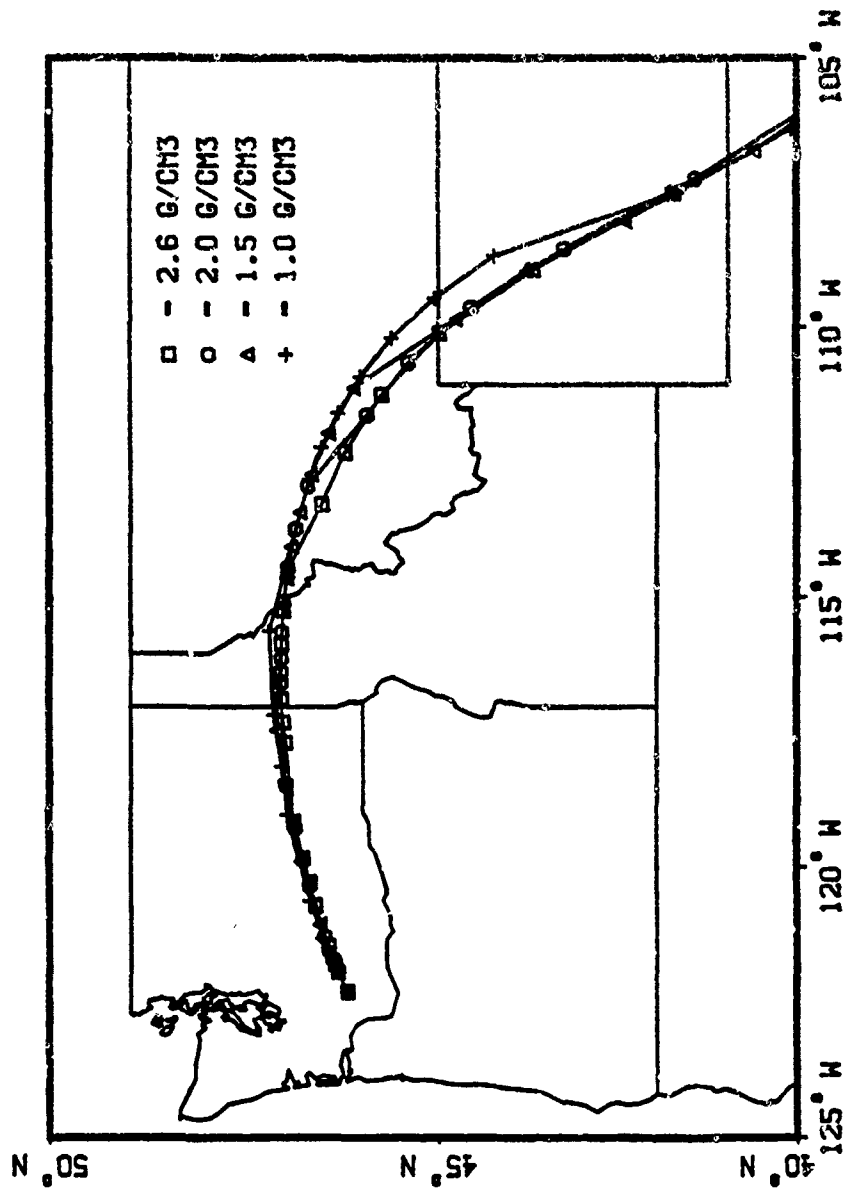
Figure V-15. Hotlines: Particle Density Variations

80
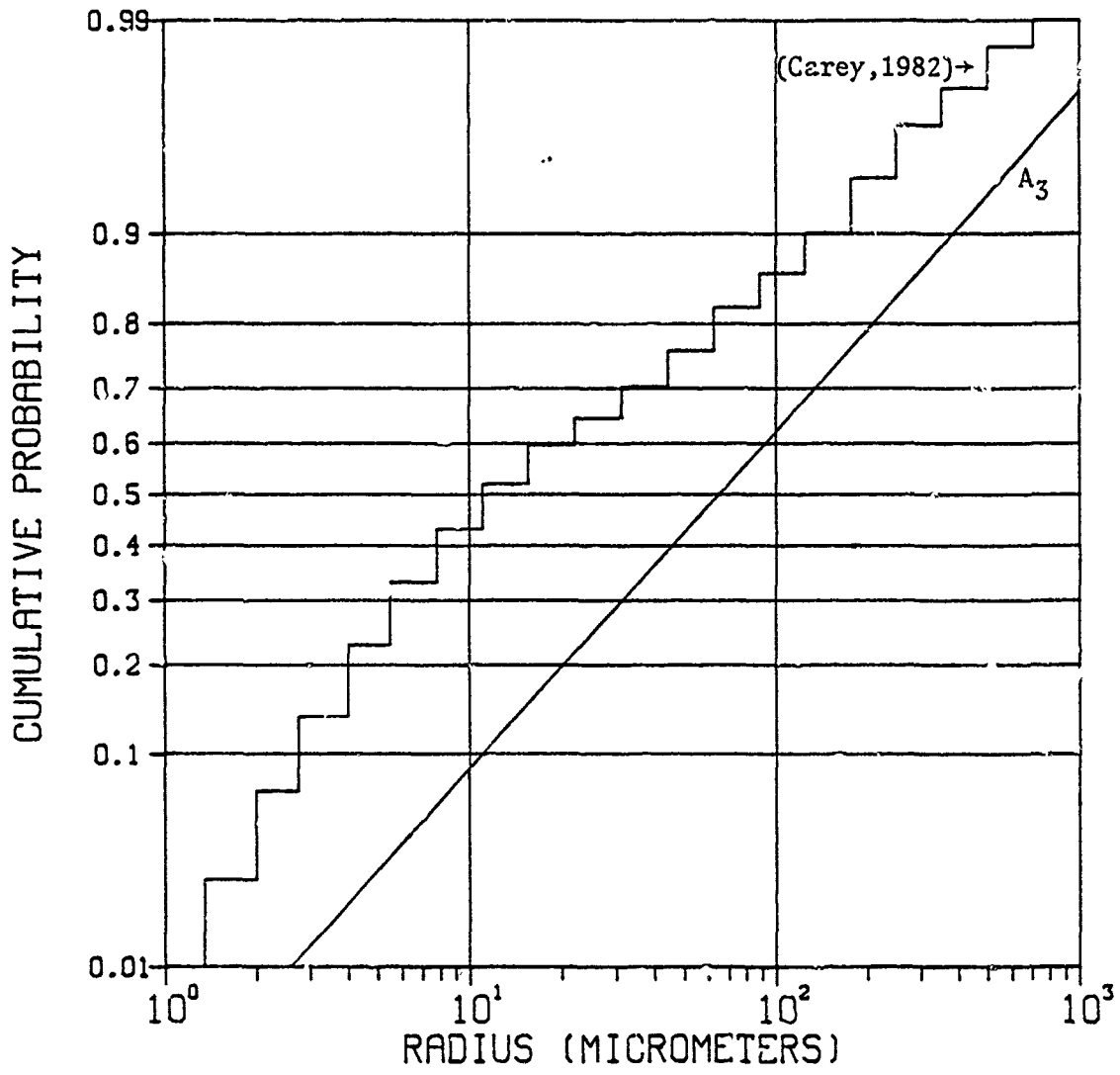
Figure V-16. Measured Histogram and Nuclear Particle Size Distribution

where

$M(r)$ = particle mass-size frequency distribution function
f_i = fraction of $M(r)$ composed of the i-th distribution
β_i = log-slope
α_i = $\ln (r_S^i)$
r_S^i = median particle radius in the i-th distribution

See Table V-3 for numerical values of distribution parameters. Log-normal functions were selected because explosive processes often produce log-normal particle size spectra (2)(40) and because aircraft measurements of the ash cloud showed log-normal distributions (36). Figures V-17 and 18 show the log-normal fit and the ash cloud histogram. Three radius modes occur near 8, 60 and 250 micrometers.

The third change to the dose rate equation necessary to derive an ashfall equation is to replace yield-dependent expressions for lateral deviations with empirical expressions for ash cloud spreading. The satellite-detected ash cloud expanded with time as follows (21):

$$w = 0.006\ t \qquad (5.2)$$

where

w = width of plume front (kilometers)
t = elapsed time since start of eruption (seconds)

Define
$$\sigma = (\sigma_x^2 + \sigma_y^2)^{\frac{1}{2}} \qquad (5.3)$$

and
$$(\sigma_x, \sigma_y) = \frac{(V_x, V_y)}{(V_x^2 + V_y^2)^{\frac{1}{2}}}\ \sigma \qquad (5.4)$$

Assume that
$$w \simeq 4\ \sigma \qquad (5.5)$$

So,
$$\sigma = 0.0015\ t \qquad (5.6)$$

82

TABLE V-3

Trimodal Log-Normal Function Parameters

for the Measured Particle Sizes

i	α_i	β_i	f_i
1	2.031	0.852	0.66
2	4.176	0.633	0.25
3	5.495	0.445	0.09
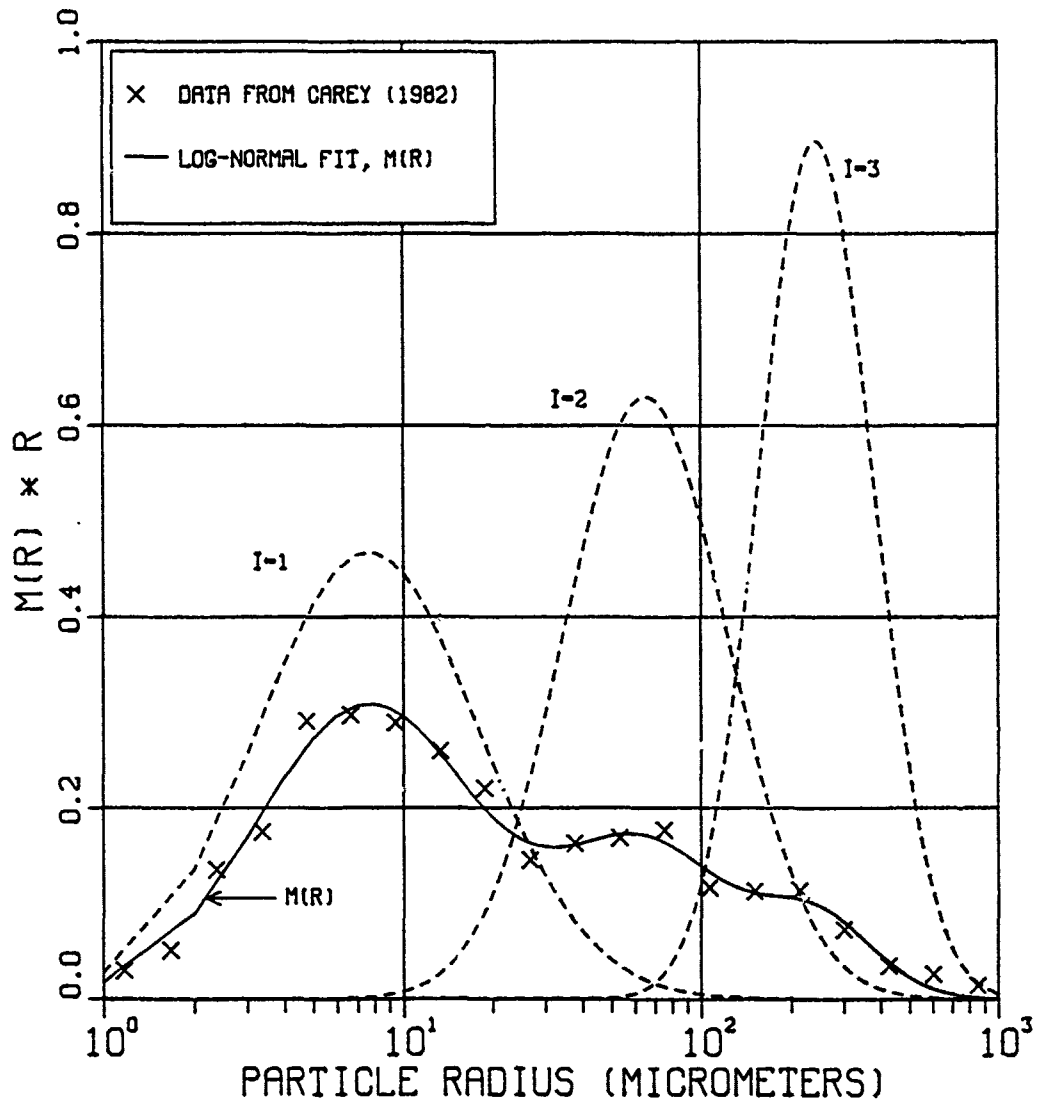
Figure V-17. Fit to Measured Size Distribution
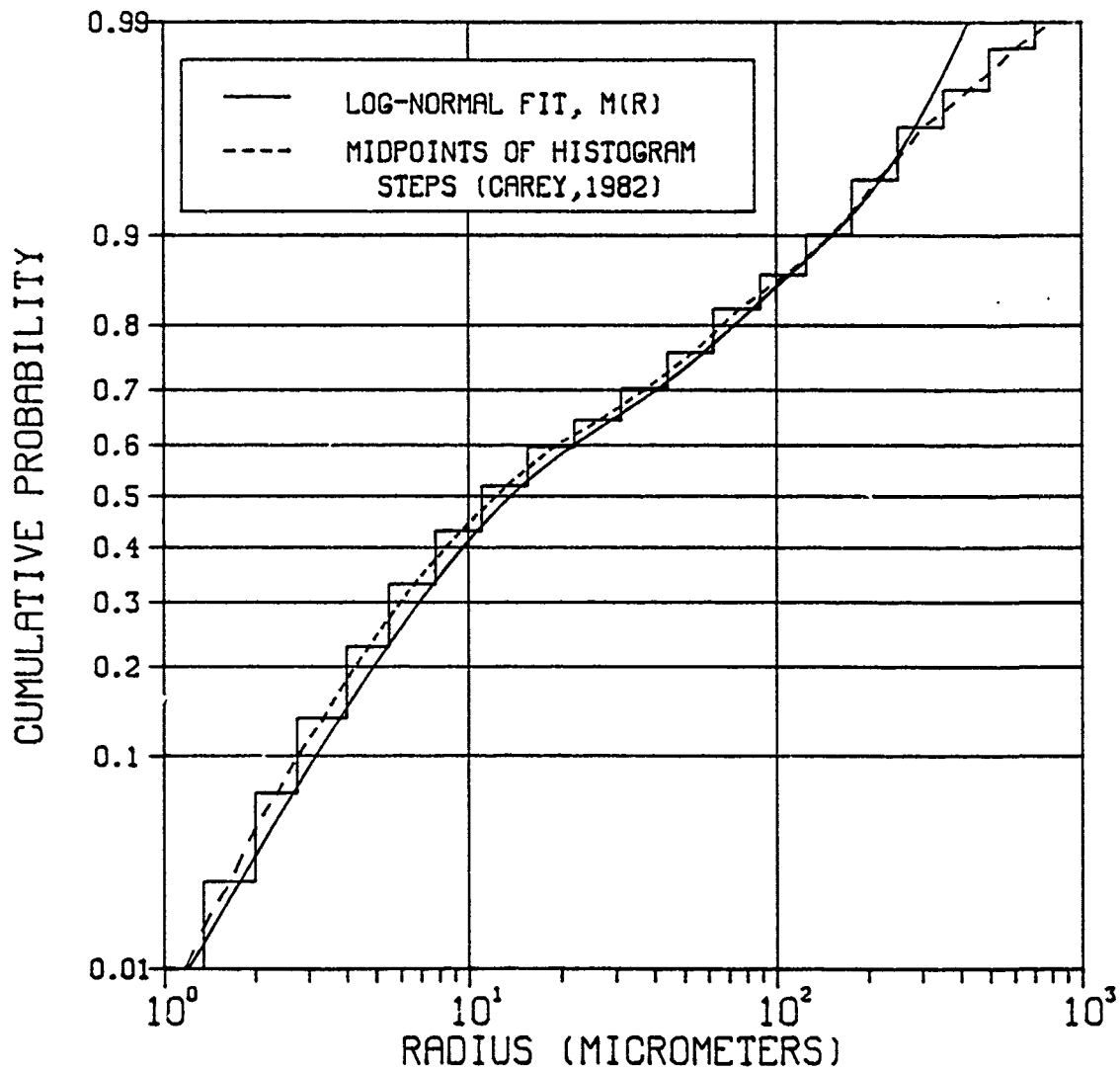
Figure V-18. Fit to Measured Size Distribution (Cumulative)

The preceding three changes convert the dose rate equation into an ashfall equation:

$$A = \frac{T \; M(r) \; |dr/dt|}{\sqrt{2\pi} \; \sigma_V} \; EXP \left[-\tfrac{1}{2} \left(\frac{x \; V_y - y \; V_x}{\sigma_V} \right)^2 \right] \tag{5.7}$$

where

A = ash mass/area on the ground at (x,y)
T = total ash mass lofted into initial cloud during eruption
M(r) = particle mass-size frequency distribution

Figure V-19 shows isomass contours computed with Eq (5.7) using hotline coordinates of Figure V-8. On the hotline, computed mass decreased with increasing distance from the volcano. Figure V-20 shows computed ashfall on the hotline, compared to actual measurements. The fallout data indicates a secondary maximum at approximately 325 kilometers downwind, near Ritzville, Washington. Figure V-3 also shows the "Ritzville Bulge". The Ritzville bulge was not predicted using the measured particle size distribution (Table V-3) in the ashfall equation Eq (5.7).

Particle Sizes in the Falling Cloud. The measured grain size distribution represents the size spectrum of fallen, not falling, particles. The falling cloud particle size spectrum contained aggregates of smaller particles; many of the larger, falling particles were broken during impact and during the mechanical sieving processes used to size the ash samples. Some falling ash clusters were captured and sized without breakage, near Pullman, Washington; data indicates that falling particles were two to five times larger than fallout particle sizes reported for that location (52)(100). The unbroken particle data is consistent with terminal
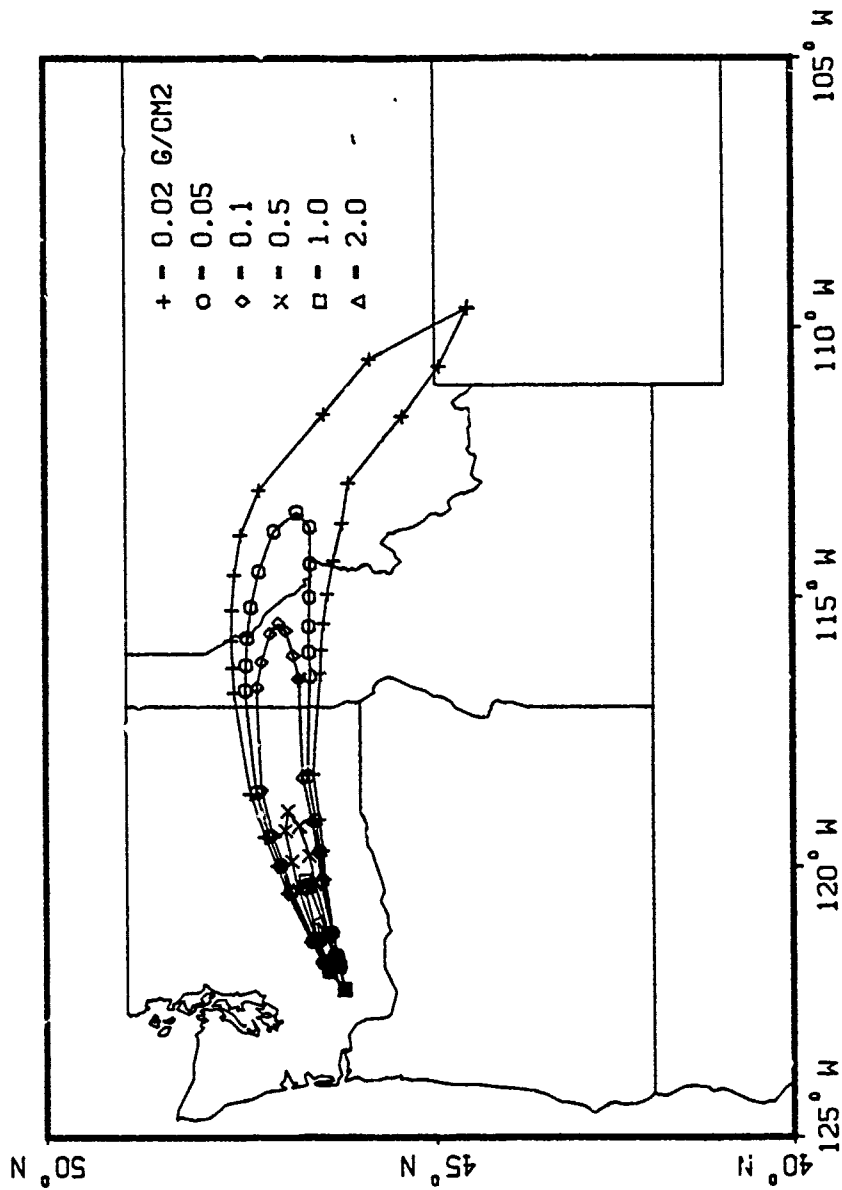
Figure V-19. Isomass Contours

87
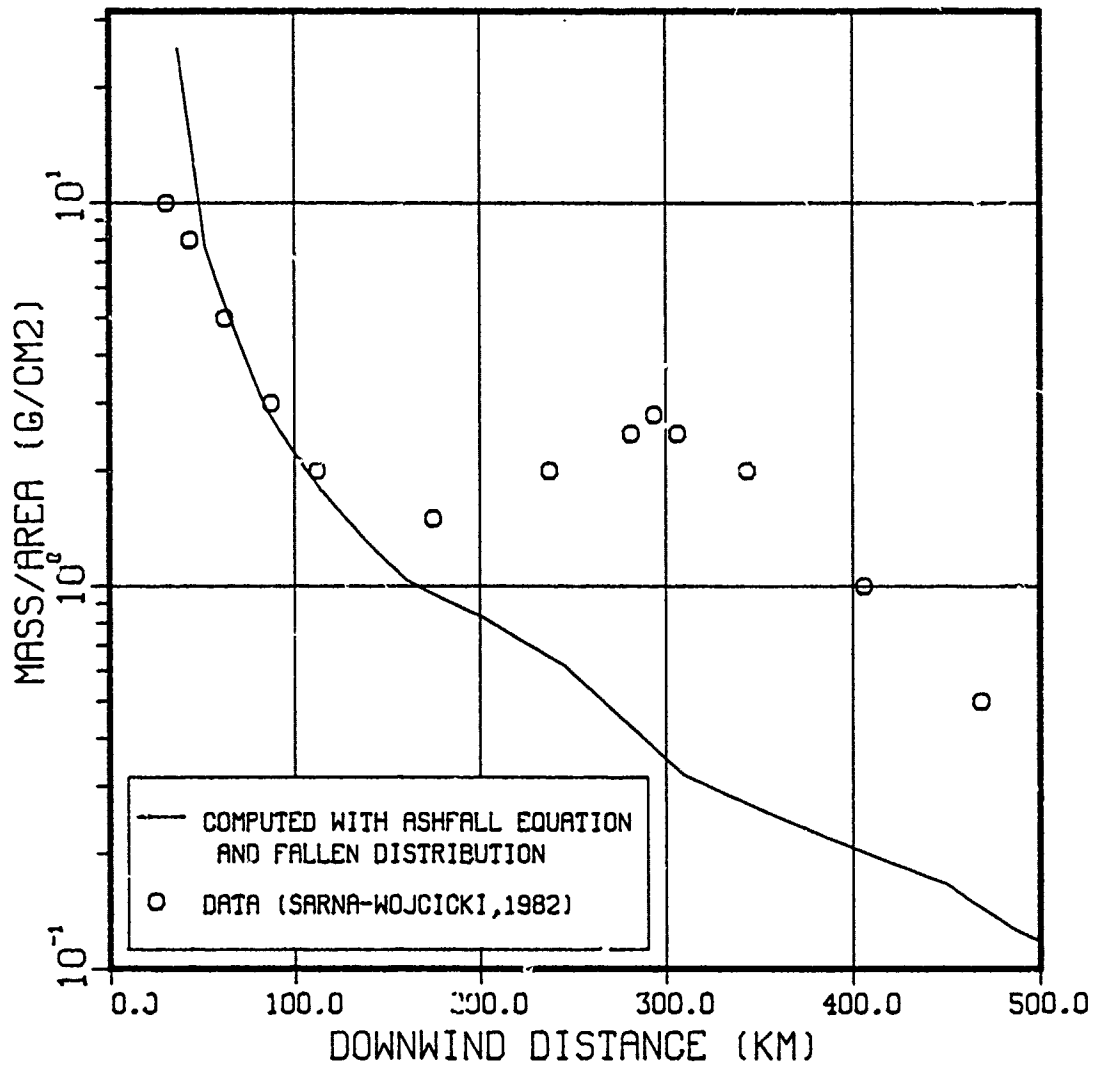
Figure V-20. Isomass on Hotline

velocity calculations. Figure V-21 shows where theoretical fall calculations predict that particles of various sizes and densities would land. Computed sizes are consistently larger than measured sizes landing at the same place.

Using Eq (5.7), the actual ashfall data and the function minimization technique (Appendix G), a particle mass-size frequency spectrum was back-calculated for the falling cloud. Specifically, a size distribution function, $M'(r)$, was found that enables the ashfall equation to closely match the ashfall data, including the Ritzville bulge (90). Table V-4 shows the parameters for $M'(r)$; the function is plotted in Figures V-22 and V-23. The size spectrum has a mode near 60 μm and particles smaller than 10 μm constitute less than 10% of the falling cloud mass, compared to 40% of the measured fallout mass. It is interesting to note, however, that the measured size distribution (Figure V-17) also contains a mode near 60 μm. The presence of that 60 μm secondary mode in the measured size distribution could be an artifact of its parent, falling cloud distribution, diminished by the particle breakage that produced the dominant measured mode near 8 μm.

The back-calculated cloud particle size spectrum was used in Eq (5.7) to compute ash mass on and around the hotline. Figure V-24 shows the hotline mass compared to measured data; the Ritzville bulge is accurately replicated. Isomass contours in Figure V-25 also show the Ritzville bulge with appropriate widening of the 1.0 gram per square centimeter contour around Ritzville.

At distances beyond 500 kilometers from the volcano, contours computed from spectral winds are slightly east of the contours extrapolated
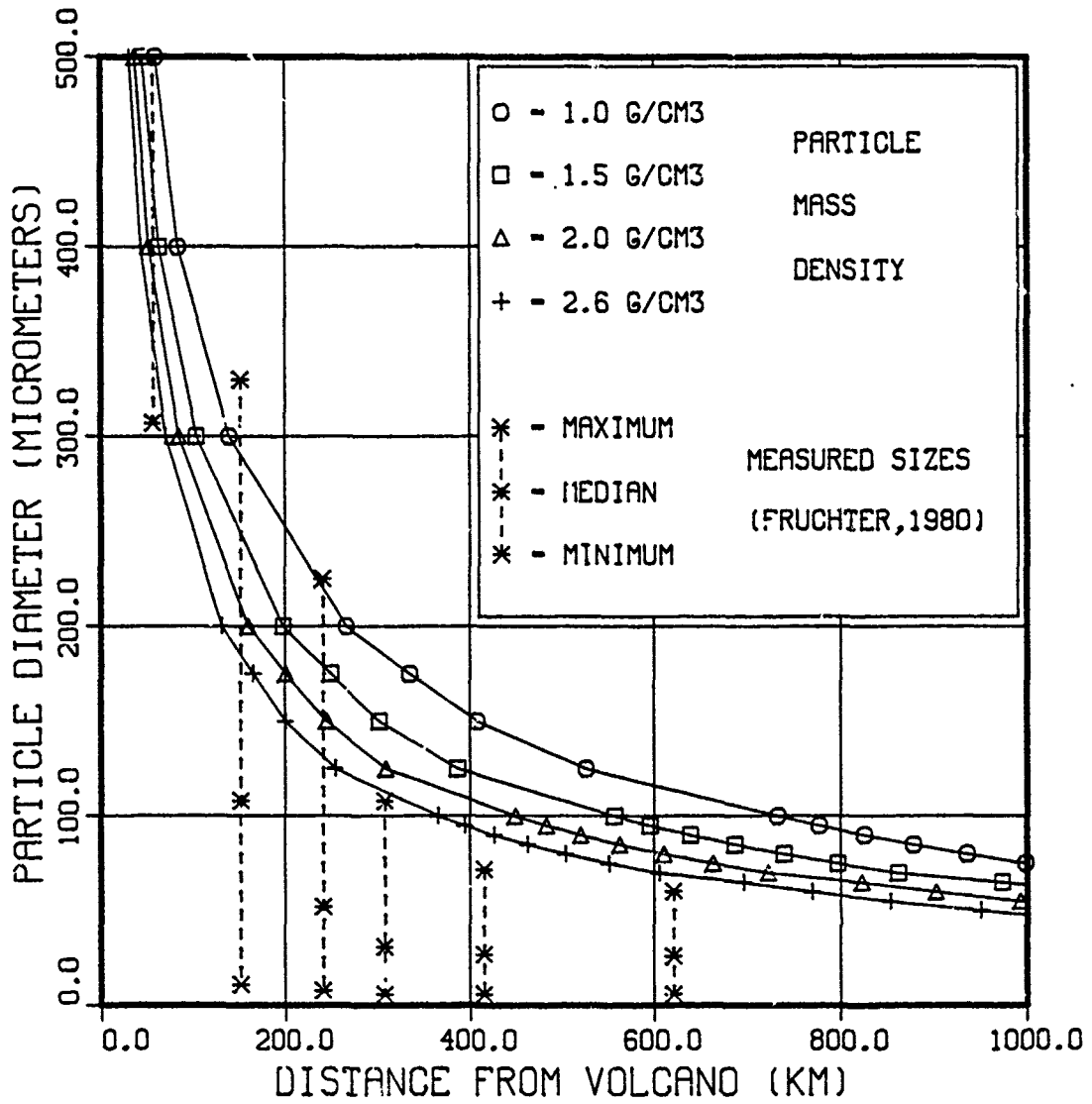
Figure V-21. Particle Size vs Distance from Volcano

TABLE V-4

Trimodal Log-Normal Function Parameters

for the Falling Particle Sizes

i	α_i	β_i	fi
1	4.075	0.333	0.14
2	4.085	0.133	0.39
3	4.267	1.297	0.47
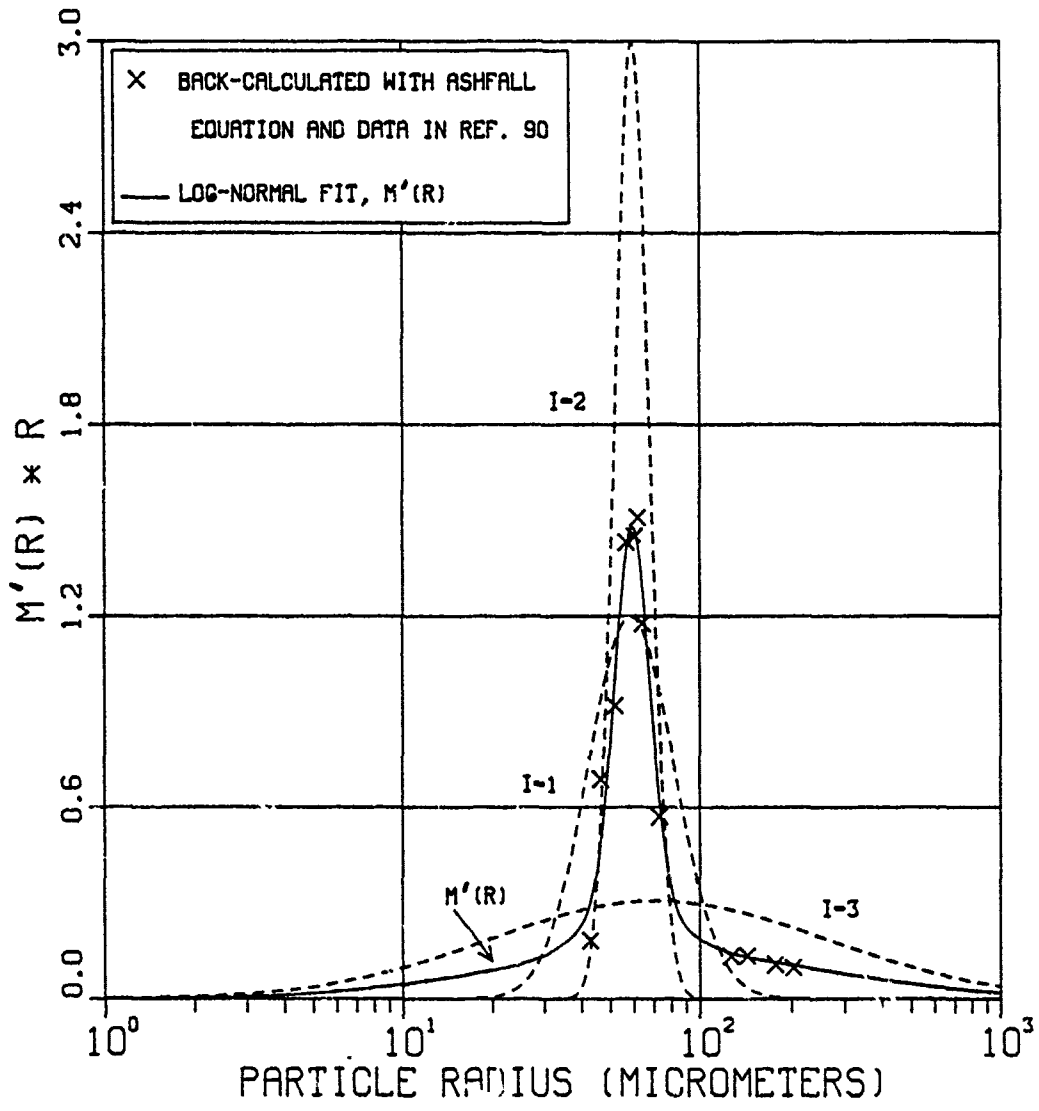
Figure V-22. Calculated Falling Particle Size Distribution
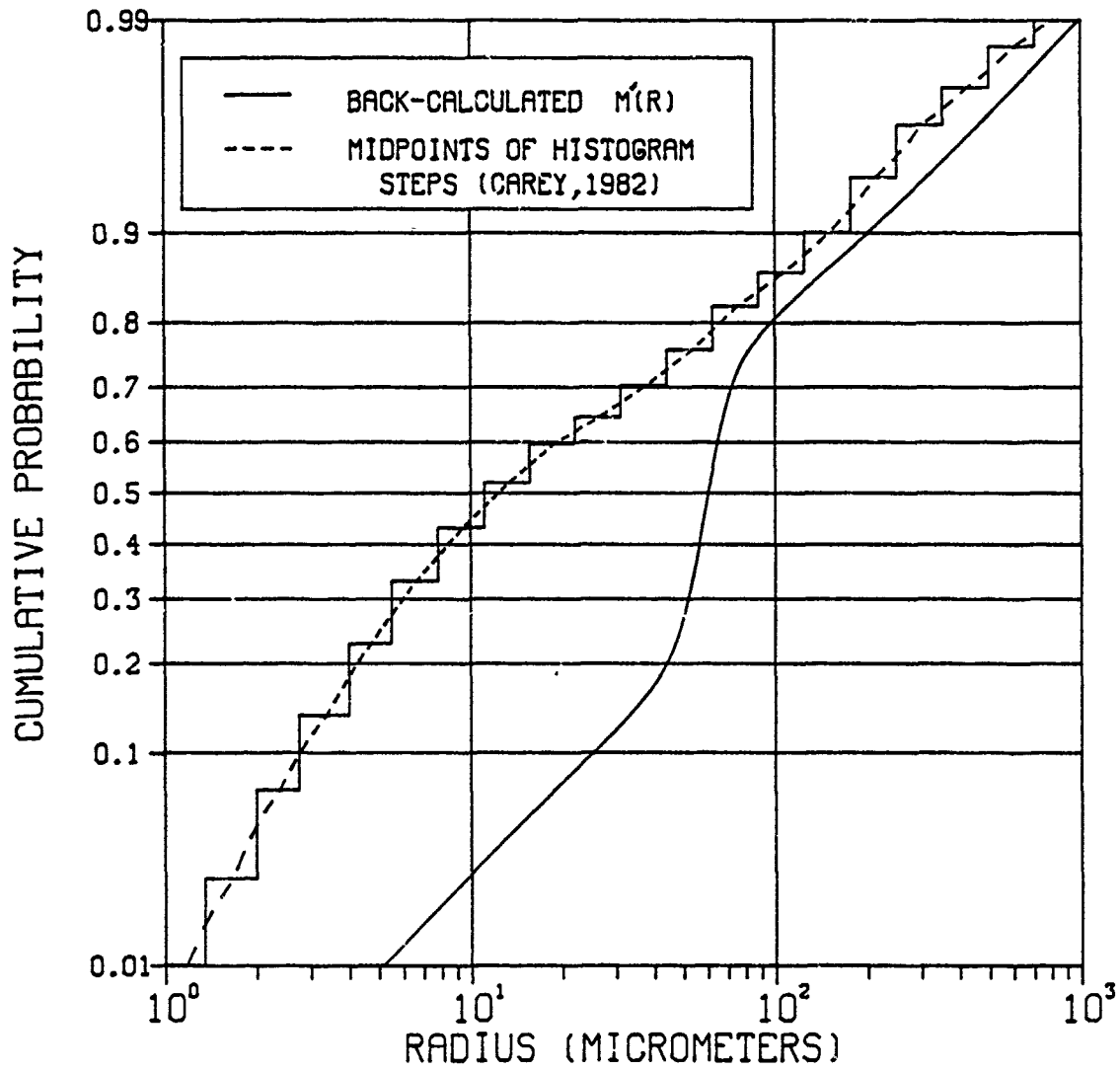
Figure V-23. Calculated Falling Particle Size Distribution (Cumulative)
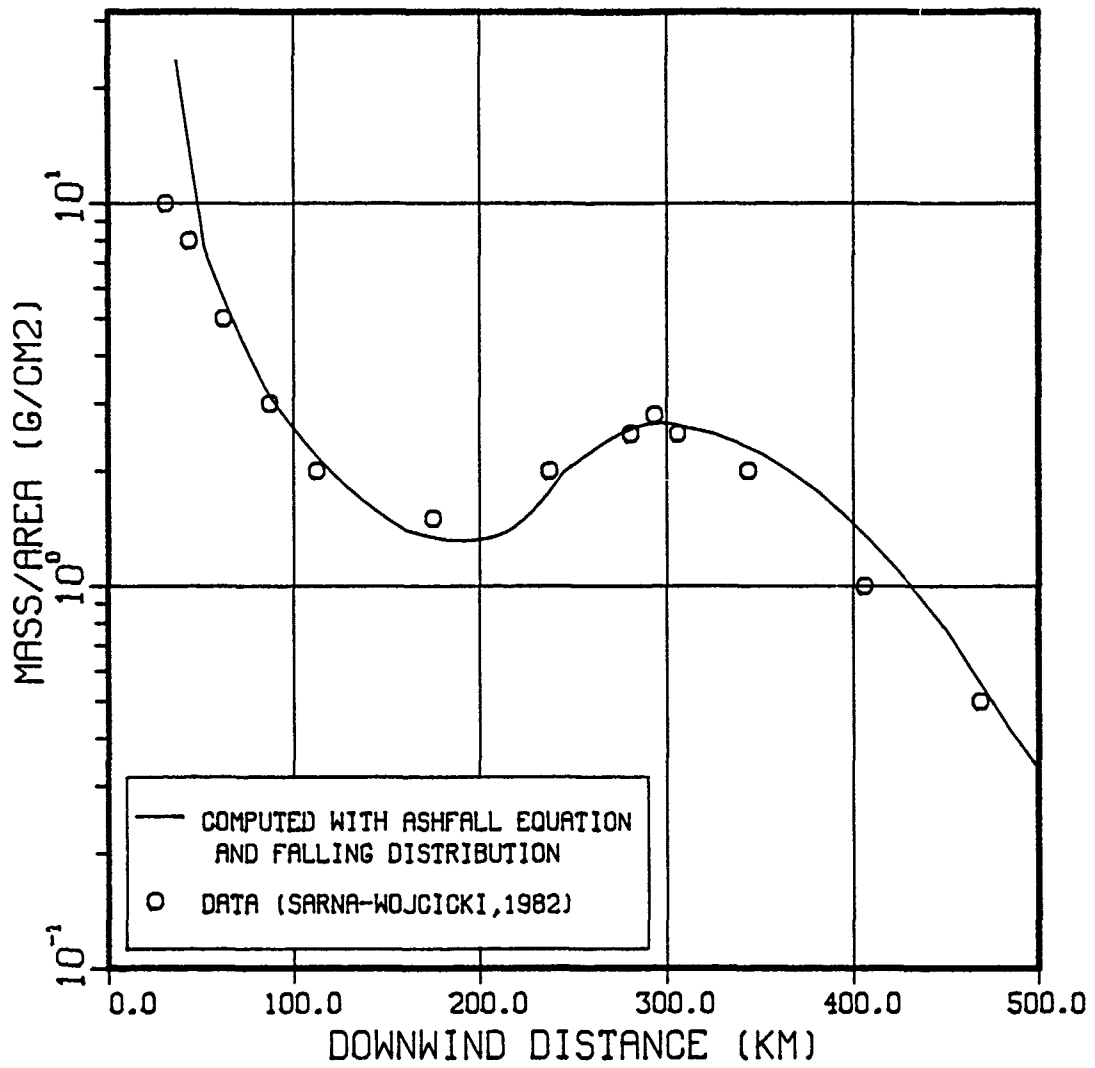
Figure V-24.   Isomass on Hotline (Falling Cloud Size Spectrum)

94
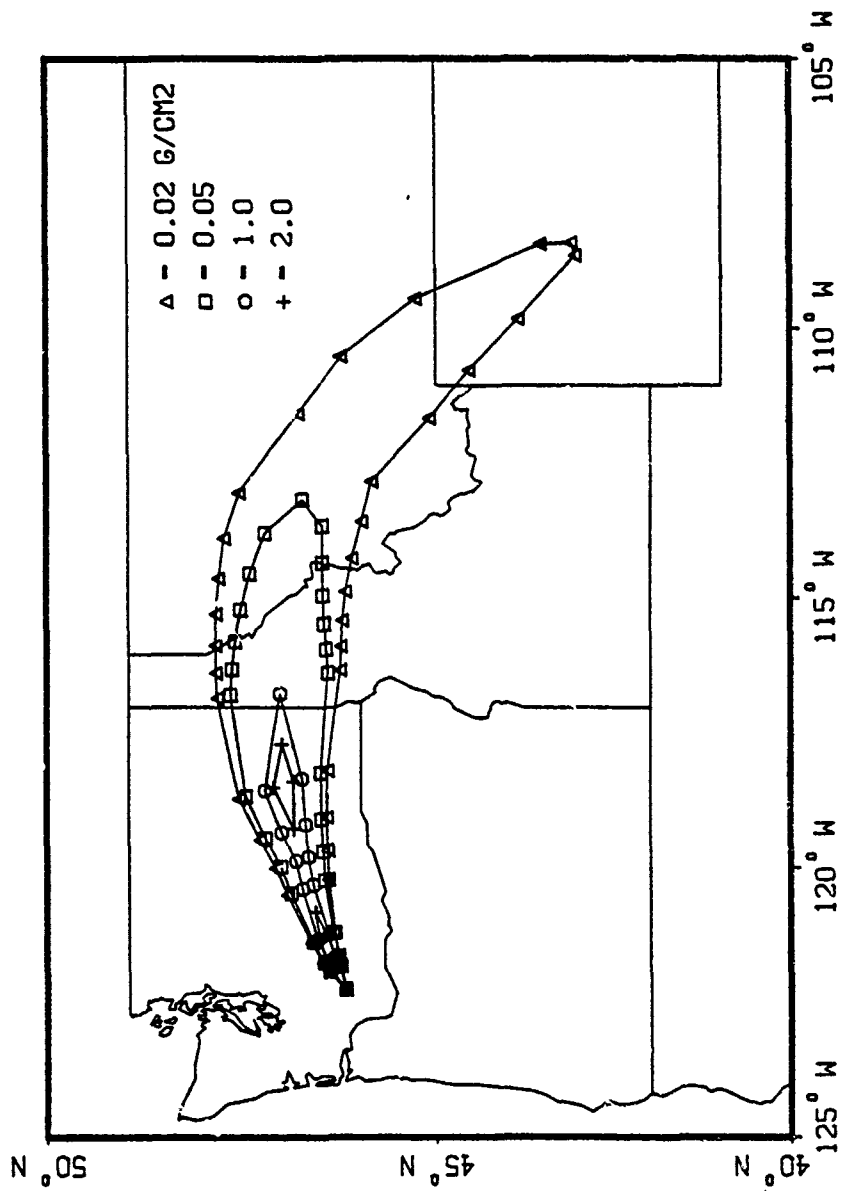
Figure V-25. Isomass Contours (Falling Cloud Size Spectrum)

from fallout and satellite data (see Figure V-3). Ashfall data from South Dakota strongly suggests that the extrapolated data contours in Figure V-3 are not accurately positioned (28). In fact, the computed contours in Figure V-25 may better represent the actual ashfall locations at those long ranges.

Summary. Using spectral winds for particle transport, the Mount St. Helens ashfall hotline was accurately computed, using a gravity-sorted initial cloud located at approximately 12 kilometers AGL. Spectral winds also produced long range isobaric trajectories that agreed with NOAA predictions of ash transport over the United States and Canada. Computed fallou.. arrival times agreed with eyewitness accounts. An ashfall equation was derived to predict volcanic ash mass at downwind points. The measured fallout mass-size frequency distribution cannot produce the Ritzville bulge in fallout calculations. A particle size distribution was determined for the falling cloud, using the ashfall equation and ashfall data. The computed falling cloud spectrum simulates the Ritzville bulge and suggests that a secondary mode in the measured distribution is an artifact of the falling cloud's mass-size frequency distribution. Figures V-26 and V-27 show isomass surfaces in three dimensions, computed with the falling and fallen particle size distributions, respectively. Each plot displays 5000 values determined at surface positions that are nodes of a Cartesian grid, with four kilometer spacing laterally. The method derived in Appendix F was used to find the hotline points associated with each of the 5000 surface positions. The vertical axis is the natural logarithm of ash mass, normalized to the peak value near the volcano, and truncated at 1.0% of the peak value.
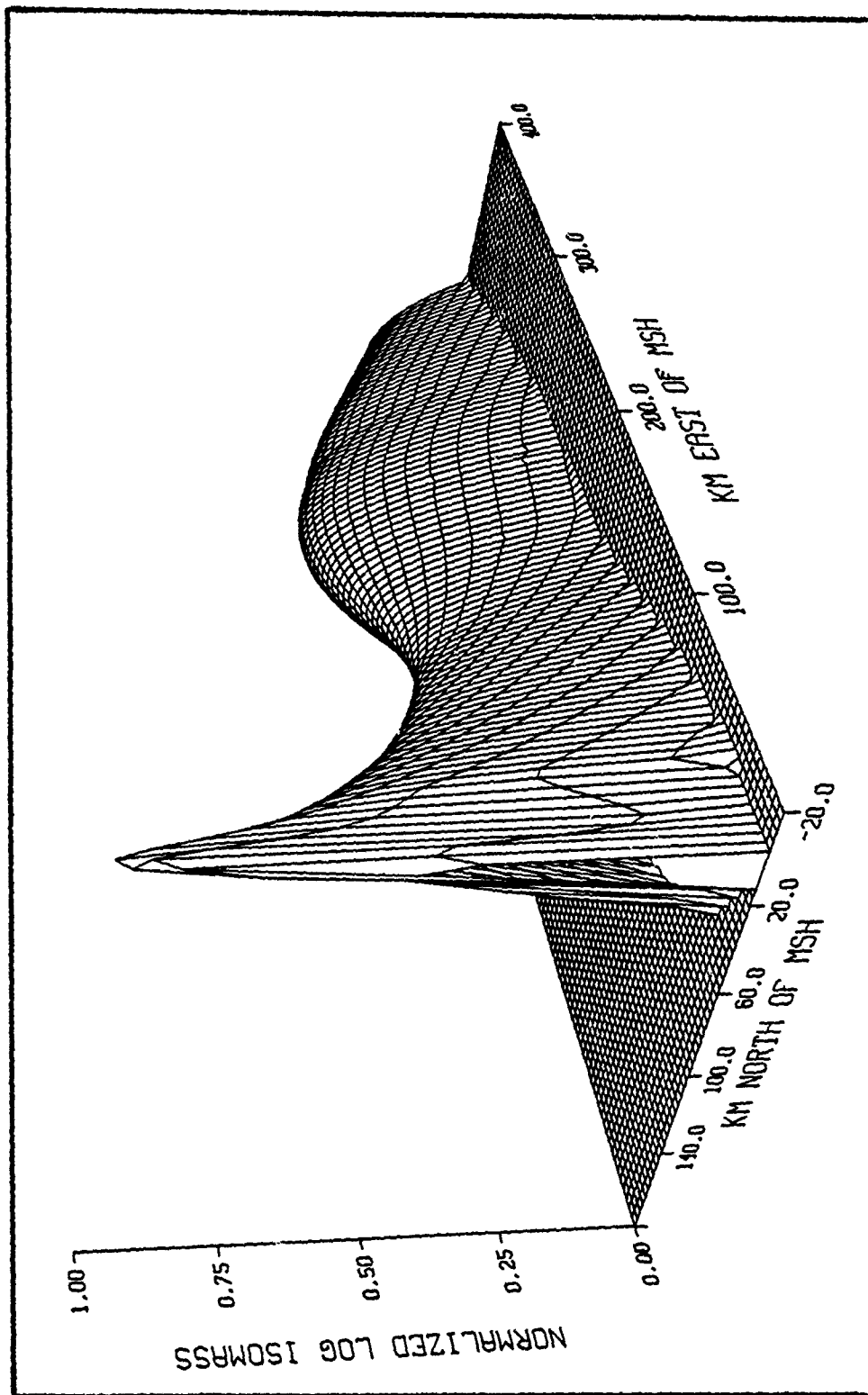
Figure V-26. Three Dimensional Ashfall (Falling Cloud Size Spectrum)
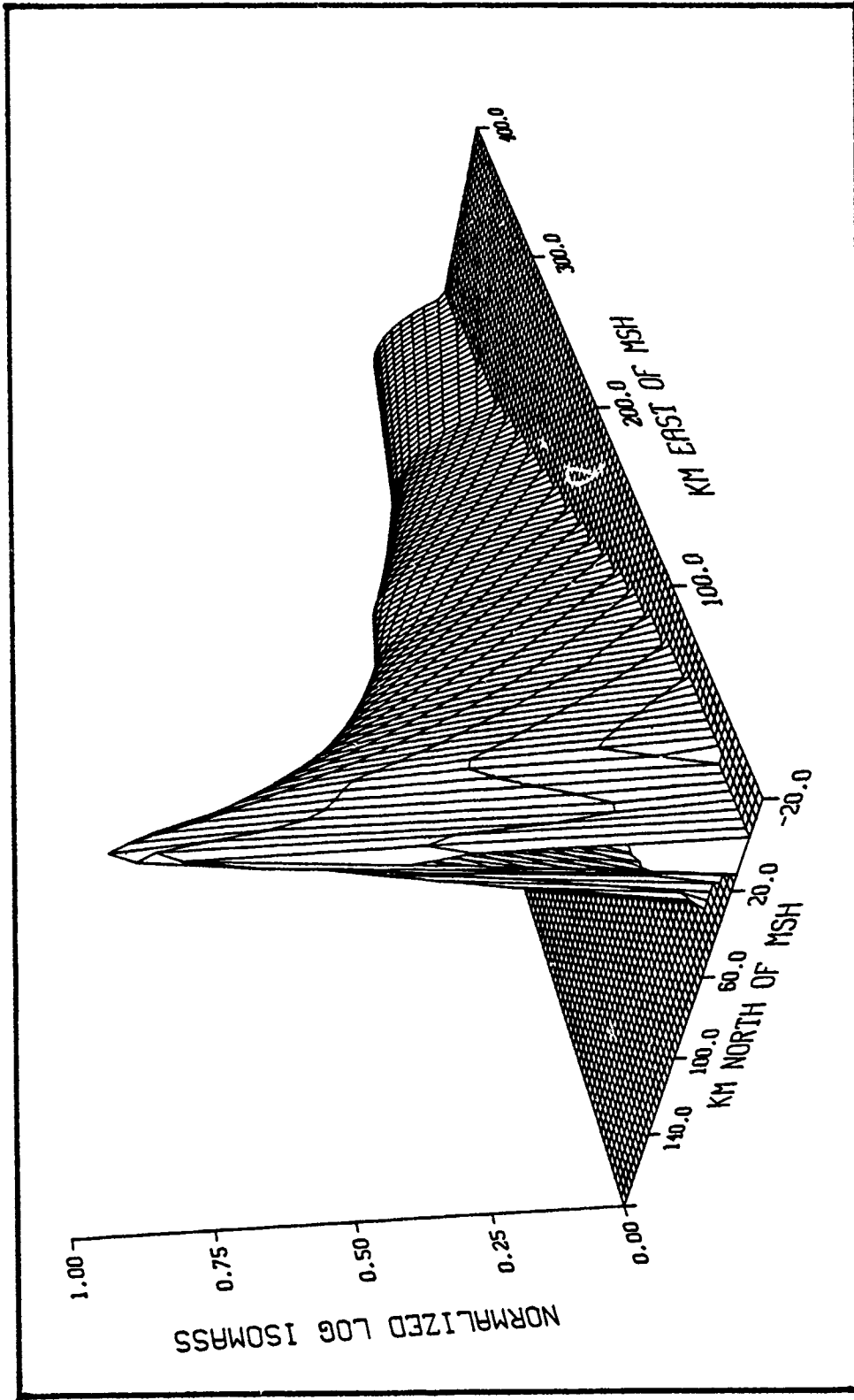
Figure V-27. Three Dimensional Ashfall (Fallen Cloud Size Spectrum)

98

DIRECT COURSE High Explosive Cloud Analysis

Description of Test Event. A six hundred ton sphere of high explo-
sives was detonated on 26 October 83 at the White Sands Missile Range.
The explosives were suspended from a fiberglass and steel tower, approxi-
mately fifty meters above ground level (AGL) to simulate a weapon airburst.
The explosion produced a particle cloud containing explosive by-products,
dirt and tower debris that rose to approximately 3000 meters AGL as it was
transported to the northwest by prevailing winds. Climatologically, winds
are westerly, so DNA's debris (not radioactive) fallout collection experi-
ments had been positioned to the east of ground zero before the test. No
debris fallout data was obtained. However, DNA tracked the cloud with
cameras and with a sampling aircraft, so the cloud motion data could be
used to validate the spectral wind transport model.

This test is a good validation exercise for spectral wind transport.
The relatively low cloud simulated a cloud from a kiloton range nuclear
burst. The coefficients are least accurate in the lower part of the
atmosphere due to terrain and boundary layer shear effects. Furthermore,
the cloud was tracked for distances less than the spacing between most
wind observation sites used to generate the spectral coefficients. Thus,
it was theoretically possible for cloud transport to be affected by atmo-
spheric disturbances too small to appear in the spectral model.

Spectral Winds. The NMC provided two sets of spectral coefficients:
12UT 26 Oct 83 and 00UT 27 Oct 83. The explosion occured at 18UT
26 Oct 83. The coefficients were written on magnetic tape (114) in the
same format as those provided for the Mount St. Helens analysis. Figures

V-28 through V-31 show spectral winds over the United States computed at the lowest four levels above ground for 00UT 27 Oct 83. Easterly flow over New Mexico is apparently caused by a strong low pressure system located over Northern Mexico. Figure V-32 shows wind speed vs altitude computed with coefficients and measured at the test site (22). The spectral winds lack the vertical resolution of radiosonde data and they do not model shear in the lowest layer of atmosphere. However, because the cloud transport was dominated by stronger winds at high altitudes, the spectral winds did model the westward motion of the cloud.

Cloud Motion. Isobaric trajectories are shown in Figures V-33 and V-34 for both sets of spectral coefficients. Figure V-35 shows isobaric trajectories using a new coefficient set, derived by linearly interpolating the 12UT and 00UT coefficients to represent winds at 18UT 26 Oct 83. The aircraft position data illustrates where the sampling aircraft was located when the pilot reported that he was in any part of the cloud or stem (23). Table V-5 shows the aircraft position data, including altitudes. Spectral winds most accurately modeled cloud transport near the cloud top (500 millibars). The spectral model clearly simulated the unusual easterly flow that dominated transport of the DIRECT COURSE cloud.

Summary. The DIRECT COURSE cloud was transported to the northwest by climatologically atypical winds (13)(14). Spectral winds predicted isobaric trajectories correctly, to the northwest. The cloud trajectory and spectral wind trajectory agree best near the top of the 3 kilometer high cloud. The low altitude spectral winds did not model the strong vertical shear in the 850 to 700 millibar level.
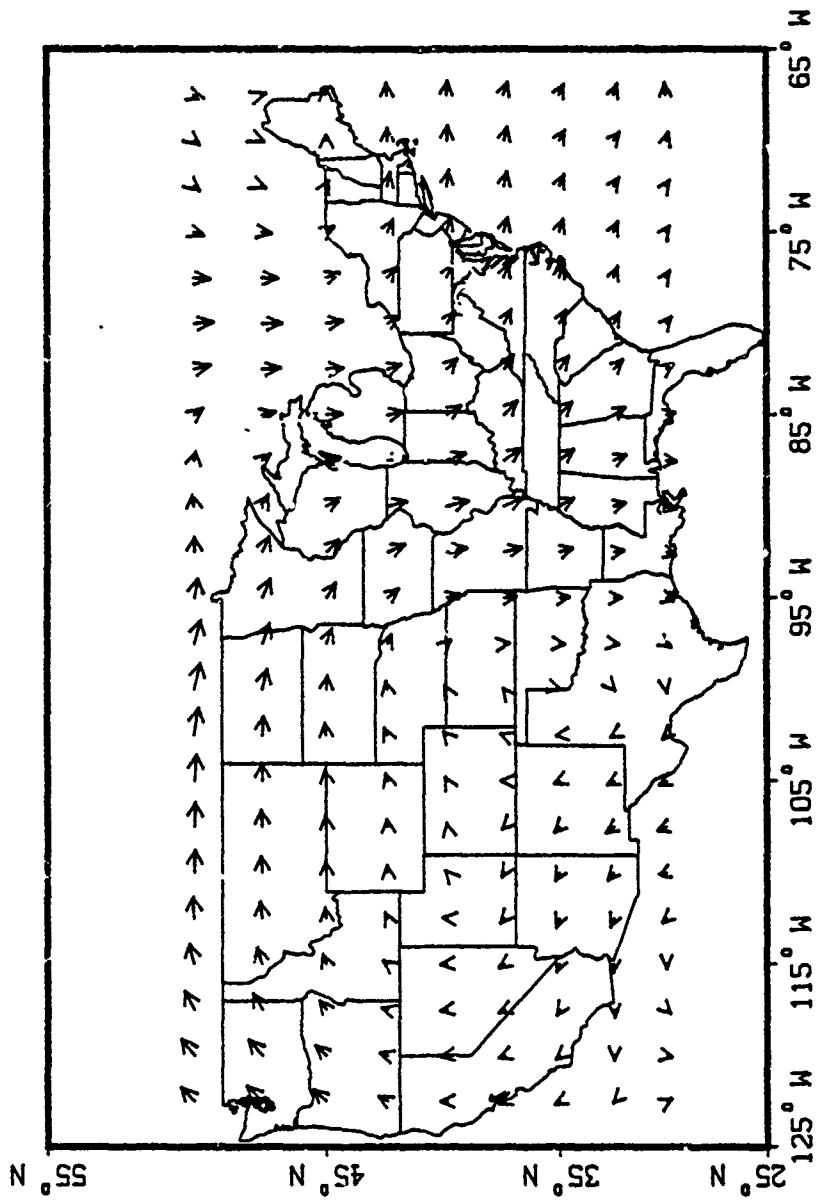
Figure V-28. 00UT 27 Oct 83 Wind Field (850 mb)

101
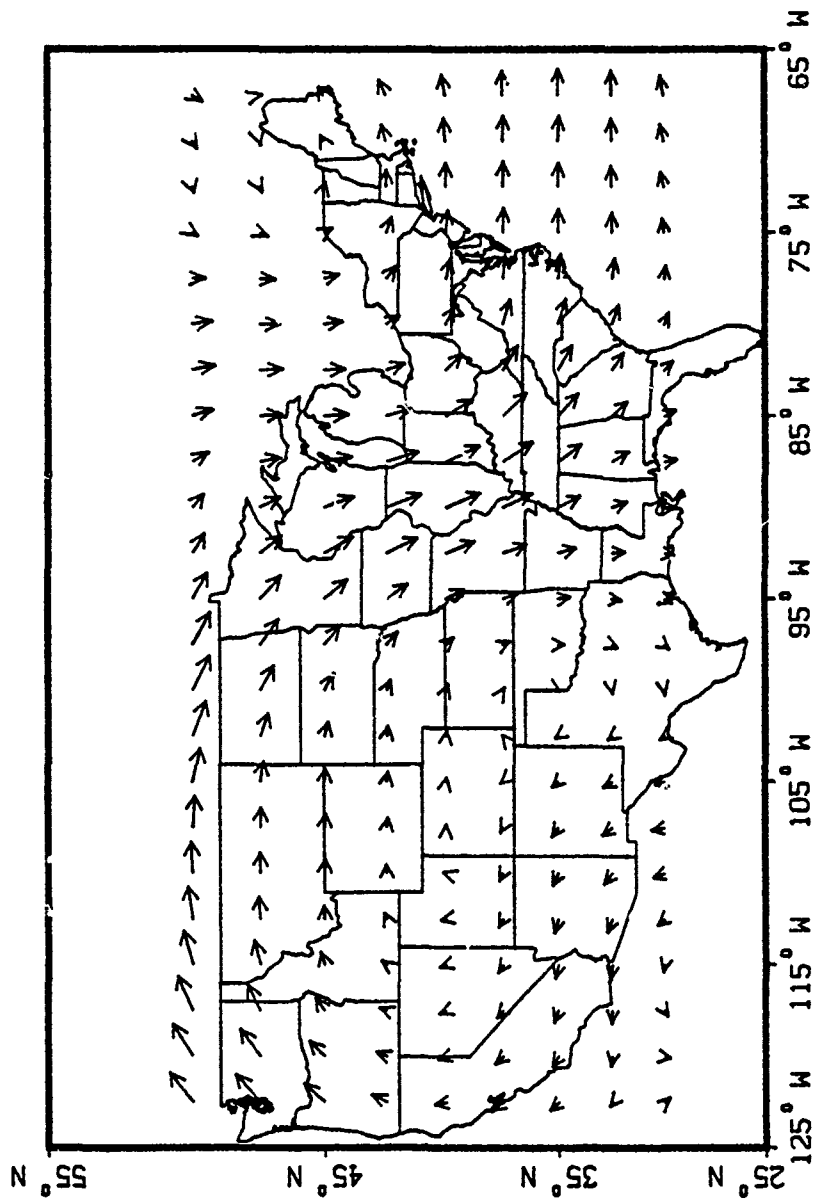
Figure V-29. 00UT 27 Oct 83 Wind Field (700 mb)

102
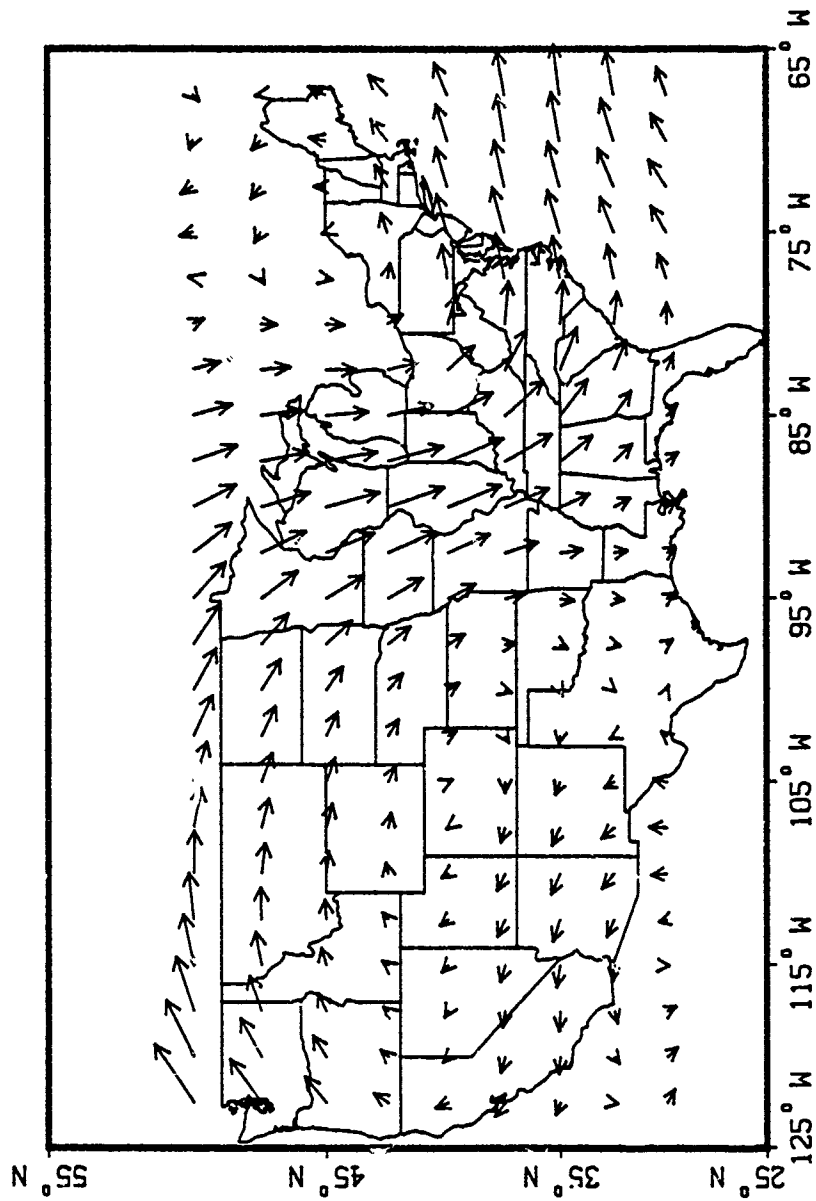
Figure V-30. 00UT 27 Oct 83 Wind Field (500 mb)
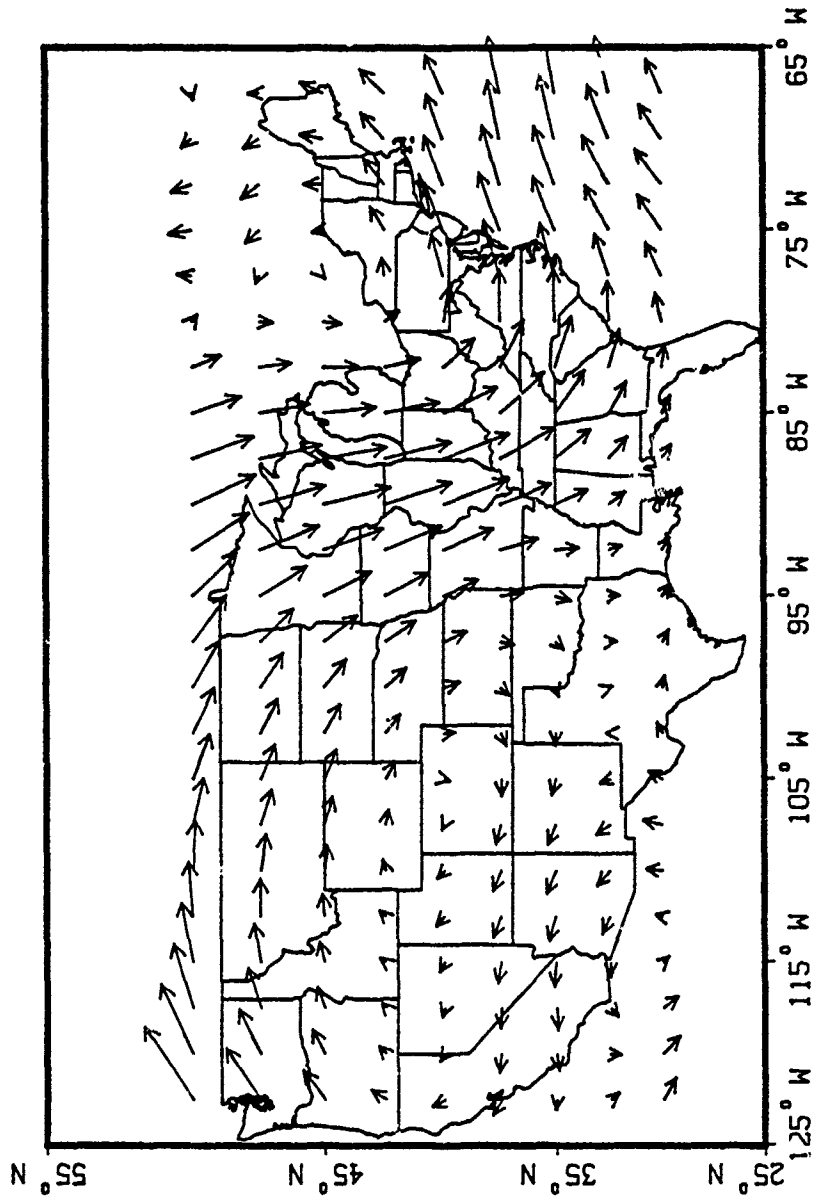
Figure V-31. 00UT 27 Oct 83 Wind Field (400 mb)
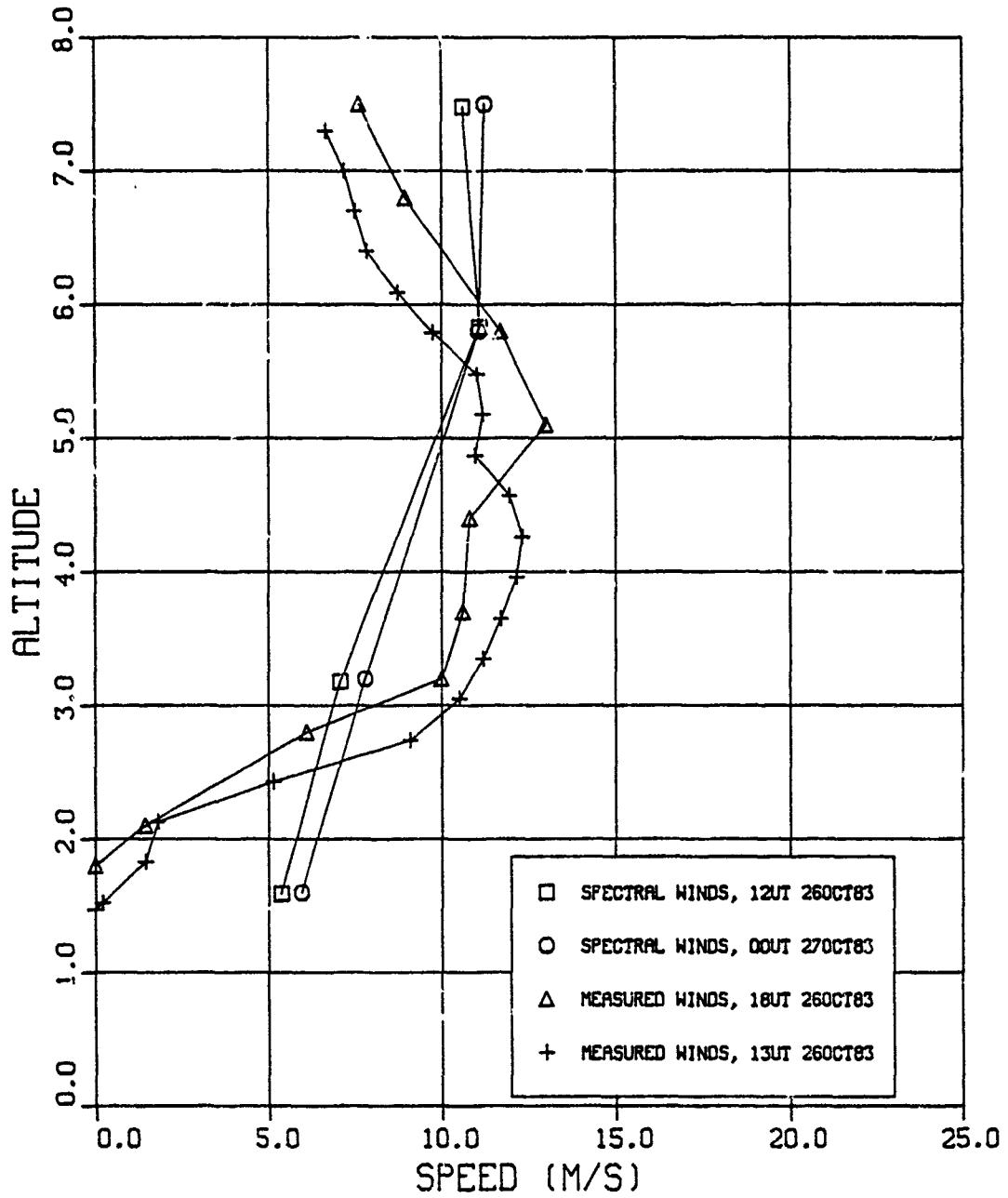
Figure V-32. Wind Speed vs Height
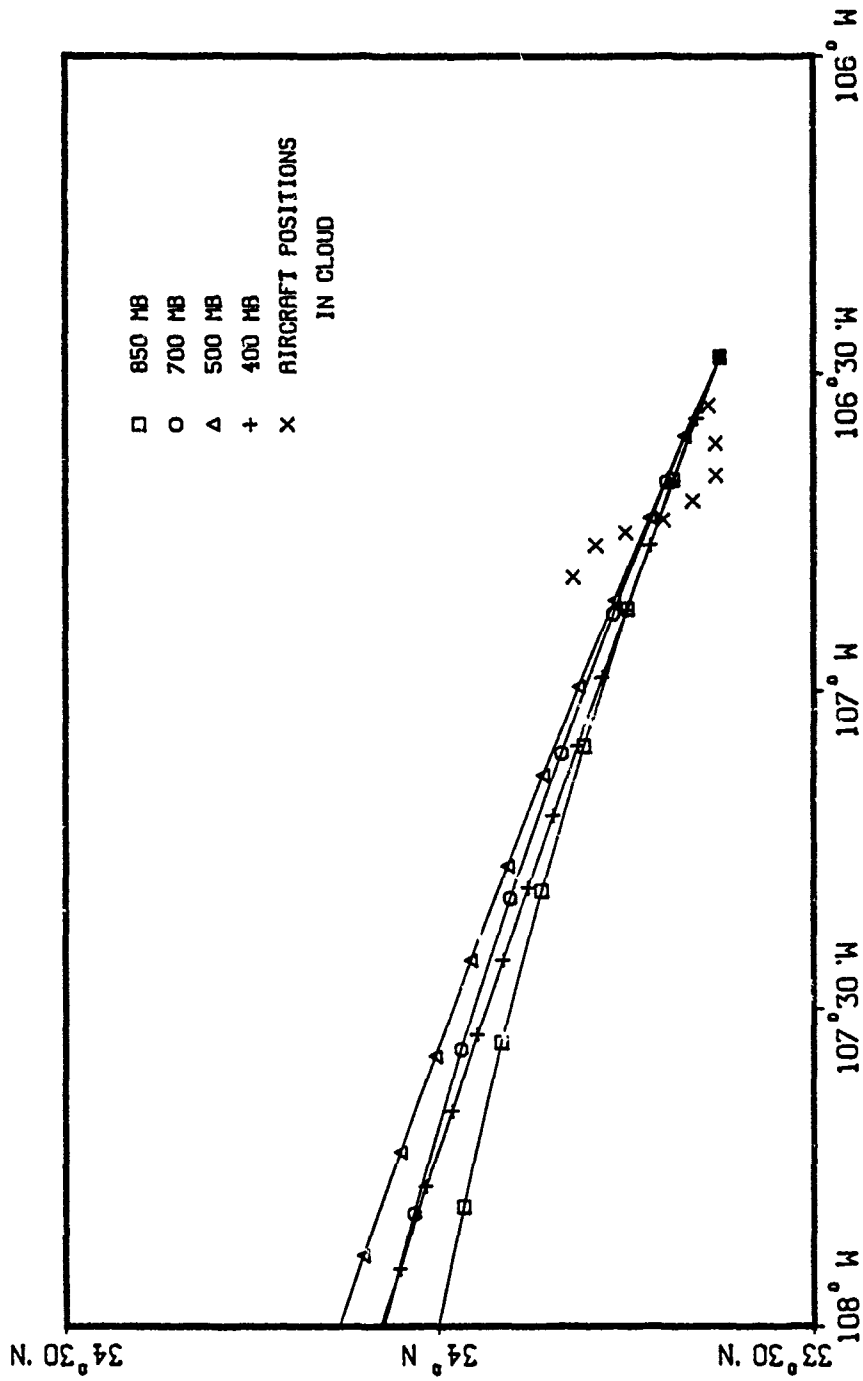
Figure V-33. Isobaric Trajectories 12UT 26 Oct 83
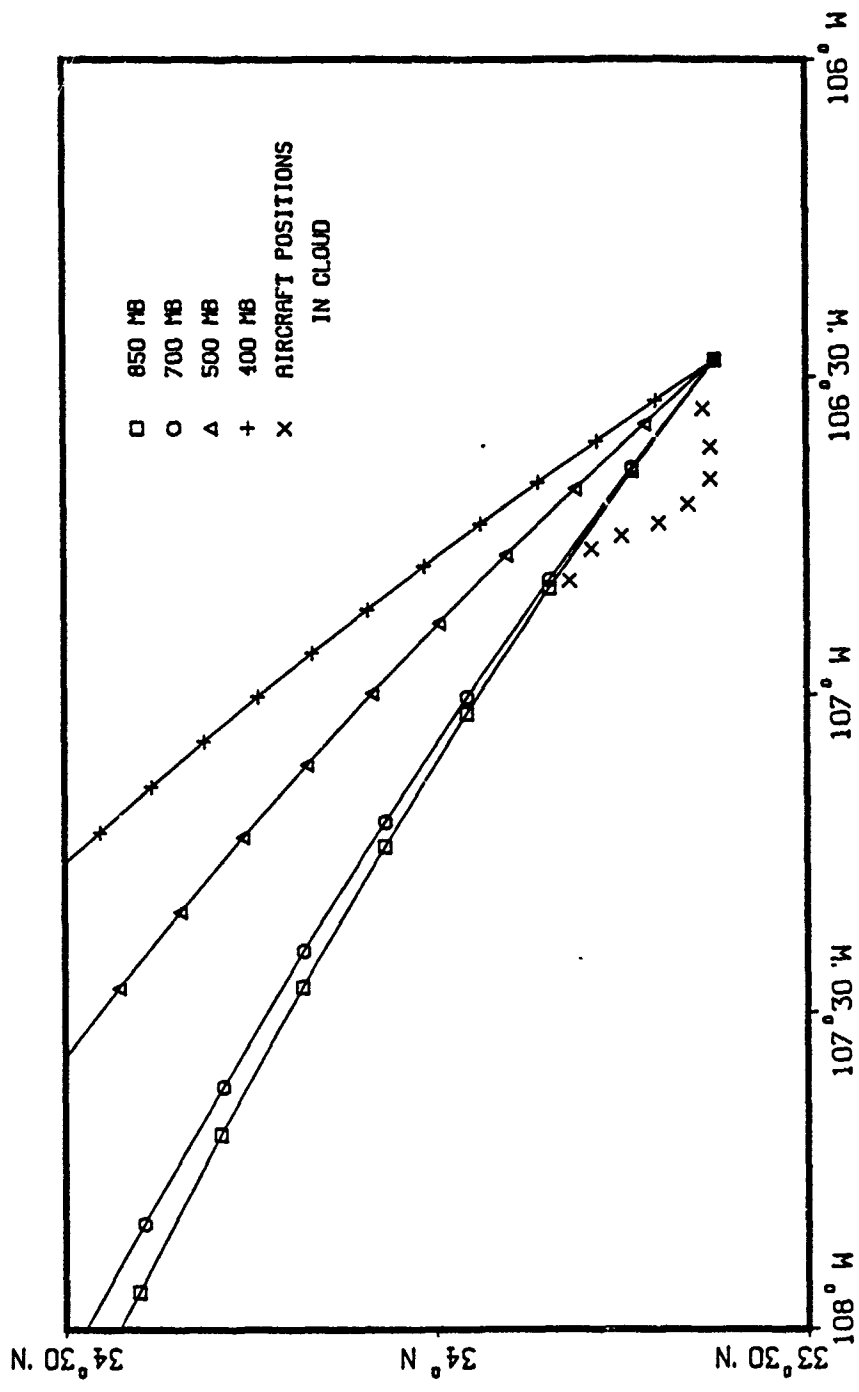
Figure V-34. Isobaric Trajectories 00UT 27 Oct 83
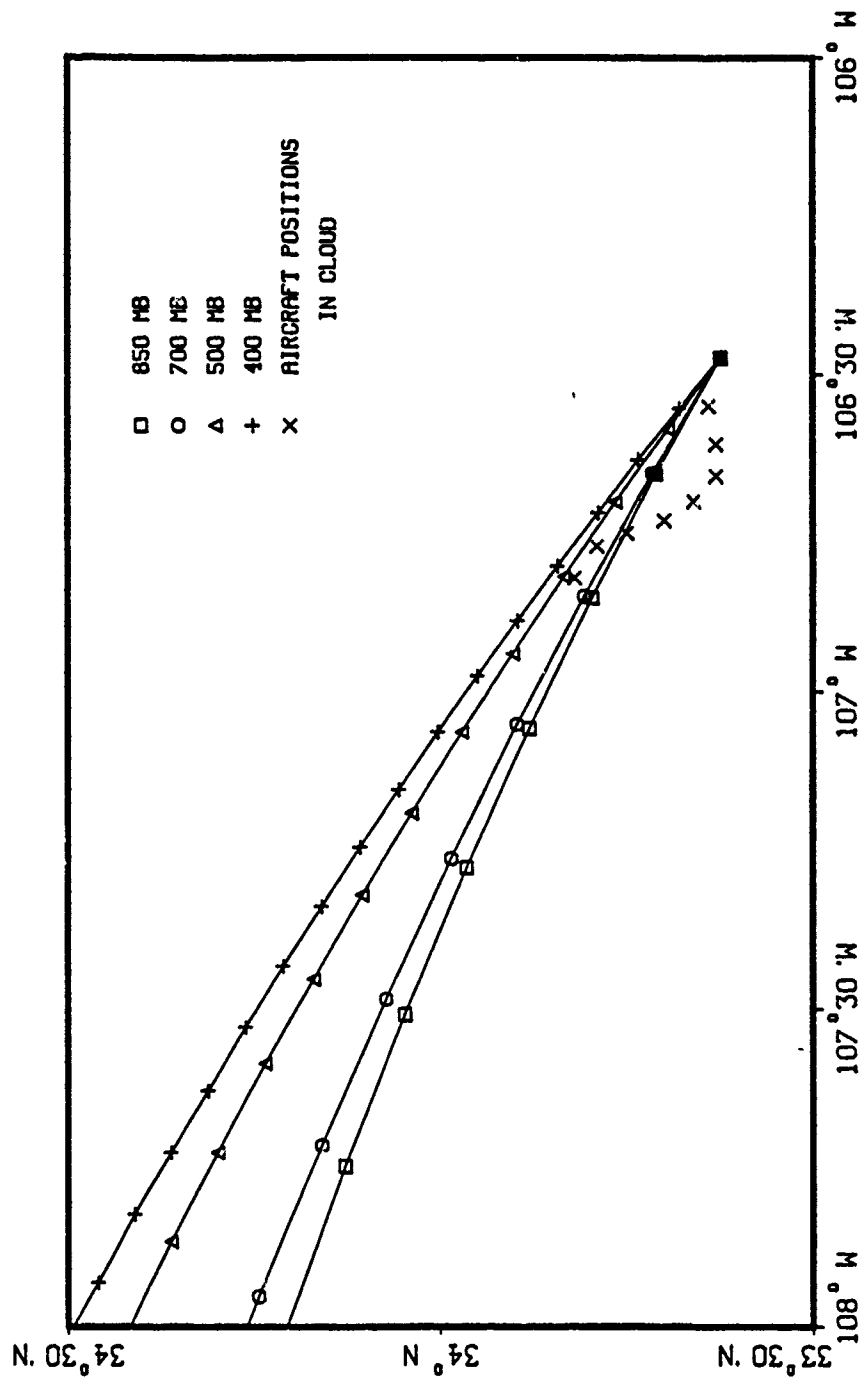
Figure V-35.   Isobaric Trajectories   18UT 26 Oct 83

TABLE V-5

Aircraft Positions in the DIRECT COURSE Cloud

Time	Altitude	Position	
MST	kilometers, AGL	kilometers West of ground zero	kilometers North of ground zero
13:00	0.87	7.4	1.7
13:01	1.07	12.6	0.8
13:02	1.33	17.2	0.8
13:03	1.42	20.8	5.0
13:04	1.51	23.5	9.5
13:05	1.67	25.2	15.0
13:06	2.03	26.5	19.9
13:08	2.79	31.7	23.3

VI. Error Analysis

Errors in the net wind components V_x and V_y were shown in Chapter V. They were determined by comparing the computed and actual arrival times of fallout from the Mount St. Helens ash cloud. The computed rms error of 2.1 meters per second in the net wind was even less than the average error of 5.0 meters per second in spectral wind vectors (Chapter II). This chapter addresses how uncertainties in the spectral winds contribute to error in computed dose rate.

Sources of Error

The error in a dose rate calculation is influenced by uncertainties in the independent variables of the dose rate equation, Eq (4.1). Standard deviations of several variables are listed in Table VI-1; deviations were based on the ranges of published values. Table VI-1 also shows best estimates of the variables used in this analysis.

Error Propagation Formula

An error propagation formula for the dose rate equation was derived by assuming that errors are symmetric about zero, and that errors in any two independent variables are uncorrelated (10).

$$\sigma_{\dot{D}}^2 \simeq \sigma_k^2 \left(\frac{\partial \dot{D}}{\partial k}\right)^2 + \sigma_Y^2 \left(\frac{\partial \dot{D}}{\partial Y}\right)^2 + \sigma_{ff}^2 \left(\frac{\partial \dot{D}}{\partial ff}\right)^2 + \sigma_{fv}^2 \left(\frac{\partial \dot{D}}{\partial fv}\right)^2$$

$$+ \sigma_{\alpha_0}^2 \left(\frac{\partial \dot{D}}{\partial \alpha_0}\right)^2 + \sigma_{\beta_3}^2 \left(\frac{\partial \dot{D}}{\partial \beta_3}\right)^2 + \sigma_{\beta_2}^2 \left(\frac{\partial \dot{D}}{\partial \beta_2}\right)^2 + \sigma_{S_x}^2 \left(\frac{\partial \dot{D}}{\partial S_x}\right)^2$$

$$+ \sigma_{S_y}^2 \left(\frac{\partial \dot{D}}{\partial S_y}\right)^2 + \sigma_{V_x}^2 \left(\frac{\partial \dot{D}}{\partial V_x}\right)^2 + \sigma_{V_y}^2 \left(\frac{\partial \dot{D}}{\partial V_y}\right)^2 \qquad (6.1)$$

TABLE VI-1

Nominal Values and Standard Deviations

of Variables in Dose Rate Equations

VARIABLE	NOMINAL	σ	REFERENCES
k,source normalization constant	$2350 \ \dfrac{R}{hr} \ \dfrac{mi^2}{kt}$	0.15 k	(12)(19) (41)(86)
ff,fission fraction	0.5	0.5 ff	(19)(31)(41)
α_o,logarithm of median particle radius	0.203	2.0	(12)
$\beta_3 = \beta_2$,logarithmic slopes of activity-size distributions	1.386	1.0	(12)
fv,volume distributed activity fraction	0.68	0.1 fv	(12)
(V_x, V_y),net wind vector components	computed with spectral winds	5 mps	(70)(108)(109) (110)(111)
(S_x, S_y),wind shear components	computed with spectral winds	50% of (S_x, S_y)	estimate
Y,weapon yield	1 megaton used for this analysis	0.1	estimate

The error propagation formula Eq (6.1) describes how errors may propagate from independent variables into a dose rate error. Generally, the variances are squares of the deviations estimated from published uncertainty bounds. Analytic expressions for partial derivatives were obtained by differentiating the dose rate equation with respect to each independent variable. The dose rate equation depends on net wind explicitly in the spatial distribution term and implicitly in the arrival rate term.

Dose Rate Error

A hypothetical megaton burst was studied to quantify the error in dose rate caused by uncertainties in the independent variables. Table VI-2 shows the relative and absolute magnitudes of wind component errors that contribute to dose rate errors. Values are averages for ten ground points located on the 200 Roentgen contour. The 200 Roentgen exposure contour was chosen because 200 Roentgens produce approximately 200 rems dose to the surface of a human body from .3 to 3 MeV gamma rays. A 200 rem dose is the threshhold for radiation sickness, based on data from Hiroshima and Nagasaki (41). Average dose rate on the contour is 42.3 R/hr at one hour after burst.

Spectral wind uncertainties contribute minimally to the error in computed dose rate. About 4% of the dose rate variance can be attributed to wind uncertainty when spectral coefficients are used for particle transport calculations. This analysis assumed that the deviation in net wind components was 5 meters per second. The net wind vectors computed in the Mount St. Helens analysis diverged from actual data by approximately 2 meters per second. Therefore, a spectral wind component

TABLE VI-2

Wind Error Contributions

		$u = V_x$	$u = V_y$
Dose Rate Error	$\sigma_u \left(\dfrac{\partial \dot{D}}{\partial u}\right)$	33.	30.
Relative Error	$\dfrac{\sigma_u \left(\dfrac{\partial \dot{D}}{\partial u}\right)}{\dot{D}}$	0.80	0.74
Fraction of Dose Rate Variance	$\dfrac{\sigma_u^2 \left(\dfrac{\partial \dot{D}}{\partial u}\right)^2}{\sigma_{\dot{D}}^2}$	0.043	0.039

may contribute even less than 4% of the dose rate variance.

The relative errors are consistent with similar error estimates determined by W. Slinn in his assessment of meteorological uncertainties affecting the Nuclear Regulatory Commission Reactor Safety Study (98). Slinn estimates that the relative error in radionuclide concentrations downwind of an accidental reactor release, due to wind speed uncertainties, is approximately 50% of the mean concentration. This error analysis indicated that wind-induced dose rate errors are 80% (maximum) of the mean dose rate.

VII. Summary, Conclusions and Recommendations

This chapter summarizes the analyses, findings and conclusions of this research. In general, the study demonstrated the feasibility of using spectral coefficients to compute fallout particle transport anywhere in the atmosphere. Spectral winds will improve state-of-the-art fallout modeling by accounting for wind variability effects on cloud trajectories. This new technique was validated by matching a volcanic ash cloud hotline and a high explosive cloud trajectory. Wind errors were actually quantified by comparing observed and calculated particle arrival times from the volcanic ash cloud.

Particle Transport with Spectral Winds

The NMC spectral coefficients were used with truncated orthogonal polynomials to compute wind vectors along trajectories of falling particles. Computed winds were linearly interpolated between the discrete spectral heights and between sequential times. Particle trajectories were smooth and continuous in all dimensions. Reducing the truncation limit to fewer than 30 waves significantly altered winds with speeds less than 1 meter per second. This study used data derived from radiosonde fits; forecasted coefficients could be used to predict fallout transport if real time data is not available (e.g. post-attack).

Variable Wind Smearing Model

Variable winds produced realistically curved hotlines, so a smearing code was developed that incorporated the two-step method to determine dose rate at a point.

Hotline Location. A hotline locator model was constructed, using spectral winds to transport an array of trace particles falling from the initial cloud to the ground. The hotline was defined as the piece-wise linear connection of particle landing points on the ground. The initial cloud was a correlation of DELFIC's gravity-sorted particle wafer heights. Sample hotlines were computed for several locations. Wind shear was also computed with spectral winds along each particle's trajectory.

Dose Rate Calculation. A fallout smearing model was developed for use with curved hotline coordinates that were generated by the hotline locator and spectral winds. The model determines the coordinates of any specified dose rate contour around a hotline. A technique was devised to compute dose rate at arbitrary points downwind of the burst. The two dimensional lateral spread of cloud activity is simulated with a bi-directional Gaussian function, normalized in the net crosswind direction. The dose rate equation for variable winds reduces to the constant wind equation when a constant unidirectional wind vector is assumed for cloud transport.

Mount St. Helens Analysis

Ash cloud data from the 18 May 80 eruption of the Mount St. Helens volcano was used to validate the new fallout transport method. With an initial cloud that was positioned within the observed heights of the stabilized eruption plume, the ashfall hotline location was computed with spectral coefficients provided by the NMC. The computed hotline location accurately replicated the actual fallout hotline and correctly

116

curved to the southeast through Idaho and Wyoming. Hotline position was not sensitive to particle density. Computed arrival times of volcanic ash at points on the ground were compared to observations, this comparison provided an excellent quantification of the uncertainty in the net wind vector computed with spectral winds.

Hotline calculations with spectral coefficients for four different times showed that particle transport was dominated by winds reported for 00UT 19 May 80. Temporally varying spectral winds were computed by interpolating spectral winds. Those calculations showed that part of the plume's lateral spread was caused by time-varying winds during the nine hour eruption. Isobaric trajectory calculations with spectral winds also agreed with published data, showing low altitude ash going eastward over Canada and high altitude ash over the United States.

A volcanic ashfall equation was derived from the dose rate equation. Mass per unit area of volcanic ash was computed along the hotline, and isomass contours were determined using a measured ash particle size distribution. Computed contours were similar to fallout data, but they did not replicate the Ritzville bulge. Using the ashfall data, a particle size distribution was back-calculated that did reproduce the mass bulge in isomass contours and on the hotline. The back-calculated distribution had a single mode near 60 μm; the measured distribution was trimodal, with modes near 8, 60 and 250 μm. The 60 μm mode in the measured distribution may be an artifact of the actual falling cloud's size spectrum, before collision, impact and mechanical sieving broke the aggregate, clustered particles into smaller, constituent pieces. By analogy, particle breakup may also have happened in nuclear fallout

particle measurements, especially in Pacific tests where large amounts of water were entrained into the cloud, facilitating aggregation of small particles into larger clusters.

DIRECT COURSE Analysis

The actual cloud trajectory was determined from visual and air-craft tracking data. Isobaric trajectories were computed with two sets of spectral coefficients supplied by the NMC. Spectral winds correctly specified the northwestward cloud motion. However, comparisons of actual wind profiles with spectral wind profiles demonstrated that spectral winds, as expected, lack vertical resolution and shear between the lowest spectral height and the ground. Accordingly, the spectral winds more accurately replicated the trajectory of the top half of the high explosive cloud than the bottom half. Particle transport with spectral winds should be most accurate when the initial cloud is so high that the earth's boundary layer is a small part of the particles' trajectories.

Error Analysis

An error propagation formula was used to quantify the effects of wind (and other variables') uncertainties on computed dose rate. Wind component uncertainties contributed approximately 4% of the variance in dose rate, assuming ±5 meters per second for the net wind uncertainty, based on errors in spectral wind vectors. The Mount St. Helens data suggests that the net wind uncertainty is actually closer to ±2 meters per second, so wind contributions to dose rate error may be much less than 4% of the dose rate variance.

118

Recommendations

1. Use forecast coefficients to determine how far in advance trajectories can be accurately predicted. This study used coefficients for winds at data observation times. The NMC can derive forecast coefficients using a global circulation model.

2. Modify DELFIC to use spectral winds. However, realistically variable winds may exacerbate the numerical break-up problem previously observed with DELFIC at long ranges. Wafers may become widely separated in variable winds.

3. Develop a set of spectral coefficients from archived wind data for six nuclear tests. The nuclear tests should be the same ones previously used to benchmark DELFIC, WSEG, and DNAF-1 fallout codes. (Test Event Codenames: Johnie Boy, Jangle-S, Small Boy, Koon, Zuni, and Bravo) Use the coefficients and fallout data to further validate the spectral wind transport method.

4. Develop a particle aggregation model, accounting for the key processes that promote aggregation in particle clouds.

5. In future volcanic ash fallout experiments, measure the falling particle size distribution, using nondestructive techniques, such as cameras and laser spectrometers,to discriminate between falling and fallen particle size spectra.

Appendix A

Spectral Coefficients

Table A-1 contains some spectral coefficients for the westerly wind component on 00UT 16 Jan 82. There are three complex pairs per line, format (6E13.7). The coefficients are listed for the first two zonal wave numbers ($\ell = 0$ and 1). The immaginary parts are zero when $\ell = 0$, because only the real part of the summation is used to compute wind speed, and the spherical harmonics are real when $\ell = 0$; see Eq (2.3).

TABLE A-1

Spectral Coefficients

-.3637244E+00	0.0	-.5837291E+00	0.0	0.2643273E+01	0.0
0.1432105E+00	0.0	-.2404544E+01	0.0	0.2174675E-01	0.0
-.9834955E+00	0.0	0.1C31541E+01	0.0	0.1758606E+01	0.0
-.9824724E+00	0.0	-.4760414E-01	0.0	0.2479262E+00	0.0
-.2306027E+00	0.0	-.3866760E+00	0.0	-.1417527E+00	0.0
0.2052744E+00	0.0	0.1106223E+00	0.0	0.2658754E+00	0.0
0.2633099E-01	0.0	-.9235412E-01	0.0	-.1829985E+00	0.0
-.8426303E-01	0.0	0.9221262E-01	0.0	-.2185238E+00	0.0
-.1263896E-01	0.0	0.1788903E+00	0.0	-.9426903E-02	0.0
0.1161274E-01	0.0	0.1279462E-01	0.0	0.4710592E-02	0.0
-.1094541E-01	0.0	-.1806136E-02	0.0	0.4023800E+00	-.1175773E+00
0.1272392E+00	-.1290352E+00	-.2386734E+00	0.3597328E+00	0.2547010E+00	0.2196925E+00
-.6665641E-01	-.6895614E+00	-.1262648E+00	-.1289409E+00	0.3910370E+00	-.2788864E-01
-.1503941E+00	-.2800477E+00	-.1066868E+00	0.4032145E+00	0.2364262E+00	0.3022929E+00
-.2404331E+00	-.1523106E+00	-.1790546E+00	-.2677168E+00	-.2876702E-01	-.1189634E-03
-.7729328E-01	0.1500818E+00	0.2486688E+00	-.1265156E+00	0.2571438E-01	0.9555286E-01
0.5862517E-01	0.2822241E+00	-.9516738E-02	0.8054072E-01	-.8246559E-01	-.5288965E-01
-.3773670E-01	-.2037801E+01	-.1322073E+00	0.1148806E+00	-.2309645E-01	0.1718027E-01
0.9333167E-02	-.1795435E+00	0.9305805E-01	0.4475105E-01	0.6534290E-01	0.2818696E-01
-.9247113E-02	0.2321525E-01	-.1644637E-01	0.1044125E-01	-.2708900E-02	-.1630729E-01
-.7532623E-02	-.9351436E-02	0.9087492E-02	-.1317627E-01	0.3604640E-03	0.4114226E-02

Appendix B

Derivation of Spectral Wind Equations

Wind vector components at a fixed height in the atmosphere are correlated in space with the following expansion:

$$(U,V) = (u,v)\cos\phi = \sum_{\ell=-J}^{J} \sum_{n=|\ell|}^{|\ell|+J+1} (U_n^{\ell}, V_n^{\ell})\, P_n^{\ell}(\sin\phi)\, EXP(i\ell\lambda) \qquad (B.1)$$

Terms are defined in Chapter II.

The ℓ-summation in Eq (B.1) can be expressed as follows:

$$\sum_{\ell=-J}^{J} = \sum_{\ell=-J}^{-1} + \sum_{\ell=0}^{0} + \sum_{\ell=1}^{J} \qquad (B.2)$$

Negative indices can be rewritten.

$$\sum_{\ell=-J}^{-1} \sum_{n=|\ell|}^{|\ell|+J+1} (U_n^{\ell}, V_n^{\ell})\, P_n^{\ell}(\sin\phi)\, EXP(i\ell\lambda)$$

$$= \sum_{\ell=1}^{J} \sum_{n=\ell}^{\ell+J+1} (U_n^{-\ell}, V_n^{-\ell})\, P_n^{-\ell}(\sin\phi)\, EXP(-i\ell\lambda)$$

$$= \sum_{\ell=1}^{J} \sum_{n=\ell}^{\ell+J+1} (U_n^{-\ell}, V_n^{-\ell})\, Y_n^{-\ell} \qquad (B.3)$$

Wind components are real variables, so (95:25)(15:689):

$$(U_n^{-\ell}, V_n^{-\ell}) = (-1)\ (U_n^{\ell}, V_n^{\ell})^* \qquad (B.4)$$

Complex conjugate is denoted by $*$. From (72:495):

$$Y_n^{-\ell} = (-1)^{-\ell} \, (Y_n^\ell)^* \tag{B.5}$$

Therefore, the negative ℓ-summation becomes:

$$\sum_{\ell=1}^{J} \sum_{n=\ell}^{\ell+J+1} (U_n^\ell, V_n^\ell)^* \, (Y_n^\ell)^* \tag{B.6}$$

$$= \sum_{\ell=1}^{J} \sum_{n=\ell}^{\ell+J+1} \{ \, [\, \mathrm{Re}(U_n^\ell, V_n^\ell) \,] \, P_n^\ell(\sin\phi) \, (\cos\ell\lambda)$$

$$+ [\, -i \, \mathrm{Im}(U_n^\ell, V_n^\ell) \,] \, P_n^\ell(\sin\phi) \, (-i \, \sin\ell\lambda)$$

$$+ [\, -i \, \mathrm{Im}(U_n^\ell, V_n^\ell) \,] \, P_n^\ell(\sin\phi) \, (\cos\ell\lambda)$$

$$+ [\, \mathrm{Re}(U_n^\ell, V_n^\ell) \,] \, P_n^\ell(\sin\phi) \, (-i \, \sin\ell\lambda) \, \} \tag{B.7}$$

U and V are real numbers; the real part of the summation with conjugates is the same without the conjugates. The real part of Eq (B.6) can be expressed as follows:

$$\mathrm{Re} \sum_{\ell=1}^{J} \sum_{n=\ell}^{\ell+J+1} (U_n^\ell, V_n^\ell) \, Y_n^\ell \tag{B.8}$$

Therefore, the spectral wind equation becomes a summation over positive indicies. Spectral wind components are determined with the following expression:

$$(U,V) = (u,v)\cos\phi$$

$$= \sum_{n=0}^{J+1} (U_n^0, V_n^0) \; P_n^0(\sin\phi) + \text{Re} \left[2 \sum_{\ell=1}^{J} \sum_{n=\ell}^{\ell+J+1} (U_n^\ell, V_n^\ell) \; P_n^\ell(\sin\phi) \; \text{EXP}(i\ell\lambda) \right] \quad \text{(B.9)}$$

Let A = 1 if $\ell = 0$; A = 2 otherwise.

$$(U,V) = (u,v)\cos\phi = \text{Re} \sum_{\ell=0}^{J} A \sum_{n=\ell}^{\ell+J+1} (U_n^\ell, V_n^\ell) \; P_n^\ell(\sin\phi) \; \text{EXP}(i\ell\lambda) \quad \text{(B.10)}$$

Associated Legendre Polynomials

P_n^ℓ are associated Legendre polynomials, normalized as in (9).

$$P_n^\ell(x) = \frac{(-1)^{\ell+n}}{2^n \, n!} \left(\frac{(2n+1) \, (n-\ell)!}{2 \, (n+\ell)!} \right)^{\frac{1}{2}} (1-x^2)^{\frac{\ell}{2}} \frac{d^{\ell+1}}{dx^{\ell+1}} (1-x^2)^n \quad \text{(B.11)}$$

To generate numerical values, the model uses the recursion relation (95):

$$x \; P_n^\ell(x) = \epsilon_{n+1}^\ell P_{n+1}^\ell(x) + \epsilon_n^\ell \; P_{n-1}^\ell(x) \quad \text{(B.12)}$$

where

$$\epsilon_n^\ell = \left(\frac{n^2-\ell^2}{4n^2-1} \right)^{\frac{1}{2}} \quad \text{(B.13)}$$

Belousov (9) shows the relation in the form:

$$P_n^m(x) = 2 \, a_n^m \, x \, P_{n-1}^m(x) - b_n^m \, P_{n-2}^m(x) \qquad (B.14)$$

where

$$a_n^m = \tfrac{1}{2} \left(\frac{4n^2-1}{n^2-m^2} \right)^{\frac{1}{2}} \quad \text{and} \quad b_n^m = \left(\frac{(2n+1)\,(n-m-1)\,(n+m-1)}{(2n-3)\,(n-m)\,(n+m)} \right)^{\frac{1}{2}}$$

Factoring $2 \, a_n^m$ from both terms on the right side of Eq (B.14) gives the following:

$$P_n^m(x) = \frac{x \, P_{n-1}^m(x) - \left(\dfrac{(n-m-1)\,(n+m-1)}{(2n-3)\,(2n-1)} \right)^{\frac{1}{2}} P_{n-2}^m(x)}{\left(\dfrac{n^2-m^2}{4n^2-1} \right)^{\frac{1}{2}}} \qquad (B.15)$$

Let $n \to n+1$ and $m \to \ell$.

$$P_{n+1}^\ell(x) = \frac{x \, P_n^\ell(x) - \left(\dfrac{(n-\ell)\,(n+\ell)}{(2n-1)\,(2n+1)} \right)^{\frac{1}{2}} P_{n-1}^\ell(x)}{\left(\dfrac{(n+1)^2 - m^2}{4\,(n+1)^2 - 1} \right)^{\frac{1}{2}}} \qquad (B.16)$$

Substituting Eq (B.13) into Eq (B.16), gives the following form of Eq (B.12):

$$P_{n+1}^\ell(x) = \frac{x \, P_n^\ell(x) - \varepsilon_n^\ell \, P_{n-1}^\ell(x)}{\varepsilon_{n+1}^\ell} \qquad (B.17)$$

125

Algorithm

The algorithm for computing wind vector components uses double precision calculations because the finite summation involves addition and subtraction of 992 terms per component.

1. Specify ϕ and λ .

2. Compute ϵ_n^{ℓ} .

3. Compute $P_{n+1}^{\ell}(\sin\phi)$ from the recursion relation, Eq (B.17).

4. Compute $EXP(i\ell\lambda) = \cos\ell\lambda + i \sin\ell\lambda$.

5. Compute (U,V) with Eq (B.10).

6. Compute $(u,v) = (U,V)/\cos\phi$.

Appendix C

Cloud Height Models

The height of a stabilized nuclear cloud in the atmosphere depends primarily on the weapon yield, atmospheric properties that affect cloud buoyancy and winds above the burst. Generally, cloud height increases with increasing weapon yield. Atmospheric nuclear weapons tests provided data for empirical fits to cloud height. The most recent and comprehensive correlations of visible cloud top and bottom height data are simple power laws (80).

$$H_{top} = c \ W^d \qquad (C.1)$$

$$H_{bot} = a \ W^b \qquad (C.2)$$

where

W is kilotons yield
H is meters above ground

a = 2228 b = 0.3463 W ≤ 4.07

a = 2661 b = 0.2198 W > 4.07

c = 3597 d = 0.2553 W ≤ 2.29

c = 3170 d = 0.4077 2.29 < W ≤ 19

c = 6474 d = 0.1650 W > 19

Yield-dependent heights are plotted in Figure C-1.

By comparison, the WSEG and AFIT codes use the following equation for height of the radioactive cloud center (19)(86).

$$HC = 44.0 + 6.1 \ \ln Y - 0.205 \ (\ln Y + 2.42) \ |\ln Y + 2.42| \qquad (C.3)$$
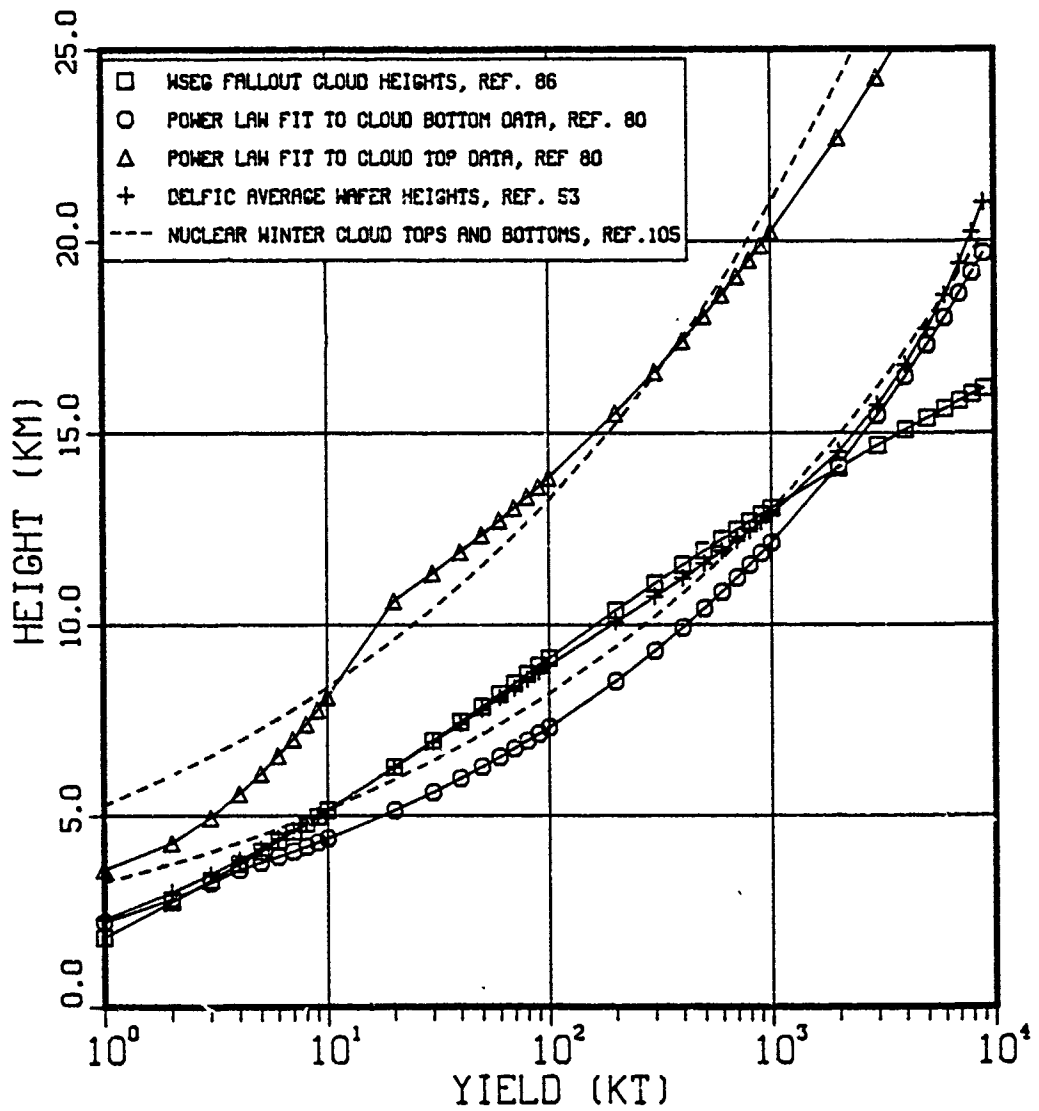
Figure C-1. Cloud Height vs Weapon Yield

where

Y is megatons yield
HC is kilofeet above ground

Figure C-1 shows that WSEG's equation puts the radioactive cloud near the bottom of the visible cloud. Early nuclear cloud data suggested that the fallout cloud was in the lower part of the visible cloud (92). For yields above 1 megaton, WSEG's predicted cloud height is notably lower than other models.

DELFIC raises thousands of wafers filled with different sized particles to various heights by stabilization time. Particle sizes are generally gravity-sorted in the initial cloud. Figure C-1 shows the average height of wafers containing the DELFIC default distribution's activity-median size (38 μm radius) in stabilized DELFIC clouds. The following equations were derived from DELFIC calculations of wafer heights in stabilized clouds (11)(53):

$$H_p = S \ D_p + B \qquad\qquad (C.4)$$

where

H_p is average height of DELFIC wafer centers (meters)

D_p is particle diameter (μm)

$S = EXP \ [\ 1.574 - 0.01197 \ln W + 0.03636 \ (\ln W)^2$
$\qquad\qquad - 0.0041 \ (\ln W)^3 + 1.965 \times 10^{-4} \ (\ln W)^4 \ ]$

$B = EXP \ [\ 7.889 + 0.34 \ln W + 0.001226 \ (\ln W)^2$
$\qquad\qquad - 0.005227 \ (\ln W)^3 + 4.17 \times 10^{-4} \ (\ln W)^4 \ ]$

The dashed lines in Figure C-1 are the cloud top and bottom heights used by Turco and others to predict the "nuclear winter" (105):

$$Z_{top} = 21 \ Y^{0.2} \tag{C.5}$$

$$Z_{bot} = 13 \ Y^{0.2} \tag{C.6}$$

where

Z is kilometers above ground.

Appendix D

Polynomials for Laurent Series Constants

Laurent series constants are used to compute r and dr/dt in the dose rate equation.

$$r = \sum_{i=1}^{6} C_i \, t^{i-6} + C_7 \, t^{-\frac{1}{2}} \qquad (D.1)$$

The constants, C_i, were derived by Colarco to enable smearing codes to rapidly determine particle size arriving on the ground from a specified height at a specified time (24). There are 1750 constants, 7 per altitude, 250 altitudes.

Each of the seven constants, C_i, was correlated with height (H_k) in kilometers (3). Seven polynomial fits were developed: one for each constant. Each polynomial for a C_i is 6th degree in height, containing seven constants $(D_{ij}$, j = 1,7).

$$C_i = D_{i1} + D_{i2} H_k + D_{i3} H_k^2 + D_{i4} H_k^3 + D_{i5} H_k^4 + D_{i6} H_k^5 + D_{i7} H_k^6 \qquad (D.2)$$

Table D-1 shows the polynomial constants, D_{ij} . Figures D-1 and D-2 show r and dr/dt computed two ways: using tabular C_i and using Eq (D.2). The figures show a family of curves for the same initial cloud heights published by Bridgman (19). Small magnitude coefficients (C_1-C_3) are not reproduced by Eq (D.2) as well as large magnitude coefficients (C_4-C_7) at altitudes $\lesssim$ 4 kilometers.

TABLE D-1

Polynomial Constants to Compute Laurent Series Constants

	j=1	2	3	4	5	6	7
i=1	.1569E-07	-.1818E-07	.5203E-08	-.5693E-09	.1994E-10	-.2735E-12	.1260E-14
2	-.4263E-07	.6693E-07	-.2723E-07	.4757E-08	-.1955E-09	.3031E-11	-.1612E-13
3	-.1415E-06	.1536E-06	-.4227E-07	-.7624E-08	.4437E-09	-.7726E-11	.4366E-13
4	-.4386E-07	.4344E-07	.5776E-06	-.2325E-07	.3289E-09	-.2013E-11	.7274E-14
5	.2489E-06	.3874E-05	-.9537E-08	-.8351E-08	.4146E-09	-.6988E-11	.3921E-13
6	-.1777E-05	-.1201E-08	.2176E-08	-.2020E-09	.1204E-10	-.2678E-12	.1945E-14
7	.1574E-04	.1394E-04	-.1112E-05	.5965E-07	-.1776E-08	.2647E-10	-.1548E-12
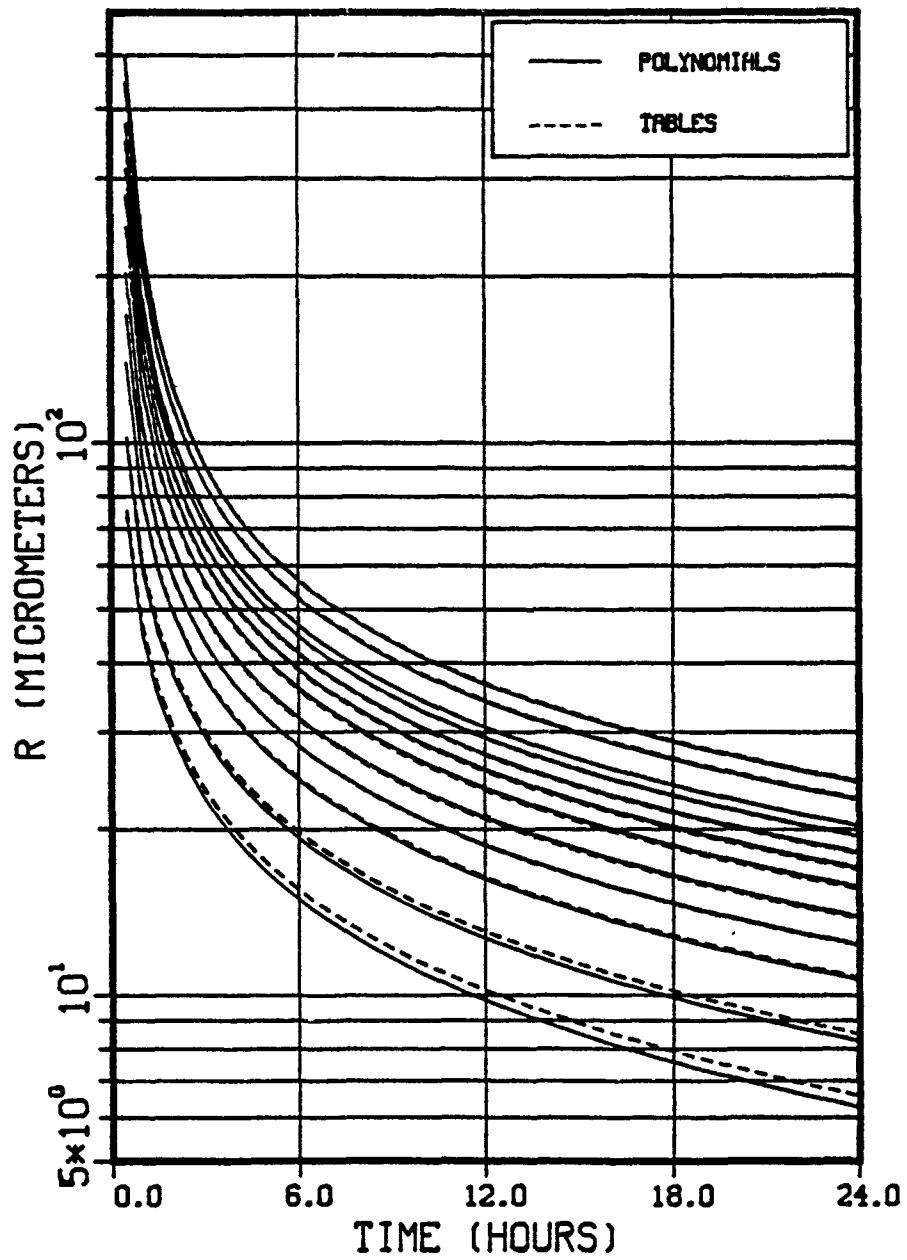
Figure D-1. Particle Size vs Arrival Time

133
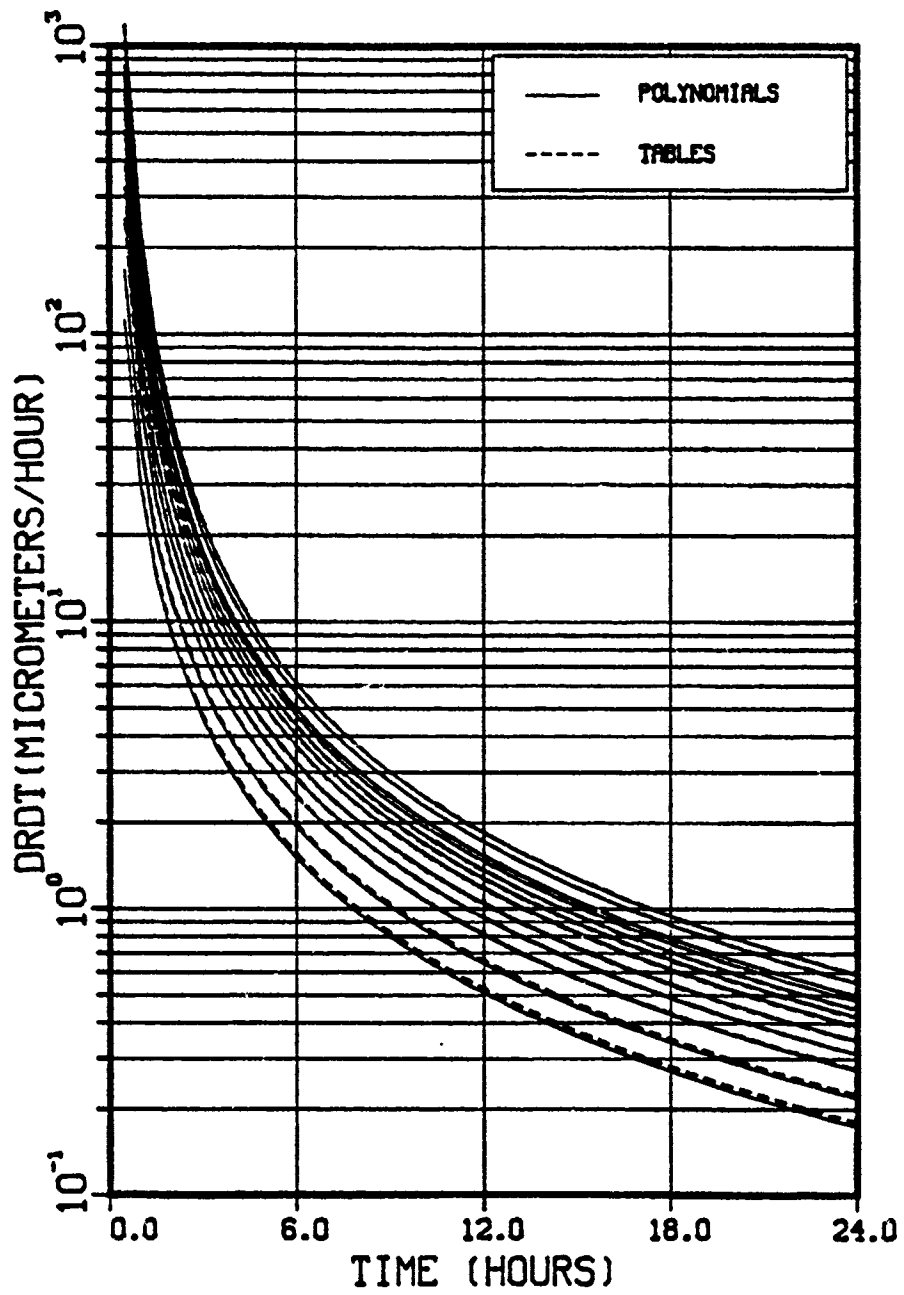
Figure D-2. |dr/dt| vs Arrival Time

Crosswind Integration of Spatial Distribution

The two-directional spatial distribution function defines how activity is distributed in the cloud horizontally.

$$F_{xy} = \int_0^\infty f(x,y,t) \, dt \qquad (E.1)$$

The integral was solved by Bridgman (19) using normal distributions in two directions and a constant unidirectional wind.

$$F_{xy} = \frac{1}{\sqrt{2\pi} \, \sigma_y \, V_x} \, EXP \left(-\tfrac{1}{2} \, \frac{y^2}{\sigma_y^2} \right) = \frac{F_y}{V_x} \qquad (E.2)$$

The term $(1/V_x)$ comes from the transformation of the integration variable from t to x, and F_y is a normalized Gaussian distribution in the crosswind (y) direction.

$$\int_{-\infty}^\infty F_{xy} \, dy = \frac{1}{V_x} \qquad (E.3)$$

If the wind is not constant and unidirectional, a more general result is derived. With variable winds, the spatial distribution function is expressed as follows:

$$F_{xy} = \frac{1}{\sqrt{2\pi} \, \sigma_v} \, EXP \left(-\tfrac{1}{2} \left(\frac{x \, V_y - y \, V_x}{\sigma_v} \right)^2 \right) \qquad (E.4)$$

135

Figure E-1 illustrates the positions of wind vector components, the ground point (x,y) and the crosswind direction.

Integrating F_{xy} in the crosswind direction gives the following:

$$\int_{C'}^{C} F_{xy}\ ds = \int_{C'}^{C} F_{xy}\ \left(\frac{ds}{dx}\right)\ dx \qquad (E.5)$$

If $\bar{r}$ is a vector in the crosswind direction,

$$\bar{r} = x\hat{\imath} - \frac{V_x}{V_y}\ x\hat{\jmath} \qquad (E.6)$$

and ds/dx is defined by (58):

$$\frac{ds}{dx} = (\ \dot{\bar{r}} \cdot \dot{\bar{r}}\ )^{\frac{1}{2}} = \left[\ 1 + \left(\frac{V_x}{V_y}\right)^2\ \right]^{\frac{1}{2}} \qquad (E.7)$$

The integral becomes:

$$\int_{-\infty}^{\infty} \frac{1}{\sqrt{2\pi}\ \sigma_v}\ \text{EXP}\left(\ -\frac{1}{2}\left(\frac{x\ V_y - y\ V_x}{\sigma_v}\right)^2\ \right)\left[\ 1 + \left(\frac{V_x}{V_y}\right)^2\ \right]^{\frac{1}{2}}\ dx \qquad (E.8)$$

$$= \frac{\left[\ 1 + \left(\frac{V_x}{V_y}\right)^2\ \right]^{\frac{1}{2}}}{\sqrt{2\pi}\ \sigma_v}\ \int_{-\infty}^{\infty} \text{EXP}\left(\ -\frac{1}{2}\left(\frac{x\ V_y - y\ V_x}{\sigma_v}\right)^2\ \right)\ dx \qquad (E.9)$$

On CC', $y = (-V_x/V_y)\ x$, so the integral in Eq (E.9) becomes:

$$\int_{-\infty}^{\infty} \text{EXP}\left(\ -\frac{1}{2}\ \frac{x^2\left(V_y + \frac{V_x^2}{V_y}\right)^2}{\sigma_v^2}\ \right)\ dx \qquad (E.10)$$

136
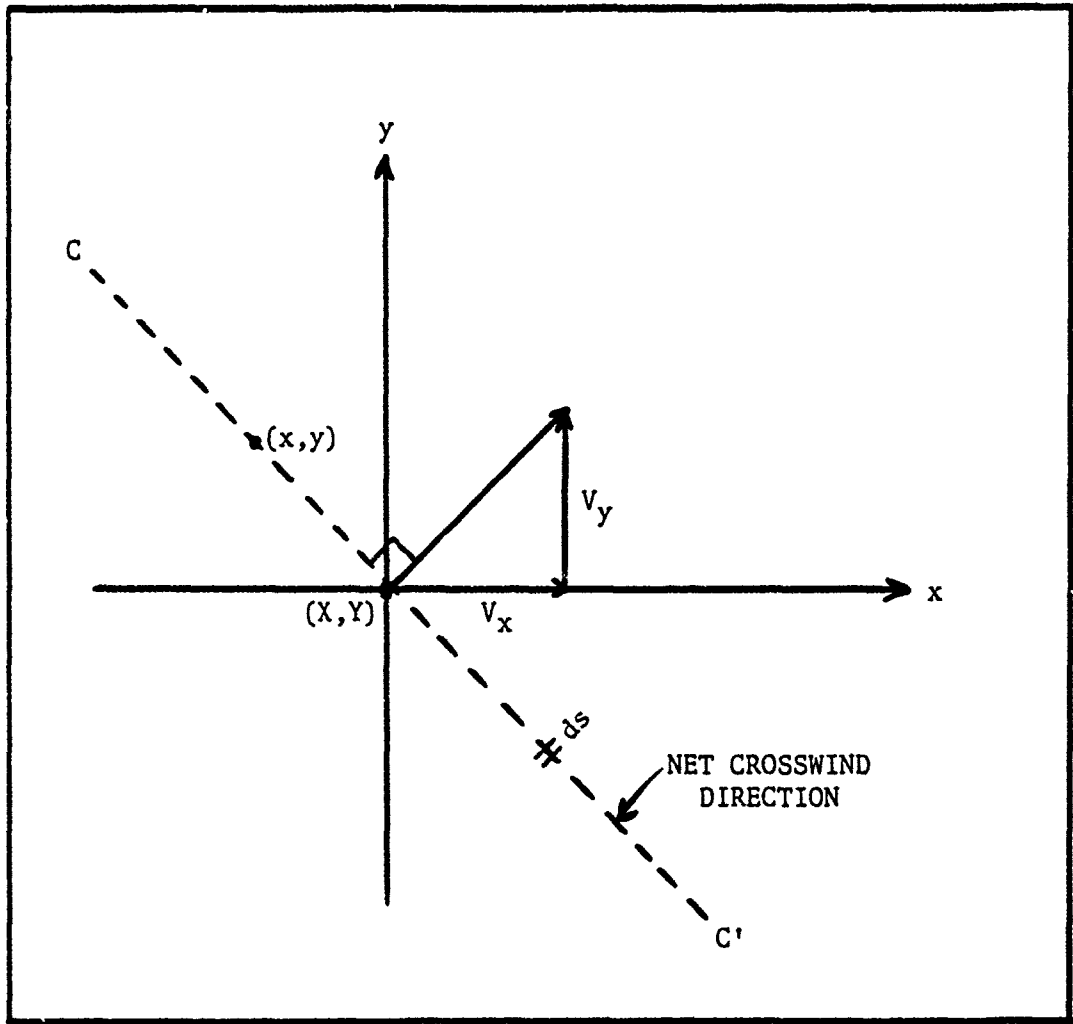
Figure E-1. Wind and Hotline Geometry

The above integral Eq (E.10) is solved aralytically (88):

$$= \frac{\sqrt{2\pi}\ \sigma_v}{V_y + \dfrac{V_x^2}{V_y}} \tag{E.11}$$

Therefore,

$$\int_{C'}^{C} F_{xy}\ ds = \frac{\left[\ 1 + \left(\dfrac{V_x}{V_y}\right)^2\ \right]^{\frac{1}{2}}}{V_y + \dfrac{V_x^2}{V_y}} = (\ V_x^2 + V_y^2\ )^{-\frac{1}{2}} \tag{E.12}$$

This solution reduces to $(1/V_x)$ or $(1/V_y)$ when a constant wind is uni-directional along the x or y axis. The constant wind result was derived by Bridgman and Bigelow (19).

Appendix F

Method to Compute Dose Rate at Arbitrary Coordinates

To compute dose rate at any point (x,y) downwind of the burst, it is necessary to identify the hotline point (X,Y) at the intersection of the net wind and crosswind lines. The point (x,y) lies on the crosswind line. See Figure IV-5. This appendix describes a way to find the hotline point associated with any ground point by marching along the hotline, computing the angle between the net wind and crosswind directions, until a right angle is found. The hotline point (X,Y) is simply bracketed between two discrete hotline points, and then determined explicitly, without resorting to a numerical convergence scheme.

Figure F-1 shows a hypothetical hotline, with net wind and crosswind lines drawn for three different hotline points:

(X,Y) is the hotline point on a net crosswind line to (x,y).
(X_i,Y_i) is the hotline point upwind of (X,Y).
(X_{i+1},Y_{i+1}) is the hotline point downwind of (X,Y).

The net wind vector from burst point $(0,0)$ to (X,Y) is OH: HF is the net crosswind line that is perpendicular to OH. The point (x,y) is on HF. The coordinates (X,Y) can be determined by finding the point (X,Y) that makes HF normal to OH. Following are line segments:

$$OA = (X_i^2 + Y_i^2)^{\frac{1}{2}} \tag{F.1}$$

$$AF = [(X_i - x)^2 + (Y_i - y)^2]^{\frac{1}{2}} \tag{F.2}$$

$$OF = (x^2 + y^2)^{\frac{1}{2}} \tag{F.3}$$
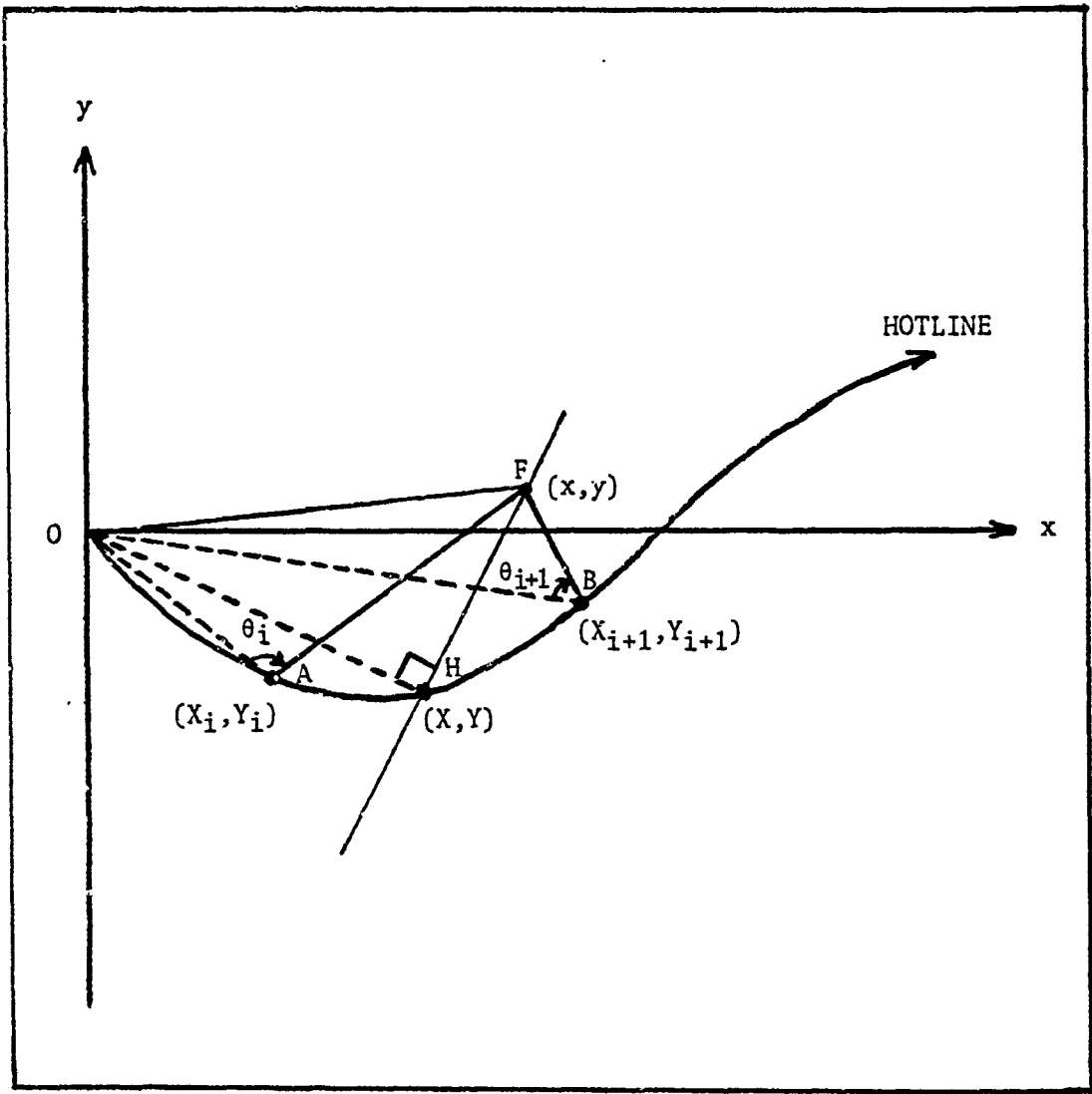
Figure F-1.   Hotline Geometry

The line OF is fixed. The angle θ_i changes to θ_{i+1} when (X_i, Y_i) changes to (X_{i+1}, Y_{i+1}). The angle θ_i is determined from the cosine law for triangles:

$$\cos\theta_i = \frac{OA^2 + AF^2 - OF^2}{2 \cdot OA \cdot AF} \tag{F.4}$$

To find (X,Y), it is necessary to march along the hotline, computing $\cos\theta$ at each hotline point. When $\cos\theta > 0$, $\theta = \theta_{i+1}$ and $\theta_{i+1} < \pi/2$, so (X,Y), the vertex of the right triangle OH-HF-OF, is between (X_i, Y_i) and (X_{i+1}, Y_{i+1}). Assuming a piecewise linear hotline, (X,Y) can be determined by finding ΔX, the distance from X_i to X; see Figure F-2.

$$X = X_i + \Delta X \quad \text{and} \quad Y = Y_i + \Delta Y \tag{F.5}$$

$$m = \frac{\Delta Y}{\Delta X} = \frac{(Y_{i+1} - Y_i)}{(X_{i+1} - X_i)} \tag{F.6}$$

$$\Delta Y = m \, \Delta X \tag{F.7}$$

Since OH is perpendicular to HF, the slopes of both lines are related.

$$\frac{y - Y}{x - X} = -\frac{X}{Y} \tag{F.8}$$

$$X^2 - Xx + Y^2 - Yy = 0 \tag{F.9}$$

Substituting Eq (F.5) for X and Y:

$$(X_i + \Delta X)^2 - (X_i + \Delta X) x + (Y_i + m \Delta X)^2 - (Y_i + m \Delta X) y = 0 \tag{F.10}$$

141
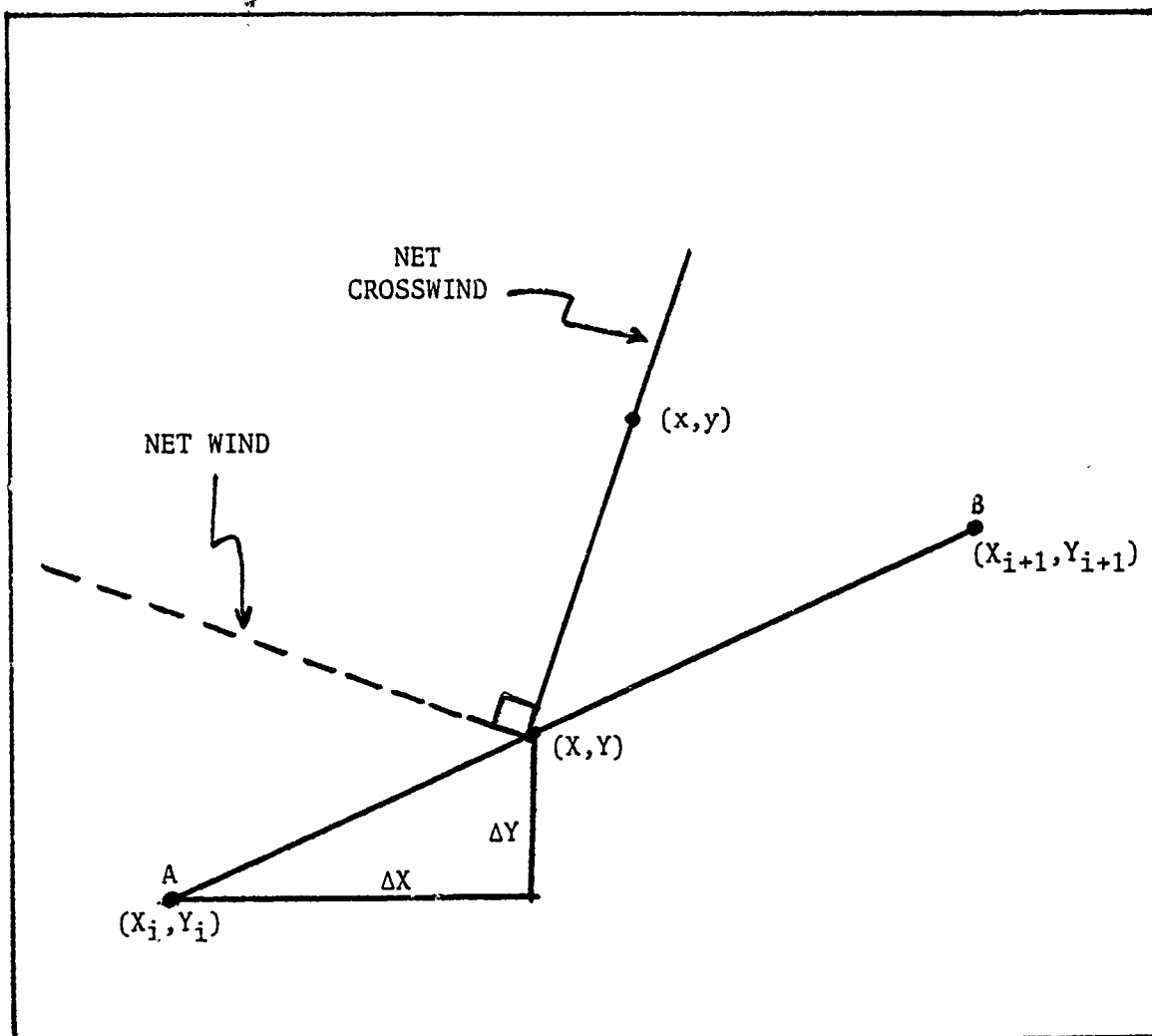
Figure F-2. Hotline Segment

$$A\ (\Delta X)^2 + B\ \Delta X + C = 0 \qquad (F.11)$$

where

$$A = 1 + m^2 \qquad (F.12)$$

$$B = 2\ X_i + 2\ m\ Y_i - x - m\ y \qquad (F.13)$$

$$C = X_i^2 + Y_i^2 - x\ X_i - y\ Y_i \qquad (F.14)$$

The quadratic Eq (F.11) can be solved explicitly for the two roots:

$$\Delta X_\pm = \frac{-B \pm (\ B^2 - 4AC\ )^{\frac{1}{2}}}{2A} \qquad (F.15)$$

Since the hotline segment is represented with line AB, the correct root is the value of ΔX that places $(X_i + \Delta X, Y_i + \Delta Y)$ on AB. In Figure F-3, $X_i + \Delta X_+$ is in segment AB. The other root also produces a right angle at (X, Y), but it does so by placing (X, Y) outside the AB segment.

The above method was verified by computing dose rates at arbitrary coordinates surrounding a curved hotline from a megaton cloud. Figure IV-9 is a three dimensional plot of downwind dose rates computed with this technique. Peak dose rates occur on the hotline and values decrease normally in crosswind directions.

y

NET
CROSSWIND

HOTLINE

(x,y)

x

NET WIND

B
(X_{i+1},Y_{i+1})

A
(X_i,Y_i)

$X=X_i+\Delta X_+$

$X=X_i+\Delta X_-$
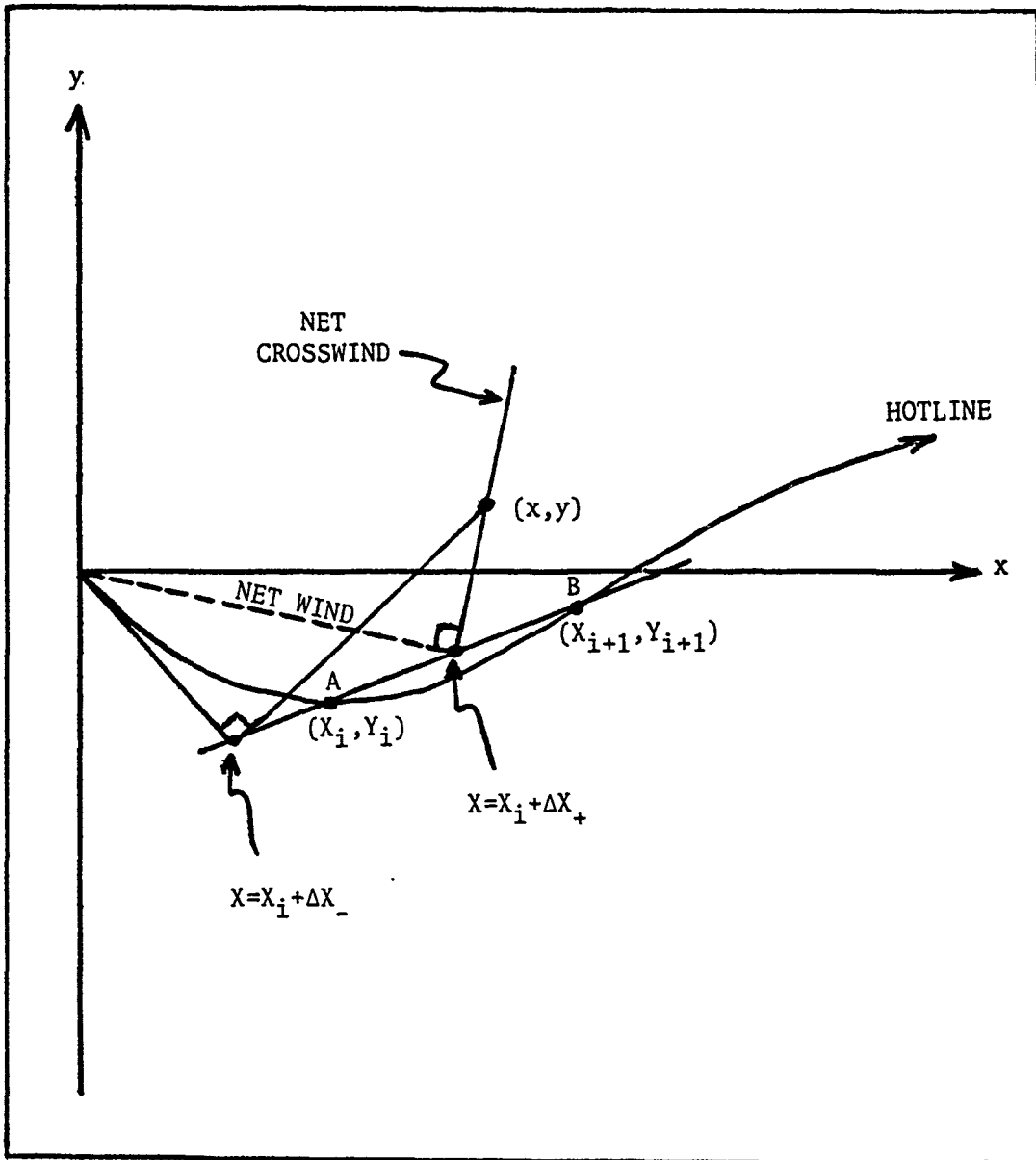
Figure F-3. Hotline with Root Locations

Appendix G

Function Minimization Method to Fit Particle Size Distribution Data

This appendix describes a technique to fit particle size distribution data points with a trimodal log-normal function. The technique requires minimization of the sum of the squares of differences between data points and functional values. The technique was used twice in this study: (1) to fit points in the measured size spectrum published by Carey and Sigurdsson (21), and (2) to fit size distribution data points that were back-calculated with the ashfall equation and actual fallout data.

The measured size distribution was digitized from the histogram shown in (21), yielding twenty values of grain size and corresponding weight fraction. At the top of each histogram bar, the average radius was computed, and used with the frequency for that range of particle sizes. Twenty data points were obtained.

The data points were fitted by minimizing the sum of twenty residuals: squared differences between data points and values of a trimodal log-normal function. See Eq (5.1). The follo ing function was minimized within a nine parameter hyperspace constrained by upper and lower bounds on the log-normal function parameters.

$$F = \sum_{j=1}^{20} [M(r_j) \cdot r_j - N(r_j) \cdot r_j]^2 \qquad (G.1)$$

where

$N(r_j)$ = measured particle size distribution function for twenty different particle radii
$M(r_j)$ = trimodal log-normal function
r_j = particle radius

The distribution functions $M(r_j)$ and $N(r_j)$, were weighted with r_j to facilitate selection of search limits on the hyperspace. This method produced an excellent fit to the measured data; the mean difference between $N(r_j) \cdot r_j$ and $M(r_j) \cdot r_j$ was 0.013 for the fit shown in Figure V-17. Log-normal function parameters are in Table V-3.

Isomass calculations with the ashfall equation and $M(r_j)$ generally agreed with ashfall data, but they did not replicate the Ritzville bulge. However, preliminary calculations, using the discontinuous histogram, showed that multiple modes in the mass size distribution produced multiple maxima in downwind ashfall. This observation suggested that a different particle size spectrum may have produced the bulge.

Using fallout data and the ashfall equation Eq (5.7), particle mass-size frequency was back-calculated at 13 points along the fallout centerline. The 13 points were then fitted with the trimodal log-normal function, Eq (5.1), using the same nine-parameter constrained minimization search technique used to fit the measured distribution data. The following function was minimized:

$$F = \sum_{j=1}^{13} [M'(r_j) \cdot r_j - N'(r_j) \cdot r_j]^2 \qquad \text{(G.2)}$$

where

$N'(r_j)$ = back-calculated particle size frequency at discrete points along the fallout centerline

$M'(r_j)$ = trimodal log-normal function

This method produced an excellent fit to the back-calculated data; the mean difference between $N'(r_j) \cdot r_j$ and $M'(r_j) \cdot r_j$ was 0.021. The fit is shown in Figure V-22. Log-normal function parameters are in Table V-4.

Bibliography

1. Abramowitz, Milton and Irene A. Stegun (editors). Handbook of Mathematical Functions with Formulas, Graphs and Mathematical Tables. Washington, D.C.: National Bureau of Standards, December 1972.

2. Aitchison, J. and J.A.C. Brown. The Lognormal Distribution. Cambridge: Cambridge University Press, U.K., 1957.

3. ASD Computer Center. Subprogram Library Guide: Polynomial Least Squares Curve Fit. Wright-Patterson AFB, OH: Aeronautical Systems Division, January 1978.

4. Baer, F. and F.N. Alyea. "Effects of Spectral Truncation on General Circulation and Long Range Prediction," Journal of the Atmospheric Sciences, 28: No.4: 457-480 (May 1971).

5. Ballish, Bradley A. Initialization, Theory and Application to the NMC Spectral Model. PhD Dissertation. University of Maryland, College Park, MD, 1980.

6. Bauer, Ernest. "Dispersion of Tracers in the Atmosphere and Ocean," Journal of Geophysical Research, 79 (6): 789-795 (20 February 1974).

7. Bauer, Ernest. The Growth and Disappearance of Tracer Clouds in the Atmosphere. IDA Note N-890, Institute for Defense Analysis, Alexandria, VA, June 1983.

8. Beck, H.L. and P.W. Krey. "Radiation Exposures in Utah from Nevada Nuclear Tests," Science, 220 (4592): 18-24 (1 April 1983).

9. Belousov, S.L. Tables of Normalized Associated Legendre Polynomials. Pergamon Press, New York, 1962.

10. Bevington, Philip K. Data Reduction and Error Analysis for the Physical Sciences. New York: McGraw Hill, 1969.

11. Bigelow, W.S. Jr. Major USAF. DELFIC Calculations for Hypothetical Nuclear Detonations at Washington, D.C. Unpublished Microfiche and Computer Printout, December 1979 and June 1981.

12. Bigelow, W.S. Jr. Major USAF. Far Field Fallout Prediction Techniques. PhD Dissertation. School of Engineering, Air Force Institute of Technology (AU), Wright-Patterson AFB, OH, December 1983.

13. Boquist, W. DIRECT COURSE Data Memo #2. Technology International Corporation, Bedford, MA, 24 January 1984.

14. Boquist, W. DIRECT COURSE Data Memo #3. Technology International Corporation, Bedford, MA, 16 February 1984.

15. Bourke, W. "A Multi-Level Spectral Model. I. Formulation and Hemispheric Integrations," _Monthly Weather Review_, _102_: 687-701 (October 1974).

16. Brazier, S. and others. "Bimodal Grain Size Distribution and Secondary Distribution in Air-Fall Ash Layers," _Nature_, _301_: 115-119 (13 January 1983).

17. Bridgman, Charles J. "Reply to Hillyer G. Norment," _Health Physics_, _46_ (1): 242-244 (January 1984).

18. Bridgman, Charles J. Unpublished Working Paper, Air Force Institute of Technology, Wright-Patterson AFB, OH, December 1981.

19. Bridgman, Charles J. and Winfield S. Bigelow. "A New Fallout Prediction Model," _Health Physics_, _43_ (2): 205-218 (August 1982).

20. Briggs, Steven R. and others. _Handbook on Atmospheric Diffusion_. DOE/TIC - 11223, U.S. Department of Energy, Washington, D.C., 1982.

21. Carey, Steven N. and Haraldur Sigurdsson. "Influence of Particle Aggregation on Deposition of Distal Tephra from the May 18, 1980 Eruption of Mount St. Helens Volcano," _Journal of Geophysical Research_, _87_ (B8): 7061-7072 (10 August 1982).

22. Cockayne, John E. DIRECT COURSE Rawinsonde Data from White Sands Missile Range. Science Applications Incorporated, McLean, VA, 28 November 1983.

23. Cockayne, John E. Ground Track Data for DIRECT COURSE Cloud Sampling Aircraft. Science Applications Incorporated, McLean, VA, 24 January 1984.

24. Colarco, R.F. _A Computer Fallout Model for Operational Type Studies_. MS Thesis, School of Engineering, Air Force Institute of Technology (AU), Wright-Patterson AFB, OH, 1980.

25. Cooley, Duane S. _Technical Procedure Bulletin No.105, A Description of the Flattery Global Analysis Method - No.1_. U.S. Deaprtment of Commerce, National Oceanic and Atmospheric Administration, National Weather Service, Silver Spring, MD, 10 January 1974.

26. Danielsen, Edwin F. "Trajectories of the Mount St. Helens Plume," _Science_, _211_ (4484): 819-821 (20 February 1981).

27. Davies, C.N. "Definitive Equations for the Fluid Resistance of Spheres," _Proceedings of the Physical Society of London_, _57_: 259-270 (July 1945).

28. Davis, Briant L. and others. "Quantitative Analysis of Mount St. Helens Ash by X-ray Diffraction and X-ray Fluorescence Spectrometry," _Journal of Applied Meteorology_, _20_ (8): 922-933 (August 1981).

29. Draxler, Roland R. and Albion D. Taylor. "Horizontal Dispersion Parameters for Long Range Transport Modeling," Journal of Applied Meteorology, 21 (3): 367-372 (March 1982).

30. Ehrlich, Paul R. and others. "Long-Term Biological Consequences of Nuclear War," Science, 222 (4630): 1293-1300 (23 December 1983).

31. Eisenbud, Merril. Environmental Radioactivity. Second Edition, New York: Academic Press, 1973.

32. Eliasen, E., B. Machenhauer and E. Rasmussen. On a Numerical Method for Integration of the Hydrodynamical Equation with a Spectral Representation of the Horizontal Fields. Copenhagen University, Institute for Theoretical Meteorology. Report Number 2. Copenhagen, Denmark, 1970.

33. Eliassen, Anton. "A Review of Long-Range Transport Modeling," Journal of Applied Meteorology, 19 (3): 231-240 (March 1980).

34. Ellsaesser, H.W. "Evaluation of Spectral vs Grid Methods of Hemispheric Numerical Weather Prediction," Journal of Applied Meteorology, 5: 246-262 (June 1966).

35. Ellsaesser, H.W. "Expansion of Hemispheric Meteorological Data in Anti Symmetric Surface Spherical Harmonic (Laplace) Series," Journal of Applied Meteorology, 5: 263-273 (June 1966).

36. Farlow, Neil H. and others. "Size Distributions and Mineralogy of Ash Particles in the Stratosphere from Eruptions of Mount St. Helens," Science, 211 (4484): 832-834 (20 February 1981).

37. Flattery, Thomas W. Major USAF. Spectral Models for Global Analysis and Forecasting. Paper Included in "Automated Weather Support, Proceedings of the Sixth AWS Technical Exchange Conference," AWS Technical Report 242, U.S. Naval Academy, Annapolis, MD, April 1971.

38. Folsom, Michael M. and Robert R. Quinn. Open File Report 80-12. Department of Natural Resources, Division of Geology and Earth Resources, Olympia, WA, July 1980.

39. Fruchter, Jonathan S. and others. "Mount St. Helens Ash from the 18 May 1980 Eruption: Chemical, Physical, Mineralogical, and Biological Properties," Science, 209 (4461): 1116-1125 (5 September 1980).

40. Fuchs, N.A. The Mechanics of Aerosols. New York: Pergamon Press, 1964.

41. Glasstone, Samuel and Philip J. Dolan. The Effects of Nuclear Weapons. Third Edition. Washington, D.C.: U.S. Government Printing Office, 1977.

42. Haaland, Carsten M. "Forecasting Radiation Exposure from Fallout Caused by Multiple, Non-Simultaneous, Upwind Ground Bursts," Health Physics, 46 (2): 347-359 (February 1984).

43. Haltiner G.J. and F.L. Martin. Dynamical and Physical Meteorology. New York: McGraw-Hill, 1957.

44. Harris, David M. and others. "Radar Observations of Ash Eruptions," Paper published in The 1980 Eruptions of Mount St. Helens, Washington, Lipman and Mullineaux, Editors. U.S. Department of the Interior, Washington, D.C., 1982.

45. Harris, David M. and William I. Rose, Jr. "Estimating Particle Sizes, Concentrations, and Total Mass of Ash in Volcanic Clouds Using Weather Radar," Journal of Geophysical Research, 88 (C15): 10969-10983 (20 December 1983).

46. Hawthorne, Howard A. (editor). Compilation of Local Fallout Data from Test Detonations 1945-1962 Extracted from DASA 1251. DNA 1251-1 and 2 Ex. Defense Nuclear Agency, Washington, D.C., 1 May 1979.

47. Hawthorne, Howard A. Fallout Hazard Prediction Inconsistencies. DASIAC SR174. Santa Barbara, CA: General Electric Company, 1 October 1979.

48. Heald, R.C. and L. Mahrt. "The Dependence of Boundary-Layer Shear on Diurnal Variation of Stability," Journal of Applied Meteorology, 20 (8): 859-868 (August 1981).

49. Hedman, Fritz A. and Ralph C. Simmons. Wind-Weighting Factors for Fallout Calculations. NMCSSC TR 10-66. Washington, D.C.: Defense Communications Agency, December 1966.

50. Heffter, Jerome L. and others. A Regional-Continental Scale Transport, Diffusion, and Deposition Model. NOAA Technical Memorandum ERL ARL-50, Air Resources Laboratories, Silver Spring, MD, June 1975.

51. Hobbs, Peter V. and others. "Particles and Gases in the Emissions from the 1980-1981 Volcanic Eruptions of Mt. St. Helens," Journal of Geophysical Research, 87 (C12): 11062-11086 (20 December 1982).

52. Hooper, P.R. and others. "Composition of the Mount St. Helens Ashfall in the Moscow-Pullman Area on 18 May 1980," Science, 209 (4461): 1125-1126 (5 September 1980).

53. Hopkins, Arthur T. A Two Step Method to Treat Variable Winds in Fallout Smearing Codes. MS Thesis, Air Force Institute of Technology, Wright-Patterson AFB, OH, March 1982.

54. Hough, S.S. "On the Application of Harmonic Analysis to the Dynamical Theory of the Tides. Part II. On the General Integration of Laplace's Dynamical Equations," Royal Society of London Philosophical Transactions A, 191: 139-185 (1898).

55. International Mathematical and Statistical Libraries Inc. Global Minimum (with Constraints) of a Function of N Variables. IMSL Library Reference Manual. IMSL, Houston, TX, 1982.

56. Katz, Arthur M. Life After Nuclear War, the Economic and Social Impacts of Nuclear Attacks on the United States. Cambridge, MA: Ballinger Publishing Company, 1982.

57. Knox, Joseph B. and Nicholas M. Short. "A Diagnostic Model Using Ashfall Data to Determine Eruption Characteristic and Atmospheric Conditions During a Major Volcanic Event," Bulletin Volcanologique, 27: 5-24 (1964).

58. Kreysig, Erwin. Advanced Engineering Mathematics. New York: Wiley, 1979.

59. Kuntz, Mel A. and others. "Petrography and Particle-Size Distribution of Pyroclastic-Flow, Ash-Cloud and Surge Deposits," Paper published in The 1980 Eruptions of Mount St. Helens, Washington, Lipman and Mullineaux, editors. U.S. Department of the Interior, Washington, D.C., 1982.

60. Lewis, Kevin N. "The Prompt and Delayed Effects of Nuclear War," Scientific American, 241: 25-47 (July 1979).

61. Lipman, Peter W. and Donal R. Mullineaux (editors). The 1980 Eruptions of Mount St. Helens, Washington. Geological Survey Professional Paper 1250. U.S. Department of the Interior, Washington, D.C., 1981.

62. Longuet-Higgins, M.S. "The Eigenfunctions of Laplace's Tidal Equations over a Sphere," Philosophical Transactions of the Royal Society of London. 262: 511-607 (February 1968).

63. Machta, Lester. "Status of Global Radioactive Fallout Predictions," Paper Published in Radioactive Fallout from Nuclear Weapons Tests, A.W. Klement, Jr. (editor). CONF-765. Proceedings of the Second Conference, U.S. Atomic Energy Commission, Washington, D.C., November 1965.

64. Machta, Lester and others. "Airborne Measurements of Atomic Debris," Journal of Meteorology, 14: 165-175 (April 1957).

65. Mason, Ralph B. Fallout Wind Illustrations for the "Most Probable" Wind Data Sets. Technical Memorandum TM275-82. Command and Control Technical Center, Washington, D.C., 1 July 1982.

66. Mason, Ralph B. Population at Risk from Fallout. Technical Report TR192-81. Command and Control Technical Center, Washington, D.C., 1 June 1981.

67. McDonald, James E. "An Aid to Computation of Terminal Fall Velocities of Spheres," Journal of Meteorology, 17: 463-465 (August 1960).

68. McDonald, James E. "Rates of Descent of Fallout Particles from Thermonuclear Explosions," Journal of Meteorology, 17: 380-382 (June 1960).

69. McGahan, J.T. Fallout in the Context of Passive Defense. Briefing Slides. Science Applications Incorporated, McLean, VA, 19 January 1983.

70. McPherson, Ronald D. "Lectures on Operational Analysis and Assimilation of Meteorological Observations VI. An Assessment of Analysis Performance," National Meteorological Center, Camp Springs, MD, May 1980.

71. Meriless, P.E. "The Equations of Motion in Spectral Form," Journal of the Atmospheric Sciences, 25: 736-743 (September 1968).

72. Messiah, A. Quantum Mechanics. New York: North Holland Publishing Company, 1961.

73. Miller, C. Dan and others. "Hazards Assessments at Mount St. Helens," Paper Published in The 1980 Eruptions of Mount St. Helens, Washington, Lipman and Mullineaux, editors. U.S. Department of the Interior, Washington, D.C., 1982.

74. Milne, William Edmund. Numerical Calculus Approximations, Interpolation, Finite Differences, Numerical Integration and Curve Fitting. Princeton, NJ: Princeton University Press, 1949.

75. National Oceanic and Atmospheric Administration. U.S. Standard Atmosphere, 1976. National Aeronautics and Space Administration and U.S. Air Force. Washington, D.C., 1976.

76. National Research Council. Long-Term Worldwide Effects of Multiple Nuclear-Weapons Detonations. National Academy of Sciences, Washington, D.C., 1975.

77. Newell, Reginald E. and Adarsh Deepak (editors). Mount St. Helens Eruptions of 1980: Atmospheric Effects and Potential Climatic Impact. NASA SP-458. Washington, D.C.: National Aeronautics and Atmospheric Administration, 1982.

78. Norment, Hillyer G. "Comments on the Paper 'A New Fallout Prediction Model'," Health Physics, 46 (1): 239-242 (January 1984).

79. Norment, Hillyer G. DELFIC: Department of Defense Fallout Prediction System, Volume I-Fundamentals. DNA 5159F-1. Defense Nuclear Agency, Washington, D.C., 1979.

80. Norment, Hillyer G. DNAF-1 An Analytical Fallout Prediction Model and Code. DNA 6168F. Defense Nuclear Agency, Washington, D.C., 1981.

81. Norment, Hillyer G. Evaluation of Three Fallout Models: DELFIC, SEER and WSEG-10. Draft of Final Report for Defense Nuclear Agency. Atmospheric Science Associates, Bedford, MA, 28 April 1978.

82. Office of Technology Assessment. The Effects of Nuclear War. Congress of the United States, Washington, D.C., 1979.

83. Orszag, S.A. "Transform Method for the Calculation of Vector-Coupled Sums: Application to the Spectral Form of the Vorticity Equation," Journal of the Atmospheric Sciences, 27: 890-895 (September 1970).

84. Polan, M. An Analysis of the Fallout Prediction Models Presented at the USNRDL-DASA Fallout Symposium of September 1962. Vol.II: Analyses, Comparison and Evaluation of Model Predictions. NRDL TRC-68-59. San Fransicso, CA: Naval Radiological Defense Laboratory, 28 August 1968.

85. Pugh, George E. Revision of Fallout Parameters for Low Yield Detonations. Supplement to WSEG Research Memorandum No.10, Weapon Systems Evaluation Group, Washington, D.C., 23 October 1961.

86. Pugh, George E. and R.J. Galliano. An Analytic Model of Close-In Deposition of Fallout for Use in Operational Type Studies. Weapon Systems Evaluation Group Memorandum RM10. Washington, D.C., 1959.

87. Puri, Kamal and William Bourke. "Implications of Horizontal Resolution in Spectral Model Integrations," Monthly Weather Review, 102 (5): 333-347 (May 1974).

88. Reif, F. Fundamentals of Statistical and Thermal Physics. New York: McGraw-Hill, Inc., 1965.

89. Robert, A.J. The Behavior of Planetary Waves in an Atmosphere Model Based on Spherical Harmonics. McGill University Publication in Meteorology, No.77: 59-62 (1965).

90. Sarna-Wojcicki, Andrei M. and others. "Areal Distribution, Thickness, Mass, Volume, and Grain Size of Air-Fall Ash from the Six Major Eruptions of 1980," Paper Published in The 1980 Eruptions of Mount St. Helens, Washington, Lipman and Mullineaux, editors. U.S. Department of the Interior, Washington, D.C., 1982.

91. Sarna-Wojcicki, Andrei M. and others. "Composition of Air-Fall Ash Erupted on May 18, May 25, June 12, July 22, and August 7," Paper published in The 1980 Eruptions of Mount St. Helens, Washington, Lipman and Mullineaux, editors. U.S. Department of the Interior, Washington, D.C., 1982.

92. Schuert, E.A. A Fallout Forecasting Technique with Results Obtained at the Eniwetok Proving Ground. USNRDL TR-139, United States Naval Research Defense Laboratories, San Francisco, CA, 3 April 1957.

93. Sela, Joseph G. "Spectral Modeling at the National Meteorological Center," Monthly Weather Review, 108 (9): 1279-1292 (September 1980).

94. Sela, Joseph G. Telephone Conversation. National Meteorological Center, Camp Springs, MD, 10 May 1983.

95. Sela, Joseph G. The NMC Spectral Model. NOAA Technical Report NWS 30, U.S. Department of Commerce, National Oceanic and Atmospheric Administration, National Weather Service, Silver Spring, MD, May 1982.

96. Slade, David H. (editor). Meteorology and Atomic Energy. TID-24190, U.S. Atomic Energy Commission, Washington, D.C., July 1968.

97. Slaughter, M. and M. Hamil. "Model for Deposition of Volcanic Ash and Resulting Bentonite," Geological Society of America Bulletin, 81: 961-968 (March 1970).

98. Slinn, W.G.N. Meteorological Aspects of the Reactor Safety Study Requiring Further Study. Published in "Proceedings of the Symposium on Intermediate Range Atmospheric Transport Processes and Technology Assessment," CONF-801064, U.S. Department of Energy, Gatlinberg, TN, October 1981.

99. Smith, William K. A Plotting Program for Producing Ashfall Prediction Maps from Output of the NOAA Forecast Trajectory Program: Application to and Examples from the 1980 Mount St. Helens Eruptions. Open File Report 80-2005, United States Department of the Interior, Geological Survey, Washington, D.C., 1980.

100. Sorem, Ronald K. "Volcanic Ash Clusters: Tephra Rafts and Scavengers," Journal of Volcanology and Geothermal Research, 13 (1-2): 63-71 (July 1982).

101. Staff of the Air Resources Laboratories. "Estimates of the Path of Volcanic Ash in the Troposphere and Stratosphere from the Mt. St. Helens Eruption of May 18, 1980," Environmental Research Laboratories, National Oceanic and Atmospheric Administration, Silver Spring, MD, 29 May 1980.

102. Stewart, Robert E. "Estimating Lateral Growth Rate of a Particulate Plume," *Journal of Applied Meteorology*, 7: 947-950 (October 1968).

103. Tarbell, Terry C. Major USAF, and others. *High Resolution Analysis System (HIRAS) Functional Description (Revised)*. Air Force Global Weather Central, Offutt AFB, NB, February 1982.

104. Telegadas, Kosta. "Estimation of Maximum Credible Atmospheric Radioactivity Concentrations and Dose Rates from Nuclear Tests," *Atmospheric Environment*, 13: 327-334 (1979).

105. Turco, R.P. and others. "Nuclear Winter: Global Consequences of Multiple Nuclear Explosions," *Science*, 222 (4630): 1283-1292 (23 December 1983).

106. United States Department of the Interior, Geological Survey. *The National Atlas of the United States of America*. Washington, D.C., 1970.

107. Valley, S.L. (editor). *Handbook of Geophysics and Space Environments*. Bedford, MA: Air Force Cambridge Research Laboratories and Office of Aero-Space Research, 1965.

108. Vlcek, Charles L. *Monthly RMS Vector Error for 100 MB Spectral Analysis (North America)*. National Meteorological Center, Camp Springs, MD (14 May 1984).

109. Vlcek, Charles L. *Monthly RMS Vector Error for 250 MB Spectral Analysis (North America)*. National Meteorological Center, Camp Springs, MD (14 May 1984).

110. Vlcek, Charles L. *Monthly RMS Vector Error for 500 MB Spectral Analysis (North America)*. National Meteorological Center, Camp Springs, MD (20 March 1984).

111. Vlcek, Charles L. *Monthly RMS Vector Error for 850 MB Spectral Analysis (North America)*. National Meteorological Center, Camp Springs, MD (20 March 1984).

112. Warburton, John D., Major USAF. Magnetic Tape and Computer Listing of National Weather Service Routines for Spectral Coefficients. National Meteorological Center, Camp Springs, MD, 26 April 1983.

113. Warburton, John D., Major USAF. Magnetic Tape with Spectral Coefficients for 18, 19, 20 May 1980. Tape Number X00910. National Meteorological Center, Camp Springs, MD, 19 September 1983.

114. Warburton, John D., Major USAF. Magnetic Tape with Spectral Coefficients for 26, 27 October 1983. Tape Number X00464. National Meteorological Center, Camp Springs, MD, 28 November 1983.

115. Weinberger, H.F. A First Course in Partial Differential Equations. New York: Blaisdell Publishing Company, 1965.

116. Westphal, Louis A. 9018 Global Analysis Tape for 15-31 May 80. NCDC TD-9609. USAF Environmental Technical Applications Center, Asheville, NC, 23 June 1983.

117. Wilkins, Eugene M. "Effective Coefficients of Diffusivity for Atomic Bomb Clouds at One Thousand to Two Thousand Miles," Transactions of the American Geophysical Union, 39 (1): 58-59 (February 1958).

118. Wilson, L. and T.C. Huang. "The Influence of Shape on the Atmospheric Settling Velocity of Volcanic Ash Particles," Earth and Planetary Science Letters, 44: 311-324 (August 1979).

119. Young, David M. and Robert Todd Gregory. A Survey of Numerical Mathematics. Reading, MA: Addison-Wesley Publishing Company, 1972.

VITA

Arthur Thomas Hopkins was born 8 January 1949 in Lewiston, Maine. He graduated from Lewiston High School and attended the Catholic University of America in Washington, D.C., where he earned Bachelor and Master of Science in Engineering degrees in Aerospace and Atmospheric Sciences. He entered the U.S. Air Force in July 1973 as a reentry physics project manager at the Space and Missile Systems Organization, Los Angeles, California. In 1977, he was assigned to the Defense Nuclear Agency, Washington, D.C., as a nuclear research officer. He entered the Air Force Institute of Technology Nuclear Engineering program in 1980, and earned the Master of Science in Nuclear Engineering degree in 1982. He is a member of Tau Beta Pi, the American Nuclear Society, the Health Physics Society, and the American Meteorological Society.

Permanent Address: 12 Whipple Street
                     Lewiston, Maine   04240

REPORT DOCUMENTATION PAGE

1a REPORT SECURITY CLASSIFICATION	1b. RESTRICTIVE MARKINGS
UNCLASSIFIED	

2a. SECURITY CLASSIFICATION AUTHORITY	3. DISTRIBUTION/AVAILABILITY OF REPORT
2b. DECLASSIFICATION/DOWNGRADING SCHEDULE	Approved for public release; distribution unlimited

4. PERFORMING ORGANIZATION REPORT NUMBER(S)	5. MONITORING ORGANIZATION REPORT NUMBER(S)
AFIT/DS/ENP/84-2	

6a. NAME OF PERFORMING ORGANIZATION	6b. OFFICE SYMBOL (If applicable)	7a. NAME OF MONITORING ORGANIZATION
School of Engineering	AFIT/ENP	

6c. ADDRESS (City, State and ZIP Code)	7b. ADDRESS (City, State and ZIP Code)
Air Force Institute of Technology Wright-Patterson AFB, Ohio 45433	

8a. NAME OF FUNDING/SPONSORING ORGANIZATION	8b. OFFICE SYMBOL (If applicable)	9. PROCUREMENT INSTRUMENT IDENTIFICATION NUMBER
Defense Nuclear Agency	STBE	

8c. ADDRESS (City, State and ZIP Code)	10. SOURCE OF FUNDING NOS.			
	PROGRAM ELEMENT NO.	PROJECT NO.	TASK NO.	WORK UNIT NO.
Washington, D.C. 20305				

11. TITLE (Include Security Classification)
See Box 19

12. PERSONAL AUTHOR(S)
Hopkins, Arthur Thomas   Major USAF

13a. TYPE OF REPORT	13b. TIME COVERED		14. DATE OF REPORT (Yr., Mo., Day)	15. PAGE COUNT
PhD Dissertation	FROM _____	TO _____	1984 September	170

16. SUPPLEMENTARY NOTATION
from p. XI —> Originator-supplied key words included:

17. COSATI CODES			18. SUBJECT TERMS (Continue on reverse if necessary and identify by block number)
FIELD	GROUP	SUB. GR.	Fallout, Particle Trajectories, *Spectral Coefficients*
18	08		Atmospheric Motion, Volcanoes, *Distribution Functions, Theses*
08	07		

19. ABSTRACT (Continue on reverse if necessary and identify by block number)

Title: DEVELOPMENT AND VALIDATION OF A NEW FALLOUT
TRANSPORT METHOD USING VARIABLE SPECTRAL WINDS

Advisory Committee Chairman: Charles J. Bridgman

Approved for public release: IAW AFR 190-17.

LYNN E. WOLAVER   25 Feb 85
Dean for Research and Professional Development
Air Force Institute of Technology (ATC)
Wright-Patterson AFB OH 45433

20. DISTRIBUTION/AVAILABILITY OF ABSTRACT	21. ABSTRACT SECURITY CLASSIFICATION
UNCLASSIFIED/UNLIMITED ☒ SAME AS RPT. ☐ DTIC USERS ☐	UNCLASSIFIED

22a. NAME OF RESPONSIBLE INDIVIDUAL	22b. TELEPHONE NUMBER (Include Area Code)	22c. OFFICE SYMBOL
Charles J. Bridgman, Professor	(513) 255-2012	AFIT/ENP

DD FORM 1473, 83 APR   EDITION OF 1 JAN 73 IS OBSOLETE.

A new method has been developed to incorporate variable winds into fallout transport calculations. The method uses spectral coefficients derived by the National Meteorological Center. Wind vector components are computed with the coefficients along the trajectories of falling particles. Spectral winds are used in a two-step method to compute dose rate on the ground, downwind of a nuclear cloud. First, the hotline is located by computing trajectories of particles from an initial, stabilized cloud, through spectral winds, to the ground. The connection of particle landing points is the hotline. Second, dose rate on and around the hotline is computed by analytically smearing the falling cloud's activity along the ground. The feasibility of using spectral winds for fallout particle transport was validated by computing Mount St. Helens ashfall locations and comparing calculations to fallout data. In addition, an ashfall equation was derived for computing volcanic ash mass/area on the ground. Ashfall data and the ashfall equation were used to back-calculate an aggregated particle size distribution for the Mount St. Helens eruption cloud. Further validation was performed by comparing computed and actual trajectories of a high explosive dust cloud (DIRECT COURSE). Using an error propagation formula, it was determined that uncertainties in spectral wind components produce less than four percent of the total dose rate variance. In summary, this research demonstrated the feasibility of using spectral coefficients for fallout transport calculations, developed a two-step smearing model to treat variable winds, and showed that uncertainties in spectral winds do not contribute significantly to the error in computed dose rate.